PROCEEDINGS

of

The first International Conference on

Recent and Emerging Trends in Computer and Computational Sciences

CONTENTS

Abstract. Graphs arising from real life applications are typically large, depending on the task at hand a simple yet effective strategy would be to partition the graph and process the resultant sub graphs individually. More generally suppose a problem with a given objective is decomposed into smaller instances, how does the combined solution from the sub instances compare with the optimal solution obtained from the original instance. In this work we investigate the application of such a strategy with respect to two NP-hard problems that arise in many applications, namely the Minimum Dominating Set and Maximum Coverage. Accordingly we define performance ratios and derive relationships between these and quantities that can be computed from a given graph and sub graphs obtained from partitioning it. We show that a "minimum vertex support cut" maximises a lower bound on a defined performance ratio, for the minimum dominating set and also a special case of the maximum coverage. We empirically assess how some of the commonly used graph cuts such as the normalised cut fare with respect to the performance ratios defined above on both synthetic and real graphs.

Keywords : Graph cut, Minimum Dominating Set, Maximum Coverage, Word of mouth marketing,Social Network Analysis, Greedy algorithm

1 Introduction

The information age has resulted in an explosion of data, thus the size of problems in present day applications presents many challenges. Graphs are a very useful representation in many applications, typically graphs arising from real life applications are large. One possible way do deal with a large problem is to break it into smaller problems which can then be processed individually. A natural question is the following. Consider an instance of a problem where the aim is to minimize/maximize a given objective. Suppose the problem is decomposed into smaller sub instances and the optimal solutions from each of these sub instances are combined, how much worse is the combined solution from the sub instances as compared to the optimal solution obtained from the original instance.

In this paper we consider the above question with respect to two graph related NP-hard problems. The Minimum Dominating Set (MDS) (and the set cover problem of which the MDS may be regarded as a special case) and Maximum Coverage problems arise in many applications, such as choosing an initial set of target nodes in a word of mouth marketing scenario for instance. These may be formally stated as follows.

Minimum dominating set (MDS) : *Given a graph* $G \equiv (V, E)$*, find a set* $V^{'} \subseteq V$ *of smallest cardinality such that for all* $u \in V - V^{'}$ *there is a* $v \in V^{'}$ *for which* $(u, v) \in E$*.*

The Minimum dominating set can be treated as an instance of the well known **Set Cover Problem** [2].

Maximum Coverage (MC) : *Given a universe* U *of* n *elements and a family* F *of subsets of* U*, and an integer* $k \leq \mid F \mid$*, find the* k*-element subset* $C \in F$ *(i.e.*

$| C |= k$) *that maximises* $\cup_{S \in C} S$. *i.e. choose a subset of the family* F *such that the number of elements covered is maximised.*
Although both the set cover problem and Maximum Coverage problem are NP-hard, a polynomial time greedy approximation algorithm may be employed; in each step of the greedy algorithm, the set S covering the largest number of remaining uncovered elements is picked. The only difference in the application in case of Maximum Coverage, is that the algorithm terminates after k steps.

While there exists a significant amount of literature related to the dominating set and maximum coverage problems, the main contribution of this paper is examining the above problems in a problem decomposition context. Given that many real world networks consist of a large number of nodes, it may often be infeasible to work on the entire graph. A practical strategy in such a situation would be to partition the graph into smaller subgraphs which could be processed individually. In this work we focus specifically on the following question *given a graph and subgraphs obtained by partitioning it, how close is the combined solution from the individual subgraphs to the optimal solution that could be obtained from the original graph (with respect to a particular objective).*

The outline of the rest of the paper is as follows. We introduce some notation in section 1.1. In section 2 we define performance ratios for the above problems in terms of the ratio of the combined optimal solution from the subgraphs to that obtained from the full graph, we also define corresponding *empirical* performance ratios which can be computed directly from a given graph and subgraphs obtained by partitioning it. In section 2.1 we state a few relationships between these corresponding quantities focusing mostly on the case of two partitions. We report empirical results on real and synthetic graphs, partitioning the graphs using the popular min and normalised cuts respectively.

1.1 Notation

We introduce some notation which will be used in the rest of the paper. We consider a graph $G \equiv (V, E)$ with an incidence matrix A for the rest of the paper. Almost all the discussion in this paper does not require a distinction between weighted and unweighted graphs. Thus $G \equiv (V, E)$ could be considered as a binary *coverage graph* (V is the set of vertices and E the set of edges and node i is said to "cover" node j if $G(i, j) = 1$). In practice, G could be obtained from the original network, by applying criteria most suitable to the particular application. For instance the coverage matrix could be the binary matrix obtained by applying a threshold on the edge weights of the original network. Another possibility is that a node i could be deemed to cover node j if there is a path of length h or less from node i to node j.

If the graph is used for modeling dynamics of interaction between individual entities such as propagation of viruses (whether biological or computer viruses) through a social network, word of mouth marketing etc. and the edge weights represent probabilities of activation, then retaining only edges with weight above a threshold (say p_{thresh}) amounts to enforcing that any currently inactive node has a probability of activation of at least p_{thresh} if any of its neighbours are

active. In this case $G(i,j) = 1$ implies that i activates j with a probability $\geq p_{thresh}$.

- Define $cover(G,S) = \cup_{x \in S}(N(x) \cup x)$ where $S \subseteq V$ and $N(x)$ denotes the neighbours of x.
- Let $C^*(G,k)$ denote the maximum number of nodes in graph G covered by selecting k covering nodes i.e. $C^*(G,k) = \max_S \mid cover(G,S) \mid$ where $\mid S \mid = k$.
- Let $S_k^{(g)}$ denote the set of k nodes ($S_k^{(g)} \subset V$) chosen according to the greedy algorithm.

For a graph $G \equiv (V,E)$ partitioned into two subgraphs $G_1 \equiv (V_1,E_1)$ and $G_2 \equiv (V_2,E_2)$, let

- the maximum node degrees for the graphs G_1, G_2 and G be d_1, d_2 and d respectively. Let g_1,g_2 and g be the sizes of the greedy set covers (i.e. covers obtained by the greedy approach) of G_1,G_2 and G respectively. Let $c_1^* = \mid S_1^* \mid$, $c_2^* = \mid S_2^* \mid$ and $c^* = \mid S^* \mid$ be the sizes of the minimum dominating sets of G_1, G_2 and G respectively
- Define the **vertex support of the cut** as the total number of nodes in either partition connected to nodes in the other partition in the original graph. i.e. if $CS = \{s,t\} \in E, \mid s \in V_1, t \in V_2$ denotes the cut set of the partition, and $P = \cup s$, $Q = \cup t$ are the sets of nodes in G_1 and G_2 respectively connected to nodes in the other partition, then

$$vSupCut(V_1,V_2) = \mid P \cup Q \mid = \mid P \mid + \mid Q \mid \tag{1}$$

- Define the **minimum vertex support cut** of a graph $G \equiv (V,E)$ as $minVSupCut(G) = \min_{V_1,V_2} vSupCut(V_1,V_2)\ V_1 \neq \phi, V_2 \neq \phi, V_1 \cap V_2 = V$

2 The Minimum Dominating Set and Maximum Coverage in a problem decomposition context

We define performance ratios for the dominating set and maximum coverage problems as follows. Define $X^{(optimal)}$ as the ratio of the solution obtained by combining the optimal solutions from the individual subgraphs to the optimal solution obtained from the original graph and let

$$\rho^{(optimal)} = min(X^{(optimal)}, 1/X^{(optimal)}) \tag{2}$$

Since computing the optimal solutions in the case of minimum dominating set and maximum coverage is NP-hard, $X^{(optimal)}$ and $\rho^{(optimal)}$ cannot be computed directly for large graphs. Thus we also define an "empirical" performance ratio $\rho^{(greedy)}$ as the ratio of corresponding empirical quantities computed using the greedy algorithm outlined in Cormen *et* al. [2]. Let $G \equiv (V,E)$ be the graph partitioned into $G_1 \equiv (V_1,E_1), \ldots, G_p \equiv (V_p,E_p)$ $(V_1 \cup V_2 \ldots V_p = V$ and

$V_i \cap V_j = \phi, i \neq j$). For the minimum dominating set and the maximum coverage the corresponding expressions are as below, these are discussed in a little more detail in the appendix.

$$\rho_{MDS}^{(optimal)} = 1/X_{MDS}^{(optimal)} = \frac{\mid S^* \mid}{\mid S_1^* \mid + \mid S_2^* \mid \ldots \mid S_p^* \mid} \tag{3}$$

$$\rho_{MC}^{(optimal)} = X_{MC}^{(optimal)} = \frac{\mid cover(G, S_{k_1}^* \cup \ldots S_{k_p}^*) \mid}{\mid cover(G, S_k^*) \mid} \tag{4}$$

For $p = 2$ partitions, the optimal and empirical performance ratios for the minimum dominating set are:

$$\rho_{MDS}^{(optimal)} = \frac{c^*}{c_1^* + c_2^*} \text{ and } \rho_{MDS}^{(greedy)} = \frac{g}{g_1 + g_2} \tag{5}$$

where the symbols are according to notation in section 1.1. Analogous to an empirical performance ratio for the Minimum Dominating Set ($\rho_{MDS}^{(greedy)}$) we define one for the maximum coverage problem as :

$$\rho_{MC}^{(greedy)} = \frac{\mid cover(G_1, S_{k_1}^{(g)}) \mid + \mid cover(G_2, S_{k_2}^{(g)}) \mid}{\mid cover(G, S_k^{(g)}) \mid} \tag{6}$$

2.1 Relating performance ratios to empirically computable quantities

In this section we state propositions relating the performance ratios to quantities that can be empirically computed for a given graph (and its subgraphs), the vertex support of a cut is one such quantity that appears in two of these propositions.

Minimum Dominating Set (MDS) While computing the minimum dominating set is NP-hard in general, bounds may be derived for the performance ratio in terms of quantities that can be computed empirically for a given graph. We state the following propositions, the proofs are given in the appendix.

Proposition 1. *Let $G \equiv (V, E)$ be partitioned into subgraphs $G_1 \equiv (V_1, E_1)$ and $G_2 \equiv (V_2, E_2)$. Then*

$$\frac{1}{1 + \frac{vSupCut(V_1, V_2)H(d)}{g}} \leq \rho_{MDS}^{(optimal)} \leq 1$$

Proposition 2.

$$\frac{\rho_{MDS}^{(greedy)}}{H(d)} \leq \rho_{MDS}^{(optimal)} \leq min(1, \rho_{MDS}^{(greedy)} H(d)) \tag{7}$$

where $\rho_{MDS}^{(greedy)} = \frac{g}{g_1 + g_2}$ and $\rho_{MDS}^{(optimal)}$ and $H(d)$ are as explained earlier. It can also be shown that a tighter upper bound on $\rho_{MDS}^{(optimal)}$ is $\frac{g}{\frac{g_1}{H(d_1)} + \frac{g_2}{H(d_2)}}$.

Maximum Coverage Given graph G and a budget k, we now express lower bounds on the performance ratio $\rho_{MC}^{(optimal)}$ (see (13)) as given by propositions 3 and 4. As before let $G \equiv (V, E)$ be partitioned into $G_1 \equiv (V_1, E_1)$ and $G_2 \equiv (V_2, E_2)$. Let S_k^* be the optimal k-node cover for G. Note that for the max cover problem there is an additional criteria, namely the quota of nodes allocated to G_1 and G_2, let the number of nodes be k_1 and $k_2 = k - k_1$ respectively.

Let $S_{k_1}^{(g)}$ ($S_{k_1}^{(g)} \subset V_1$) be the set of k_1 nodes in G_1 and $S_{k_2}^{(g)}$ be the set of $k_2 = k - k_1$ nodes in G_2 both chosen according to the greedy algorithm. Let $S_1^{'} = S_k^* \cap V_1$ and $S_2^{'} = S_k^* \cap V_2$ be the subsets of S_k^* present amongst V_1 and V_2 respectively. We consider the special case where $k_1 =\mid S_1^{'} \mid$ and $k_2 =\mid S_2^{'} \mid$ i.e. the "budget allocation" to the subgraphs happens to be exactly right by chance. (Note that in practice we do not know $\mid S_1^{'} \mid$ and $\mid S_2^{'} \mid$). Then the following relationships given by propositions 3 and 4 hold.

Proposition 3.

$$1 - \frac{vSupCut(V_1, V_2)}{cover(G, S_k^{(g)})} \leq \rho_{MC}^{(optimal)} \tag{8}$$

Proposition 4.

$$\rho_{MC}^{(greedy)}(1 - 1/e) \leq \rho_{MC}^{(optimal)} \tag{9}$$

where $\rho_{MC}^{(greedy)}$ is as defined in 6.

Summary and implications of Propositions 1 - 4 Proposition 2 and 4 express the bounds on optimal performance ratios for $\rho_{MDS}^{(optimal)}$ and $\rho_{MC}^{(optimal)}$ in terms of the sizes of greedy set covers of the subgraphs and the full graph. Propositions 1 and 3 express the lower bound on the performance ratios for the minimum dominating set and maximum coverage problems respectively, in terms of the *vertex support of the cut*. The analysis of the maximum coverage is more difficult since it depends on how the total quota of nodes ("the budget") is divided amongst the subgraphs. Proposition 3 holds only in the special case when the actual allocation of nodes to each subgraph is same as the optimal allocation (by chance). Note that propositions 1 and 3 imply that minimising $vSupCut$ i.e. $minVSupCut(G)$ improves the lower bound on the optimal performance ratios (although this does not necessarily guarantee an optimal partitioning).

It can be easily shown that $minVSupCut(G)$ is analogous to the well known min cut (we omit this due to space constraints). Although it may be possible to achieve high performance ratios with the min cut, a common problem is that it tends to favour unbalanced partitions, while it is often desirable to have balanced partitions. We subsequently report results obtained from partitioning the graphs using the min cut, ratio cut and normalised cut; the latter two tend to produce more balanced partitions.

3 Experiments

We illustrate a few representative results on synthetic and real datasets, the graphs varied in size with the number of nodes ranging from a few hundred to a

few thousand. For the real data we used **co-citation graphs** from bibliography of fifteen years of **Case Based Reasoning (CBR) conferences** [1] For the synthetic data we generated power law graphs, they are described briefly below and in detail in the appendix.

The basic statistics of the graphs used in our experiments are summarised in table 1.

Powerlaw graphs In order to construct synthetic graphs that approximate real world power-law graphs, random graphs with a given fixed input degree sequence $(d_1 \geq d_2, \ldots, d_n)$ were generated and the degree sequence was chosen to follow an exact power law as given by : $d_k = round\left(\left(\frac{k}{n}\right)^{\alpha} d_{min}\right)$ where d_{min} = minimum node degree

We generated two sets of powerlaw graphs for our experiments, the parameter values used were ($\alpha = 5$,$d_{min} = 8$) and ($\alpha = 10$,$d_{min} = 8$). For each of these sets, power law graphs consisting of different numbers of nodes ($n = 1000$, 2000, 5000 and 10000) were generated. For each value of n (number of nodes) 50 powerlaw graphs were generated and the experiments were repeated on each of the 50 graphs. The min cut, the ratio cut and normalised cuts are commonly used graph cuts, also note that $minSupCut$ and $NrSupCut$ are closely related to the min cut and ratio cut respectively as described in the appendix. While the min cut achieves high performance ratios as defined in (5) and (6), a common problem is that it often produces highly unbalanced partitions, this is evident in table 2(a) for instance. The ratio and normalised cuts are preferred in many applications since they produce balanced partitions.

Also we observed in our experiments (see the corresponding rows in table 2(b,c) for instance) that the ratio cut may sometimes produce low empirical performance ratios, on the other hand the normalised cut consistently yielded high performance ratios including in those cases where the ratio cut performed poorly. For these reasons we mostly report results corresponding to the normalised cut.

We used the software CMINUCUT which implements the algorithm proposed by Hao and Orlin [5] to compute the min cut. While computing the exact optimal ratio and normalised cuts are NP-hard, relaxations of these cuts can be formulated as eigenvalue problems. For the normalised cut we used the software Graclus which implements the multi-level approach proposed in [3], one main advantage of this software is that it can compute the normalised cut without a computationally intensive eigenvalue decomposition. We describe experimental results pertaining to computation of empirical performance ratios from subgraphs obtained by partitioning the original graph. The results shown in tables below correspond to $p = 2$ partitions, the empirical performance ratios ($\rho_{MDS}^{(greedy)}$ and $\rho_{MC}^{(greedy)}$) are reported in the last columns of the tables. For the real graphs the empirical performance ratios were computed using the actual empirical quantities for the corresponding graphs, for the power law graphs

[1] publicly available for research purposes, can be downloaded from http://mlg.ucd.ie/cbr

# nodes	$\alpha = 5, d_{min} = 8$		$\alpha = 10, d_{min} = 8$	
	Average # edges	Average highest degree	Average # edges	Average highest degree
1000	4978	32	4417	16
2000	9965	37	8837	17
5000	24922	44	22095	19
10000	44856	50	44195	20

(a)

Graph description	# nodes	# edges
CBR Co-citation (Small)	247	8055
CBR Co-citation (Full)	657	24682

(b)

Table 1. Basic statistics of simulated power law graphs and real graphs (the largest connected component in each case) used in our experiments. (a) Power law graphs generated according to (40) Columns 2-3 : $d_{min} = 8$, $\alpha = 5$ Columns 4-5 : $d_{min} = 8$, $\alpha = 10$. (b) Real graphs derived from bibliographic datasets

the values averaged over 50 runs were used (for example for the MDS problem $\rho_{MDS}^{(greedy)} = \frac{g}{g_1+g_2}$ for the real graphs and $\rho_{MDS}^{(greedy)} = \frac{g^{(avg)}}{g_1^{(avg)}+g_2^{(avg)}}$ for power law graphs). For the maximum coverage problem, the number of covering nodes allocated to each subgraph was proportional to the size of the subgraph (number of nodes in the subgraph). Assume $G = (V, E)$ is partitioned into subgraphs $G_1 = (V_1, E_1)$ and $G_2 = (V_2, E_2)$ $(V_1 \cup V_2 = V)$. Let k be the number of covering nodes for the full graph. The number of covering nodes allocated to subgraphs G_1 and G_2 were $k_1 = round(k \mid V_1 \mid / \mid V \mid)$, $k_2 = round(k \mid V_2 \mid / \mid V \mid$ where $\mid V \mid, \mid V_1 \mid, \mid V_2 \mid$ are the number of vertices in graph G and subgraphs G_1 and G_2 respectively.

CBR graphs Table 2 shows the results corresponding to CBR graphs. Table 2(a) shows number of nodes in the $k = 2$ subgraphs obtained by partitioning the graphs using the min, ratio and normalised cuts respectively, the min cut often produces unbalanced partitions as evident from the table. Tables 2(b) and 2(c) show the results pertaining to the CBR graphs corresponding to $\rho_{MDS}^{(greedy)}$ and $\rho_{MC}^{(greedy)}$ respectively. While the min cut yields high performance ratios, this is due to highly unbalanced partitions,(for example in each of the CBR graphs one of the partitions consists of a single node).

Powerlaw graphs Tables 3 and 4 show the results pertaining to $\rho_{MDS}^{(greedy)}$ and $\rho_{MC}^{(greedy)}$ for graphs consisting of 1000 and 2000 nodes using the ratio and normalised cuts respectively . For each number of nodes (say 1000), the results averaged over 50 runs are shown. The numbers shown in the columns except the first and the last are the mean (standard deviation) of the respective quantities. The normalised cut provides good emprical performance ratios in most cases. These are shown in the last columns of the respective tables.

We observe from these tables, that for the power law gaphs the performance ratios obtained using the ratio cut were very similar to those obtained using normalised cut; however for the CBR graphs the performance ratios corresponding to the ratio cut were inferior to those corresponding to the normalised cut. In

Graph	Cut	n_1	n_2
CBR Cocitation (Small)	Min	246	1
	Ratio	123	124
	Normalised	102	145
CBR Cocitation (Full)	Min	656	1
	Ratio	328	329
	Normalised	288	369

(a)

Graph	g	**Cut**	g_1	g_2	$\rho_{MDS}^{(greedy)}$
CBR Cocitation (Small)	11	Min	11	1	0.9167
		Ratio	19	2	**0.5238**
		Normalised	7	6	0.84615
CBR Cocitation (Full)	27	Min	27	1	0.9643
		Ratio	5	66	**0.3802**
		Normalised	13	20	0.8181

(b)

Graph	Full graph	**Cut**	Sub graph 1	Sub graph 2	$\rho_{MC}^{(greedy)}$
	$(k, \mid C(G, S_k^{(g)}) \mid)$		$(k_1, \mid C(G_1, S_{k_1}^{(g)}) \mid)$	$(k_2, \mid C(G_2, S_{k_2}^{(g)}) \mid)$	
CBR Cocitation Small	(10,246)	Min	(10,246)	(0,0)	1
		Ratio	(5,41)	(5,115)	**0.6341**
		Normalised	(5,125)	(5,117)	0.9837
CBR Cocitation Full	(10,619)	Min	(10,619)	(0,0)	1
		Ratio	(5,328)	(5,174)	0.8109
		Normalised	(6,360)	(4,240)	0.969

(c)

Table 2. Results for CBR graphs, partitioned using **min cut,ratio cut and normalised cut** respectively. (a) Sizes of subgraphs obtained from partitioning (b) $\rho_{MDS}^{(greedy)} = \frac{g}{g_1+g_2}$ (c) $\rho_{MC}^{(greedy)} = \frac{|C(G_1,S_{k_1}^{(g)})|+|C(G_2,S_{k_2}^{(g)})|}{|C(G,S_k^{(g)})|}$

almost all our results (may results omitted for the sake of conciseness) we found that the normalised cut yielded good performance ratios.

4 Conclusions and future work

In this work we examine the minimum dominating set and maximum coverage problems, in a problem decomposition context. We posed the question that given a graph and subgraphs obtained by partitioning it, how close is the combined solution from the subgraphs to that which can be obtained from the original graph. Towards this end we define optimal and empirical performance ratios as benchmarks for assessing the quality of a given partitioning. We address the above question both analytically and experimentally and provide a few initial insights. For the case of two partitions we show that a *minimum vertex support cut* maximises a lower bound on the corresponding empirical performance ratios, for the minimum dominating set and also a special case of the maximum coverage. Future work includes obtaining tighter bounds on "optimal performance ratios". Another direction is investigating different graph partitioning schemes. In our experiments the normalized cut consistently provided a high empirical performance ratio, we suggest that it may also be a "good partitioning" with respect to the optimal performance ratio, deriving analytical results is another interesting question for future investigation.

Graph Parameters	Full graph # nodes	Mean (std) g	Sub graph 1 Mean (std) g_1	Sub graph 2 Mean (std) g_2	$\rho_{MDS}^{(greedy)} = \frac{g^{(avg)}}{g_1^{(avg)}+g_2^{(avg)}}$
$\alpha = 5$, $d_{min} = 8$	1000	154.92 (2.75)	101.22 (2.89)	101.98 (2.85)	0.7627
	2000	310.68 (3.80)	203.45 (4.24)	201.70 (4.06)	0.7663
$\alpha = 10$, $d_{min} = 8$	1000	169.92 (2.11)	107.84 (2.66)	108.5 (2.93)	0.7856
	2000	339.48 (2.89)	215.72 (3.26)	215.8 (3.74)	0.7868

(a)

Graph Parameters	Full graph # nodes	k	Mean (std) $\mid C(G, S_k^{(g)}) \mid$	Sub graph 1 Mean (std) $\mid C(G_1, S_{k_1}^{(g)}) \mid$	Sub graph 2 Mean (std) $\mid C(G_2, S_{k_2}^{(g)}) \mid$	$\rho_{MC}^{(greedy)} =$
$\alpha = 5$, $d_{min} = 8$	1000	10	179.36 (5.43)	68.92 (5.66)	68.04 (5.52)	0.7641
		100	899.84 (5.22)	399.30 (5.78)	398.58 (5.11)	0.8867
	2000	10	205.60 (6.14)	75.03 (5.84)	76.30 (6.43)	0.7362
		100	1202.25 (7.40)	505.30 (7.56)	506.40 (8.21)	0.8415
$\alpha = 10$, $d_{min} = 8$	1000	10	133.88 (2.30)	55.85 (2.26)	54.73 (1.71)	0.8261
		100	856.15 (3.39)	383.00 (4.44)	381.43 (3.27)	0.8929
	2000	10	141.62 (2.43)	57.92 (2.36)	58.75 (2.16)	0.8240
		100	1065.65 (5.88)	463.82 (4.78)	466.02 (5.19)	0.8726

(b)

Table 3. Empirical performance ratios for power law graphs partitioned using the **ratio cut**. Table (a) : ($\rho_{MDS}^{(greedy)}$) Table (b) : $\rho_{MC}^{(greedy)}$

References

1. A. L. Barabasi and R. Albert. Emergence of scaling in random networks. *Science*, 286:509–512, 1999.
2. T. H. Cormen, C. E. Leiserson, R. L. Rivest, and C. Stein. *Introduction to Algorithms*. MIT Press, Cambridge,Massachussets,USA, 2001.
3. Inderjit S. Dhillon, Yuqiang Guan, and Brian Kulis. Weighted graph cuts without eigenvectors a multilevel approach. *IEEE Trans. Pattern Anal. Mach. Intell.*, 29(11):1944–1957, 2007.
4. D. Greene, J. Freyne, B. Smyth, and P. Cunningham. An analysis of research themes in the cbr conference literature. In *Proc. 9th European Conference on Case-Based Reasoning (ECCBR 2008)*, 2008.
5. J. Hao and J.B. Orlin. A faster algorithm for finding the minimum cut in a graph. In *Proc. of the 3rd Annual ACM-SIAM Symposium on Discrete Algorithms*, pages 165–174, Orlando, Florida, 1992.
6. G. Markus. Co-citation analysis and the search for invisible colleges : A methodological evaluation. *Scientometrics*, 57(1):27–57, 2003.
7. G. Nemhauser, L. Wolsey, and M. Fisher. An analysis of the approximations for maximizing submodular set functions. *Mathematical Programming*, 14:265–294, 1978.
8. M. Newman. The structure of scientific collaboration networks. *Proc. Natl. Acad. Sci.*, 98, 2001.

Acknowledgements

This work was supported by Enterprise Ireland Grant No. PC/2007/010. The author would like to thank Dr. Neil Hurley for providing the code related to

Graph parameters	Full graph # nodes	Mean (std) g	Sub graph 1 Mean (std) g_1	Sub graph 2 Mean (std) g_2	$\rho_{MDS}^{(greedy)} = \frac{g^{(avg)}}{g_1^{(avg)}+g_2^{(avg)}}$
$\alpha = 5$	1000	154.92 (2.75)	99.52 (7.33)	103.50 (6.88)	0.7633
$d_{min} = 8$	2000	310.70 (3.80)	200.48 (15.00)	208.92 (13.69)	0.7591
$\alpha = 10$	1000	171.92 (2.18)	106.56 (7.06)	105.52 (6.27)	0.811
$d_{min} = 8$	2000	332.12 (3.55)	217.720 (8.45)	215.68 (8.45)	0.766

(a)

Graph parameters	Full graph # nodes	k	Mean (std) $\mid C(G, S_k^{(g)}) \mid$	Sub graph 1 Mean (std) $\mid C(G_1, S_{k_1}^{(g)}) \mid$	Sub graph 2 Mean (std) $\mid C(G_2, S_{k_2}^{(g)}) \mid$	$\rho_{MC}^{(greedy)}$
$\alpha = 5$	1000	10	179.36	74.06	65.16	0.7763
$d_{min} = 8$		100	899.84	391.94	382.06	0.8601
	2000	10	205.42	82.3	73.46	0.7588
		100	1202.48	495.48	481.9	0.8128
$\alpha = 10$	1000	10	133.54	54.8	54.52	0.8188
$d_{min} = 8$		100	855.8	374.82	366.58	0.8663
	2000	10	141.64	58.98	58.96	0.8329
		100	1065.22	449.02	446.36	0.84059

(b)

Table 4. Empirical performance ratios for power law graphs partitioned using the **normalised cut**. Table (a) : ($\rho_{MDS}^{(greedy)}$) Table (b) : $\rho_{MC}^{(greedy)}$

generating power law graphs. The author would also like to thank Prof. Pádraig Cunningham and Dr. Derek Greene for useful feedback on an earlier version of the ideas described in this manuscript.

Appendix

Defining performance ratios for the dominating set and maximum coverage problems

Define $X^{(optimal)}$ as the ratio of the solution obtained by combining the optimal solutions from the individual subgraphs to the optimal solution obtained from the original graph and let

$$\rho^{(optimal)} = min(X^{(optimal)}, 1/X^{(optimal)}) \tag{10}$$

Since computing the optimal solutions in the case of minimum dominating set and maximum coverage is NP-hard, $X^{(optimal)}$ and $\rho^{(optimal)}$ cannot be computed directly. We also define an "empirical" performance ratio $\rho^{(greedy)}$ as the ratio of corresponding empirical quantities computed using the greedy algorithm outlined in Cormen *et* al. [2].

Let $G \equiv (V, E)$ be the graph partitioned into $G_1 \equiv (V_1, E_1), \ldots, G_p \equiv (V_p, E_p)$ $(V_1 \cup V_2 \ldots V_p = V$ and $V_i \cap V_j = \phi, i \neq j)$. The expressions for the Minimum Dominating Set and Maximum Coverage partitions are as follows:

1. **Minimum Dominating Set** Let S_1^*, S_2^*, ..., S_p^* and S^* be the optimal (smallest) dominating sets of G_1 and G_2, ..., G_p and G respectively. Define $X_{MDS}^{(optimal)} = \frac{|S_1^* \cup S_2^* \ldots \cup S_p^*|}{|S^*|}$ Note that since S_1^*, S_2^*, S_p^* are disjoint sets and $X_{MDS}^{(optimal)} \geq 1$,

$$\rho_{MDS}^{(optimal)} = 1/X_{MDS}^{(optimal)} = \frac{\mid S^* \mid}{\mid S_1^* \mid + \mid S_2^* \mid \ldots \mid S_p^* \mid} \tag{11}$$

   For $p = 2$ partitions, the optimal and empirical performance ratios are:

$$\rho_{MDS}^{(optimal)} = \frac{c^*}{c_1^* + c_2^*} \text{ and } \rho_{MDS}^{(greedy)} = \frac{g}{g_1 + g_2} \tag{12}$$

   where, $c_1^* = \mid S_1^* \mid$, $c_2^* = \mid S_2^* \mid$ and $c^* = \mid S^* \mid$ are the sizes of the minimum dominating sets of G_1, G_2 and G respectively and g_1, g_2 and g are sizes of dominating sets obtained by the greedy algorithm Note that while $\rho_{MDS}^{(optimal)}$ is always ≤ 1, $\rho_{MDS}^{(greedy)}$ could exceed 1.
2. **Maximum coverage** For the maximum coverage, the given inputs are the graph G and a budget k. There is an additional criterion, namely the allocation of budgets i.e. the number of covering nodes allocated to $G_1, G_2, \ldots, G_p$ let these be $k_1, k_2, \ldots, k_p$ respectively $(\sum_i^p k_i = k)$. Let $S_{k_1}^* \subseteq V_1, \ldots, S_{k_p}^* \subseteq V_p$ be the sets of nodes which form the optimal $k_1, \ldots, k_p$-element optimal covers in $G_1, \ldots, G_p$ respectively. Let S_k^* be the optimal k-element cover for G.

We define the objective function as, $X_{MC}^{(optimal)} = \frac{|cover(G, S_{k_1}^* \cup \ldots S_{k_p}^*)|}{|cover(G, S_k^*)|}$, the corresponding performance ratio is :

$$\rho_{MC}^{(optimal)} = X_{MC}^{(optimal)} = \frac{\mid cover(G, S_{k_1}^* \cup \ldots S_{k_p}^*) \mid}{\mid cover(G, S_k^*) \mid} \tag{13}$$

Note that $\rho_{MC}^{(optimal)} (= X_{MC}^{(optimal)}) \leq 1$, since S_k^* is the k-element set of nodes that covers the largest number of nodes in G. Note that $\rho_{MC}^{(optimal)}$ depends on not just the graph but on k and $k_1, \ldots, k_p$, strictly speaking it must be denoted by $\rho_{MC}^{(optimal)}(G, k, k_1, \ldots, k_p)$; however for simplicity of notation we drop ks.

Proof of propositions outlined in the paper

We prove the propositions stated in the paper. The proofs use the following results in the literature, we briefly outline them here :
Minimum Dominating Set : Let c^* be the size of an optimal (the smallest) dominating set and g the size of the dominating set obtained using the greedy algorithm. It can be proved that the greedy set cover algorithm returns a set cover whose size is at most $H(d_{max})$ times the size of an optimal (the smallest) set cover where d_{max} is the cardinality of the largest set and $H(d)$ is the dth harmonic number. The reader is referred to [2] for a description and related analysis. This result in [2] expressing the size of the greedy set cover in terms of the optimal set cover can be written as $c^* \geq \frac{g}{H(d)}$ where d is the highest degree and $H(d) = \sum_{i=1}^{d} 1/i$.
Maximum Coverage : Nemhauser *et al.* [7] show that the greedy algorithm provides a value within $(1 - 1/e)$ of the optimal for *sub modular functions*. This result can be expressed as :

$$\mid cover(G, S_k^{(g)}) \mid \geq (1 - 1/e) \mid cover(G, S_k^*) \mid \tag{14}$$

where $cover(.,.), S_k^{(g)}$ and S_k^* are described in section 1.1.
Proof of proposition 1:

Proof. To prove the above proposition we derive bounds for $X^{(optimal)} = \frac{c_1^* + c_2^*}{c^*}$ (note that for the MDS problem $\rho_{MDS}^{(optimal)} = 1/X^{(optimal)}$. It is obvious that the smallest possible value of $X^{(optimal)}$ is 1 since by definition c^* is the optimal dominating set of the whole graph. Hence $X^{(optimal)} \geq 1$.

We derive the upper bound on $X^{(optimal)}$ as below.

- Let S^* be the set of nodes of the minimum dominating set.
- Let $S^{'}$ and $S^{''}$ be the nodes of S^* present in G_1 and G_2 respectively i.e. $S^{'} = S^* \cap V_1$, $S^{''} = S^* \cap V_2$ and $S^{'} \cup S^{''} = S^*$). Let $c^{'} = \mid S^{'} \mid$ and $c^{''} = \mid S^{''} \mid$.

– Let P and Q be the sets of all nodes in G_1 and G_2 connected to nodes in the other partition. Let $\mid P \mid = p$ and $\mid Q \mid = q$ i.e. p nodes of G_1 are connected to q nodes of G_2 in the original graph G.

All nodes in G_1 except possibly the set of nodes P are covered by the set of nodes $S^{'}$ since none of those are connected to any node in G_2. Thus $S^{'} \cup P$ is a dominating set of G_1. Hence $c_1^* \leq \mid S^{'} \mid + \mid P \mid$ i.e.

$$c_1^* \leq c^{'} + p \tag{15}$$

Similarly $S^{''} \cup Q$ is a dominating set of G_2 and thus :

$$c_2^* \leq c^{''} + q \tag{16}$$

From 15 and 16 and noting that $c^{'} + c^{''} = c^*$, we get

$$\begin{aligned} c_1^* + c_2^* &\leq c^{'} + p + c^{''} + q \\ &= c^* + p + q \end{aligned} \tag{17}$$

Noting that $p + q = vSupCut(V_1, V_2)$ we have

$$X^{(optimal)} = \frac{c_1^* + c_2^*}{c^*} \leq 1 + \frac{vSupCut(V_1, V_2)}{c^*} \leq 1 + \frac{vSupCut(V_1, V_2)H(d)}{g} \tag{18}$$

since $c^* \geq \frac{g}{H(d)}$. Taking the reciprocals of the relevant quantities we get the bounds on $\rho_{MDS}^{(optimal)}$.

Proof of proposition 2:

Proof. Since c^* is the size of the optimal (smallest) set cover, it is less than the sum of the optimal set covers of the sub graphs (true by definition). Hence,

$$c^* \leq c_1^* + c_2^* \tag{19}$$

Thus 1 is a trivial upper bound on $\rho_{MDS}^{(optimal)} = \frac{c^*}{c_1^* + c_2^*}$.

Let LB_1, LB_2, LB be lower bounds for c_1^*, c_2^* and c^* respectively. Similarly let UB_1, UB_2, UB be upper bounds. It is easily seen that

$$\frac{LB}{UB_1 + UB_2} \leq \frac{c^*}{c_1^* + c_2^*} \leq \frac{UB}{LB_1 + LB_2} \tag{20}$$

We note that the sizes of the optimal set covers are at most the sizes of the corresponding greedy set covers. Hence we have,

$$c_1^* \leq g_1,\ c_2^* \leq g_2 \text{ and } c^* \leq g \tag{21}$$

Also from the basic result on the size of the greedy set cover ([2]) we have

$$\frac{g_1}{H(d_1)} \leq c_1^*,\ \ \frac{g_2}{H(d_2)} \leq c_2^* \text{ and } \frac{g}{H(d)} \leq c^* \tag{22}$$

From 21 and 22 we have,

$$LB_1 = \frac{g_1}{H(d_1)},\ UB_1 = g_1\ LB_2 = \frac{g_2}{H(d_2)},\ UB_2 = g_2\ LB = \frac{g}{H(d)},\ UB = g \quad (23)$$

Substituting for the lower and upper bounds from 23 in 20 we get the required result, i.e.

$$\frac{c^*}{c_1^* + c_2^*} \leq \frac{g}{\frac{g_1}{H(d_1)} + \frac{g_2}{H(d_2)}}$$
$$\text{and } \frac{\frac{g}{H(d)}}{g_1 + g_2} \leq \frac{c^*}{c_1^* + c_2^*} \quad (24)$$

The expressions for the lower and upper bounds can be simplified as follows. Note that $d \geq d_1$ and $d \geq d_2$ and hence $H(d) \geq H(d_1)$ and $H(d) \geq H(d_2)$ since $H(.)$ is monotonic. Replacing $H(d)$ in place of $H(d_1)$ and $H(d_2)$ in 24 gives a simpler (and a more conservative) expression for the lower bound as $\frac{g_1+g_2}{g}\frac{1}{H(d)}$, since

$$\frac{g_1}{H(d_1)} + \frac{g_2}{H(d_2)} \geq \frac{g_1 + g_2}{H(d)}$$

Using the more conservative lower bound, (24) can be written as :

$$\frac{\rho_{MDS}^{(greedy)}}{H(d)} \leq \frac{c^*}{c_1^* + c_2^*} \leq H(d)\rho_{MDS}^{(greedy)} \quad (25)$$

where

$$\rho_{MDS}^{(greedy)} = \frac{g}{g_1 + g_2}$$

and $H(d)$ is as explained in the paper. Thus

$$\frac{\rho_{MDS}^{(greedy)}}{H(d)} \leq \rho_{MDS}^{(optimal)} \leq min(1, \rho_{MDS}^{(greedy)} H(d))$$

since 1 is a trivial upper bound.

Propositions 3 and 4

For the proofs of propositions 3 and 4, as before let $G = (V, E)$ be partitioned into $G_1 = (V_1, E_1)$ and $G_2 = (V_2, E_2)$. Let S^* denote the optimal k node cover of G. Let $S_1^{'} = S^* \cap V_1$ and $S_2^{'} = S^* \cap V_2$ be the subsets of nodes of S^* present in graph G_1 and G_2 respectively. Let S_1^* and S_2^* be the optimal max covers for graphs G_1 and G_2. Note that for the max cover problem there is an additional criteria, namely the quota of nodes allocated to G_1 and G_2 (i.e. $\mid S_1^* \mid$ and $\mid S_2^* \mid$).

Proof of proposition 3

Consider the special case where $\mid S_1^* \mid = \mid S_1^{'} \mid$ and $\mid S_2^* \mid = \mid S_2^{'} \mid$.
(Note that in practice we do not know $\mid S_1^{'} \mid$ and $\mid S_2^{'} \mid$).
Let $S^{(g)}, S_1^{(g)}$ and $S_2^{(g)}$ be the sets of nodes from graphs G_1 and G_2 obtained by the greedy algorithm, where $\mid S^{(g)} \mid = k, \mid S_1^{(g)} \mid = \mid S_1^{'} \mid$ and $\mid S_2^{(g)} \mid = \mid S_2^{'} \mid$.

It is easy to see that the upper bound for $\rho_{MC}^{(optimal)}$ is 1 since S^* is the optimal k node cover for G. We derive the lower bound on $\rho_{MC}^{(optimal)}$ as follows.
It is easily seen that for any set of nodes X and Y the following holds.

$$\begin{aligned} cover(G_1, X) &= cover(G_1 - P, X) \cup cover(P, X) \\ cover(G_2, Y) &= cover(G_2 - Q, Y) \cup cover(Q, Y) \end{aligned} \tag{26}$$

where - denotes set difference.

As before let P be the set of all nodes in G_1 which are connected to one or more nodes in G_2 in the original graph G and let Q comprise the set of nodes in G_2 connected to one or more nodes in G_1. From 26 and noting that $G_1 - P$ and P are disjoint sets we have,

$$| \, cover(G_1, X) \, | = | \, cover(G_1 - P, X) \, | + | \, cover(P, X) \, |$$

Using this we write down the following relationships as below.

$$\begin{aligned} | \, cover(G_1 - P, S_1^{'}) \, | &= | \, cover(G_1, S_1^{'}) \, | - | \, cover(P, S_1^{'}) \, | \\ | \, cover(G_2 - P, S_2^{'}) \, | &= | \, cover(G_2, S_2^{'}) \, | - | \, cover(P, S_2^{'}) \, | \\ | \, cover(G_1 - P, S_1^{*}) \, | &= | \, cover(G_1, S_1^{*}) \, | - | \, cover(P, S_1^{*}) \, | \\ | \, cover(G_2 - P, S_2^{*}) \, | &= | \, cover(G_2, S_2^{*}) \, | - | \, cover(P, S_2^{*}) \, | \end{aligned} \tag{27}$$

We have,

$$\begin{aligned} | \, cover(G, S_1^{'} \cup S_2^{'}) \, | = | \, cover(G_1 - P, S_1^{'}) \, | + | \, cover(G_2 - Q, S_2^{'}) \, | \\ + | \, cover(P \cup Q, S_1^{'} \cup S_2^{'}) \, | \end{aligned} \tag{28}$$

Similarly,

$$\begin{aligned} | \, cover(G, S_1^{*} \cup S_2^{*}) \, | = | \, cover(G_1 - P, S_1^{*}) \, | + | \, cover(G_2 - Q, S_2^{*}) \, | \\ + | \, cover(P \cup Q, S_1^{*} \cup S_2^{*}) \, | \end{aligned} \tag{29}$$

Substituing from 27 in 28 and 29 we get :

$$\begin{aligned} | \, cover(G, S_1^{'} \cup S_2^{'}) \, | &= | \, cover(G_1, S_1^{'}) \, | - | \, cover(P, S_1^{'}) \, | \\ &+ | \, cover(G_2, S_2^{'}) \, | - | \, cover(Q, S_2^{'}) \, | \\ &+ | \, cover(P \cup Q, S_1^{'} \cup S_2^{'}) \, | \end{aligned} \tag{30}$$

$$\begin{aligned} | \, cover(G, S_1^{*} \cup S_2^{*}) \, | &= | \, cover(G_1, S_1^{*}) \, | - | \, cover(P, S_1^{*}) \, | \\ &+ | \, cover(G_2, S_2^{*}) \, | - | \, cover(Q, S_2^{*}) \, | \\ &+ | \, cover(P \cup Q, S_1^{*} \cup S_2^{*}) \, | \end{aligned} \tag{31}$$

(30) - (31) gives :

$$| cover(G, S_1^{'} \cup S_2^{'}) | - | cover(G, S_1^{*} \cup S_2^{*}) | = t_1 + t_2 + t_3 - t_4 \qquad (32)$$

where,

$$\begin{aligned} t_1 &= | cover(G_1, S_1^{'}) | - | cover(G_1, S_1^{*}) | \\ t_2 &= | cover(G_2, S_2^{'}) | - | cover(G_2, S_2^{*}) | \\ t_3 &= | cover(P \cup Q, S_1^{'} \cup S_2^{'}) | - (| cover(P, S_1^{'}) | + | cover(Q, S_2^{'}) |) \\ t_4 &= | cover(P \cup Q, S_1^{*} \cup S_2^{*}) | - (| cover(P, S_1^{*}) | + | cover(Q, S_2^{*}) |) \end{aligned}$$

- Since S_1^* constitutes the optimal k_1 node cover for G_1 we have

$$t_1 = | cover(G_1, S_1^{'}) | - | cover(G_1, S_1^{*}) | \leq 0$$

- Similarly $t_2 \leq 0$
- $t_4 \geq 0$ since $S_1^* \cup S_2^*$ is guaranteed to cover at least as many nodes in $P \cup Q$ as the sum of nodes covered individually by S_1^* in P and S_2^* in Q.
- t_3 can at most be the total number of nodes in $P \cup Q$. Hence

$$t_3 \leq P \cup Q = | P | + | Q |$$

since P and Q are disjoint sets.

Plugging in the separate maximum values for t_1, t_2, t_3 and the minimum value for t_4 in (32) we get

$$| cover(G, S_1^{'} \cup S_2^{'}) | - | cover(G, S_1^{*} \cup S_2^{*}) | \leq p + q \qquad (33)$$

where $p = | P |$ and $q = | Q |$. Noting that $S_1^{'} \cup S_2^{'}$ is indeed S^* and dividing both sides of (33) by $| cover(G, S^*) |$ we have :

$$1 - \frac{| cover(G, S_1^{*} \cup S_2^{*}) |}{| cover(G, S^*) |} \leq \frac{p+q}{| cover(G, S^*) |} \qquad (34)$$

We make two minor observations.

- The LHS of (34) is $1 - \rho_{MC}^{(optimal)}$.
- Also $| cover(G, S^*) | \geq | cover(G, S^{(g)}) |$, hence

$$\frac{p+q}{| cover(G, S^*) |} \leq \frac{p+q}{| cover(G, S^{(g)}) |}$$

Therefore we have,

$$1 - \rho_{MC}^{(optimal)} \leq \frac{p+q}{| cover(G, S^*) |} \leq \frac{p+q}{| cover(G, S^{(g)}) |}$$

and hence

$$1 - \frac{p+q}{\mid cover(G, S^{(g)}) \mid} \leq \rho_{MC}^{(optimal)}$$

thus proving the proposition.

Proposition 4

Let the number of nodes to be selected from the full graph be k. Let the quota of nodes allocated to subgraphs G_1 and G_2 be k_1 and k_2 respectively $(k_1 + k_2 = k)$. Let $S^{(g)}, S_1^{(g)}$ and $S_2^{(g)}$ be the sets of nodes from graphs G_1 and G_2 obtained by the greedy algorithm, hence $\mid S^{(g)} \mid = k, \mid S_1^{(g)} \mid = k_1$ and $\mid S_2^{(g)} \mid = k_2$. Define $\tilde{\rho}_{MC}$ as :

$$\tilde{\rho}_{MC} = \frac{\mid cover(G_1, S_1^*) \mid + \mid cover(G_2, S_2^*) \mid}{\mid cover(G, S^*) \mid}$$

We note that

$$\mid cover(G_1, S_1^*) \mid + \mid cover(G_2, S_2^*) \mid \leq \mid cover(G, S_1^* \cup S_2^*) \mid \tag{35}$$

since $S_1^* \cup S_2^*$ is guaranteed to cover at least as many elements in G as the sum of number of nodes covered separately in G_1 and G_2 by S_1^* and S_2^* respectively. Dividing both sides of (35) by $\mid cover(G, S^*) \mid$ we get $\tilde{\rho}_{MC} \leq \rho_{MC}^{(optimal)}$. Hence a lower bound on $\tilde{\rho}_{MC}$ is also a lower bound (a more conservative one) on $\rho_{MC}^{(optimal)}$.

Recall the expression below which is a consequence of the well known result on sub modular functions by Nemhauser et al. [7]:

$$\mid cover(G, S^{(g)}) \mid \leq \mid cover(G, S^*) \mid \leq \frac{\mid cover(G, S^{(g)}) \mid}{1 - 1/e} \tag{36}$$

Similarly for the two subgraphs G_1 and G_2 we have,

$$\mid cover(G_1, S_1^{(g)}) \mid \leq \mid cover(G_1, S_1^*) \mid \leq \frac{\mid cover(G_1, S_1^{(g)}) \mid}{1 - 1/e} \tag{37}$$

$$\mid cover(G_2, S_2^{(g)}) \mid \leq \mid cover(G_2, S_2^*) \mid \leq \frac{\mid cover(G_2, S_2^{(g)}) \mid}{1 - 1/e} \tag{38}$$

Similar to the proof of proposition 2, the above relations may be written as :

$$\begin{aligned} LB_1 \leq \mid cover(G_1, S_1^*) \mid \leq UB_1 \\ LB_2 \leq \mid cover(G_2, S_2^*) \mid \leq UB_2 \\ LB \leq \mid cover(G, S^*) \mid \leq UB \end{aligned}$$

where LB_1, LB_2, LB are the lower bounds on $cover(G_1, S_1^*), cover(G_2, S_2^*)$ and $cover(G, S^*)$ respectively. As in (20) we get :

$$\frac{LB_1 + LB_2}{UB} \leq \frac{\mid cover(G_1, S_1^*) \mid + \mid cover(G_2, S_2^*) \mid}{\mid cover(G, S^*) \mid}$$

Plugging the lower bounds from (37),(38) and upper bound from (36) we get:

$$(1-1/e)\rho_{MC}^{(greedy)} \leq \tilde{\rho}_{MC}$$

since $\tilde{\rho}_{MC} = \frac{|cover(G_1,S_1^{(g)})|+|cover(G_2,S_2^{(g)})|}{|cover(G,S_k^{(g)})|}$. Since $\tilde{\rho}_{MC} \leq \rho_{MC}^{(optimal)}$ we have the desired result, namely

$$(1-1/e)\rho_{MC}^{(greedy)} \leq \rho_{MC}^{(optimal)}$$

Description of graphs used in our experiments

Synthetic graphs : Power law graphs

It is often observed that for many real graphs the degree distribution follows a power law rather than a Poisson distribution [1]. Power law graphs are characterised by a significantly higher probability of nodes with large degrees as compared to a random graph. These nodes represent *hubs* which have a significant impact on overall connectivity of a graph, since a connected set of hubs can provide short paths between a large proportion of nodes in the network. Other characteristics often associated with power law graphs are high cluster coefficient and a scale-free property i.e. an observation of certain properties at different scales.

The degree sequence of a graph is the set of node degrees $(d_1, d_2, \ldots, d_n)$ ordered such that $d_1 \geq \ldots \geq d_n$. To construct synthetic graphs that approximate real world power-law graphs, random graphs with a given fixed input degree sequence were generated and the degree sequence was chosen to follow an exact power law as given by : For $k = 1, \ldots, n$, node degrees d_k were chosen such that

$$d_k = round\,(ck^{\alpha}) \tag{39}$$

The constant of proportionality c was set by specifying the minimum degree $d_n = d_{min}$, this yields

$$d_k = round\left(\left(\frac{k}{n}\right)^{\alpha} d_{min}\right) \text{ where } d_{min} = \text{minimum node degree} \tag{40}$$

Real-world graphs do not exhibit the perfect power-law characteristics of these synthetic graphs, but rather tend to exhibit a power-law behaviour in certain ranges of node degrees. Nevertheless, this is a useful approximation that allows us to examine algorithms on reasonably large-scale graphs which exhibit some of the characteristics shown by real-world graphs.

Real graphs : Graphs from bibliographic data

CBR dataset
It is often argued that co-authorship networks capture many key features of social

networks in general(eg. [8]). Also co-citation analysis has become the dominant method for the empirical study of the structures of scientific communication [6]. We used graphs derived from bibliographic data for our experiments, these are described below. In most of our experiments the edge directions and weights were ignored and the largest weakly connected component was used. The Case Based Reasoning (CBR) co-citation dataset was collected from bibliography of fifteen years of CBR conferences, the aim was to examine the themes that have evolved in CBR research as revealed by the implicit and explicit relationships between the conference papers, the interested reader is referred to [4] for more details. The CBR cocitation dataset consists of a total of 672 papers from the CBR conference series, published by 828 individual authors. It is publicly available for research purposes[2]. We refer to this dataset as **CBR Cocitation (Full)**. We also performed experiments on a subset of the CBR dataset this consisted of papers only within the CBR conferences, we refer to this as **CBR Cocitation (Small)**.

[2] can be downloaded from http://mlg.ucd.ie/cbr

A Local Scheme Based on Radial Basis Functions for Natural Convection Problems

G Chandhini [a] YVSS Sanyasiraju [b] BVSSS Prasad [c]

[a] *Department of Science and Humanities, PESIT, Bangalore South Campus, India*

[b] *Department of Mathematics, IIT Madras, Chennai, India*

[c] *Department of Mechanical Engineering, IIT Madras, Chennai, India*

Abstract

A localized radial basis function (RBF) meshless method is developed for solving laminar natural convection problems in enclosures. The developed scheme is based on computing the weights for the derivatives by localizing the RBF interpolation concept. This localization approach helps to control the instability due to ill-conditioning of the RBF interpolation matrix. The governing equations are considered in the velocity-pressure formulation, where the decoupling of momentum and continuity equations are obtained using a fractional step algorithm. Numerical results are presented for the benchmark problems such as: (1) natural convection of air in a square cavity and (2) natural convection in an annulus between two isothermal concentric square ducts. Comparisons with the existing benchmark solutions show that the developed local RBF gridfree scheme is stable and produces accurate results.

Key words: natural convection, radial basis function, multiquadric, fractional-step, square enclosure

1 Introduction

Natural convective heat transfer has received a lot of attention in the literature. Applications include nuclear reactor design, cooling of electronic equipment, aircraft cabin insulation and thermal storage systems. Numerical solution of the natural convection problems is challenging mainly due to the

* Corresponding author: G Chandhini
Email address: chandhinig@pes.edu, sryedida@iitm.ac.in, prasad@iitm.ac.in (BVSSS Prasad).

nonlinearity and strong coupling that exists between the governing equations. Therefore development of faster and efficient numerical schemes is a never ending continuing process for the researchers in heat transfer.

Kansa [1] has initiated the use of RBF interpolation in the global collocation methods for solving partial differential equations. Due to the global nature of the method, the resultant linear system was full and highly ill-conditioned. Various approaches, namely, domain decomposition, preconditioning and the use of compactly supported RBFs [2,3] have been experimented to circumvent these difficulties. Recently, an RBF-based local method has been proposed by Wright and Fornberg [4]. The localization approach given in their work has been successfully extended by Chandhini and Sanyasiraju to steady convection-diffusion problems [5] and to unsteady incompressible Navier-Stokes equations [6].

In the present study, the local RBF scheme developed for unsteady incompressible viscous Navier-Stokes equations [6] has been extended to solve natural convetion problems. The velocity-pressure formulation of the governing equations has been employed to model the physical process and a fractional step algorithm [7] has been used to decouple velocity and pressure terms.

The rest of the paper is organized as follows: Section 2 gives a brief description of the local RBF based gridfree scheme. The extension of RBF scheme to natural convection equations in conjunction with fractional step algorithm have been presented in Section 3. Finally, Section 4 discusses the validation of the developed scheme using benchmark problems for natural convection in closed enclosures and compared with the existing results.

2 RBF Based Local Scheme

Let $\mathcal{L}$ be any linear differential operator and n be the total number of nodes in the discretized domain. Also assume that $\bar{x}_i$ be any point from the domain. Define $S_i = \{\bar{x}_1, \ldots, \bar{x}_{n_i}\}$ as a neighborhood of $\bar{x}_i$ consisting of n_i ($\ll n$) nodes. To approximate $\mathcal{L}u(\bar{x}_i)$ over the nodes from S_i, let it be represented as a linear combination of u at the points of S_i, given by

$$\mathcal{L}u(\bar{x}_i) \approx \sum_{j=1}^{n_i} c_j u(\bar{x}_j) \tag{1}$$

Then, the computation of the weights c_j gives the required approximation to $\mathcal{L}u(\bar{x}_i)$. To proceed further, also consider the Lagrange representation of an

interpolant $s(\bar{x})$ of $u(\bar{x})$ given by

$$s(\bar{x}) \;=\; \sum_{j=1}^{n_i} \psi_j(\bar{x}) u(\bar{x}_j) \tag{2}$$

where $\psi_j(\bar{x})$'s are the Lagrange functions which satisfy the cardinal conditions,

$$\psi_j(\bar{x}_k) \;=\; \delta_{jk}, \quad j,k = 1,2,\ldots,n_i. \tag{3}$$

Applying the operator $\mathcal{L}$ to the Lagrange representation of RBF interpolant (2) gives,

$$\mathcal{L}u(\bar{x}_i) \;\approx\; \mathcal{L}s(\bar{x}_i) \;=\; \sum_{j=1}^{n_i} \mathcal{L}\psi_j(\bar{x}_i) u(\bar{x}_j) \tag{4}$$

Comparing equations (1) & (4), c_j's can be given as,

$$c_j \;=\; \mathcal{L}\psi_j(\bar{x}_i), \;\; j = 1,\ldots,n_i \tag{5}$$

Therefore, to obtain each Lagrange function ψ_j in (3), an RBF ($\Phi(\|.\|)$) based interpolation problem is developed. That is, each ψ_j is approximated as,

$$\psi_j(\bar{x}) \approx \sum_{k=1}^{n_i} \lambda_{jk} \phi(\|\bar{x} - \bar{x}_k\|) + \sum_{k=1}^{l} \gamma_{jk} p_k(\bar{x}), \quad j = 1,2,\ldots,n_i. \tag{6}$$

where $\phi(\|.\|)$ is some radial function, $\{p_j(\bar{x})\}_{j=1}^{l}$ is a basis for Π_m^d (space of all $d-$variate polynomials with degree $\leq m$) and l is the dimension of Π_m^d. The weights λ_{jk} and γ_{jk} are obtained by imposing the cardinal conditions (3) and orthogonality conditions

$$\sum_{j=1}^{n_i} \lambda_{ij} p_k(\bar{x}_j) \;=\; 0, \quad k = 1,\ldots,l \tag{7}$$

on the interpolant (6). From the interpolation problem (6)-(7), by making use of the symmetry of the interpolation matrix and some simple properties of the determinants, a general form for $\psi_j(\bar{x})$ is obtained (refer [6]) and used in equation (5) which leads to,

$$\begin{pmatrix} \mathbf{\Xi} & \mathbf{p} \\ \mathbf{p}^T & \mathbf{0} \end{pmatrix} \begin{pmatrix} \bar{c} \\ \bar{\mu} \end{pmatrix} \;=\; \begin{pmatrix} \mathcal{L}B(\bar{x}_i) \end{pmatrix} \tag{8}$$

where $\mathbf{\Xi}_{i,j} = \phi(\|\bar{x}_i - \bar{x}_j\|), \;\; i,j = 1,\ldots,n_i$, $\mathbf{p}_{i,j} = p_j(\bar{x}_i), \;\; j = 1,\ldots,l$ & $i = 1,\ldots,n_i$, $\bar{\mu}$, a dummy vector corresponding to the vector $\bar{\gamma}$ in (6) and $B(\bar{x})$ is given by

$$B(\bar{x}) \;=\; [\phi(\|\bar{x}-\bar{x}_1\|) \;\; \phi(\|\bar{x}-\bar{x}_2\|) \;\; \ldots \;\; \phi(\|\bar{x}-\bar{x}_{n_i}\|) \;\; | \;\; p_1(\bar{x}) \; p_2(\bar{x}) \;\; \ldots \;\; p_l(\bar{x})]^T \tag{9}$$

Therefore, the weights c_j's in (1) are computed using (8) and (9). It is also clear from the development of the final linear system (8) that though it is dense, the size of (8) is only n_i, which is very much smaller than the size (n) of the global RBF collocation system. This makes the system more stable for wide range of ε. Further, only the right hand side of (8) depends on the operator $\mathcal{L}$, for which the weights are to be computed. This optimizes the computation if weights have to be computed for many operators with the same distribution of nodes, as in the case of non-linear equations.

Franke [8], has made a comprehensive comparison of about seven groups consisting of about 30 interpolation methods on six different test functions and found that performance of MultiQuadric (MQ) is the most impressive and consistently performed better in terms of accuracy. Therefore, the multiquadric function, developed by Hardy [9] and defined by

$$\Phi(\bar{x}) \;=\; \sqrt{1+\varepsilon^2\|\bar{x}\|^2} \tag{10}$$

where $\varepsilon > 0$, has been used in all the computations presented in the subsequent sections.

3 Implementation of RBF Local Scheme to Natural Convection Equations

For two-dimensional problems, the natural convection fluid flow equations in non-dimensional form can be written as

Continuity equation:
$$\frac{\partial u}{\partial x}+\frac{\partial v}{\partial z}=0 \tag{11}$$

Momentum equations:
$$\frac{\partial u}{\partial t}+u\frac{\partial u}{\partial x}+v\frac{\partial u}{\partial z}=-\frac{\partial P}{\partial x}+Pr\left[\frac{\partial^2 u}{\partial x^2}+\frac{\partial^2 u}{\partial z^2}\right] \tag{12}$$

$$\frac{\partial v}{\partial t}+u\frac{\partial v}{\partial x}+v\frac{\partial v}{\partial z}=-\frac{\partial P}{\partial z}+Pr\left[\frac{\partial^2 v}{\partial x^2}+\frac{\partial^2 v}{\partial z^2}\right]+Ra\ Pr\ T \tag{13}$$

Energy equation:
$$\frac{\partial T}{\partial t}+u\frac{\partial T}{\partial x}+v\frac{\partial T}{\partial z}=\frac{\partial^2 T}{\partial x^2}+\frac{\partial^2 T}{\partial z^2} \tag{14}$$

where (u, v), P and T are dimensionless velocity field, pressure and temperature, respectively. The necessary initial and boundary conditions depend on the chosen problem and will be discussed later. The non-dimensional parameters Raleigh number Ra and Prandtl number Pr are defined as

$$Ra=\frac{g\beta\triangle t H^3}{\nu\alpha} \quad \text{and} \quad Pr=\frac{\nu}{\alpha} \tag{15}$$

with g acceleration due to gravity, β thermal expansion coefficient, H characteristic length, ν kinematic viscosity and α thermal diffusivity of the fluid.

3.1 Fractional Step Algorithm with Local RBF Scheme

The procedure, described in this section, is based on the explicit Euler time discretization. The development of the scheme based on other temporal schemes also can be generated, however, for simplicity Euler scheme has been chosen in the presentation.

Discretization of the momentum equations (12) and (13) and energy equations by Euler method gives

$$\frac{u^{(n+1)}-u^{(n)}}{\triangle t}=\left(-u\frac{\partial u}{\partial x}-v\frac{\partial u}{\partial z}-\frac{\partial P}{\partial x}+Pr\left[\frac{\partial^2 u}{\partial x^2}+\frac{\partial^2 u}{\partial z^2}\right]\right)^{(n)} \tag{16}$$

$$\frac{v^{(n+1)}-v^{(n)}}{\triangle t}=\left(-u\frac{\partial v}{\partial x}-v\frac{\partial v}{\partial z}-\frac{\partial P}{\partial y}+Pr\left[\frac{\partial^2 v}{\partial x^2}+\frac{\partial^2 v}{\partial z^2}\right]+RaPrT\right)^{(n)} \tag{17}$$

$$\frac{T^{(n+1)}-T^{(n)}}{\triangle t}=\left(-u\frac{\partial T}{\partial x}-v\frac{\partial T}{\partial z}+\left[\frac{\partial^2 T}{\partial x^2}+\frac{\partial^2 T}{\partial z^2}\right]\right)^{(n)} \tag{18}$$

Rewriting (16) and (17) in the form

$$u^{(n+1)}=u^*+\triangle t\left(-\frac{\partial P}{\partial x}\right)^{(n)} \quad \text{and} \quad v^{(n+1)}=v^*+\triangle t\left(-\frac{\partial P}{\partial z}\right)^{(n)} \tag{19}$$

where u^* and v^* are given by

$$u^*=u^{(n)}+\triangle t\left[-\left(u\frac{\partial u}{\partial x}+v\frac{\partial u}{\partial z}\right)+Pr\left(\frac{\partial^2 u}{\partial x^2}+\frac{\partial^2 u}{\partial z^2}\right)\right]^{(n)} \tag{20}$$

$$v^*=v^{(n)}+\triangle t\left[-\left(u\frac{\partial v}{\partial x}+v\frac{\partial v}{\partial z}\right)+Pr\left(\frac{\partial^2 v}{\partial x^2}+\frac{\partial^2 v}{\partial z^2}\right)+RaPrT\right]^{(n)} \tag{21}$$

At each time step, the solution is expected to satisfy continuity equation. Hence $(u,v)^{(n+1)}$ must satisfy the continuity equation (11), which implies

$$\left(\frac{\partial u}{\partial x}+\frac{\partial v}{\partial z}\right)^{(n+1)}=0 \tag{22}$$

(or)

$$\frac{\partial}{\partial x}\left[u^* + \triangle t\left(-\frac{\partial P}{\partial x}\right)^{(n)}\right] + \frac{\partial}{\partial z}\left[v^* + \triangle t\left(-\frac{\partial P}{\partial z}\right)^{(n)}\right] = 0 \tag{23}$$

Equation (23) can be simplified to

$$\frac{\partial^2 P^{(n)}}{\partial x^2} + \frac{\partial^2 P^{(n)}}{\partial z^2} = \frac{1}{\triangle t}\left(\frac{\partial u^*}{\partial x} + \frac{\partial v^*}{\partial z}\right) \tag{24}$$

Equation (24) is a Poisson's equation with non-zero source term $\frac{\partial u^*}{\partial x} + \frac{\partial v^*}{\partial z}$ (since u^*, v^* need not satisfy the continuity equation). Numerical implementation of the procedure described from (16) to (24), based on 'local' RBF gridfree scheme, can be summarized as follows.

Assume that for each center $\bar{x}_i$, there are n_i nodes in the the supporting domain, say $\{\bar{x}_{i_1}, \bar{x}_{i_2}, \ldots, \bar{x}_{i_{n_i}}\}$. Using the 'local' RBF scheme compute the weights $c_1, c_2, \ldots, c_{n_i}$ and $c'_1, c'_2, \ldots, c'_{n_i}$ for the linear operators $\mathcal{L} = -u^{(n)}\frac{\partial}{\partial x} - v^{(n)}\frac{\partial}{\partial z}$ and $\mathcal{L}' = \frac{\partial^2}{\partial x^2} + \frac{\partial^2}{\partial z^2}$, respectively. Then the discretized form of the equations for temperature and intermediate velocities are,

$$u^* = u^{(n)} + \triangle t\left[\sum_{j=1}^{n_i}(c_j + Pr\ c'_j)u_{i_j}^{(n)}\right] \tag{25}$$

$$v^* = v^{(n)} + \triangle t\left[\sum_{j=1}^{n_i}(c_j + Pr\ c'_j)v_{i_j}^{(n)} + RaPrT^{(n)}\right] \tag{26}$$

$$T^{(n+1)} = T^{(n)} + \triangle t\left[\sum_{j=1}^{n_i}(c_j + c'_j)T_{i_j}^{(n)}\right] \tag{27}$$

Assume that the weights for $\frac{\partial}{\partial x}$ and $\frac{\partial}{\partial z}$ are $d_1, d_2, \ldots, d_{n_i}$ and $d'_1, d'_2, \ldots, d'_{n_i}$, respectively. Using which the pressure equation in (24) can be discretized as

$$\sum_{j=1}^{n_i} c'_j P_{i_j}^{(n)} = \sum_{j=1}^{n_i} d_j u^{(n)} + \sum_{j=1}^{n_i} d'_j v^{(n)} \tag{28}$$

Equation (28) is a sparse linear system which can be solved to obtain $P_{i_j}^{(n)}$ using any iterative method. In these computations the weights c_j, c'_j, d_j and d'_j's are computed only once (where $n_i << n$) and used for all time levels.

4 Results and Discussion

The developed RBF scheme, described in the previous section, is validated by solving some benchmark problems from natural convective heat transfer. The effect of Rayleigh number on the fluid flow and heat transfer rates in square enclosures have been studied and those observations are discussed in this section.

4.1 Natural convection in a square enclosure

Consider the two-dimensional flow of a Boussinesq fluid of Prandtl number 0.7 (air) in an upright square cavity described in non-dimensional terms by $0 \leq x \leq 1,\ 0 \leq z \leq 1$ with buoyancy acting vertically upwards. The boundary conditions for the velocity components are $u = v = 0$ on all the four bounding walls of the cavity due to their stationary nature. The non-dimensional temperature T is taken as -0.5 and 0.5 on the walls at $x = 0$ and 1 while the walls at $z = 0$ and 1 are treated as insulated as shown in the Figure 1. Though the developed scheme can work on any arbitrarily distributed centers, however, in the present computations for the sake of simplicity, a uniformly distributed 81×81 points have been used for all the computations. The time increment has been fixed as 0.0001. Simulations are carried out, for various values of Rayleigh numbers ranging from 10^3 to 10^6, until steady state solution is reached. The results are compared qualitatively by observing the contour patterns of stream function, vorticity and temperature (isotherms). Quantitative comparisons are carried out by looking at the values of $|\psi_{mid}|$, $|\psi_{max}|$, $u_{max}(z)$, $v_{max}(x)$ and average Nusselt number $\overline{Nu}$.

The Nusselt number (Nu) has been computed using the local heat flux which represent the heat transfer across the cavity. The local heat flux in the horizontal direction at each point in the duct is given by

$$Q(x, z) = u\ T - \frac{\partial T}{\partial x} \tag{29}$$

Then on any cross-section (parallel to z-axis), the heat flow can be given as

$$Nu_x = \int_0^1 Q(x, z)dz \tag{30}$$

Average Nusselt number ($\overline{Nu}$) is calculated by integrating Nu_x over x, that is,

$$\overline{Nu} = \int_0^1 Nu_x dx \tag{31}$$

Figures 2 - 4 illustrate the streamlines, vorticity contours and isotherms, respectively for various values of Ra. Salient features of the flow, namely absolute value of the ψ at the mid point $|\psi_{mid}|$, maximum absolute value of the stream function $|\psi_{max}|$, the maximum value of the x component of the velocity and its vertical location $u_{max}(z)$, the maximum value of the z component of the velocity and its horizontal location $v_{max}(x)$, average Nusselt number $\overline{Nu}$, heat flux at $x = 0.5$ $Nu_{1/2}$ and heat flux at $x = 0$ wall Nu_0, have been compared quantitatively with the benchmark solutions [10] for different values of Ra. The corresponding values have been reported in Table 1. It is evident from the streamline patterns reported in Figure 2 that for $Ra = 10^3$ and 10^4, maximum absolute value of the stream function occurred at the midpoint of the cavity and hence not included in the table. However, it moves away substantially from the midpoint for $Ra = 10^5$ and 10^6. It is also very clear from the reported figures that the developed scheme very accurately captures the anti symmetric nature of the flow with respect to $x = 0.5$. The average Nusselt number and the maximum value of the x component of the velocity u_{max} are compared with [10] at various Ra and reported in Figure 5. The results agree with a maximum error less than 4%.

4.2 Natural convection in an annulus between two concentric square ducts

The schematic diagram of the problem is shown in Figure 6. Annulus between the ducts is filled with a viscous, incompressible Newtonian fluid. In the present investigation, fluid with Prandtl number $Pr = 0.7$ has been considered. Two different constant temperatures at the inner and outer walls, respectively are maintained with the inner wall temperature greater than that of the outer walls.

Simulations in this problem are carried out for the dimension ratio $L = \frac{L_1}{L_2} = 1/5$, which determines the width of the annulus. The local Nusselt numbers at both inner and outer boundaries are calculated using the equations

$$Nu_{in} = \begin{cases} -\frac{\partial T}{\partial z}, & \text{if } z = (1-L)/2 \text{ or } z = (1+L)/2 \\ -\frac{\partial T}{\partial x}, & \text{if } x = (1-L)/2 \text{ or } x = (1+L)/2 \end{cases} \tag{32}$$

$$Nu_o = \begin{cases} -\frac{\partial T}{\partial z}, & \text{if } z = 0 \text{ or } z = 1 \\ -\frac{\partial T}{\partial x}, & \text{if } x = 0 \text{ or } x = 1 \end{cases} \tag{33}$$

Using the values of Nu_{in} and Nu_o, the average Nusselt numbers at inner and outer squares are computed using the formulae

$$\overline{Nu}_{in} = \frac{1}{4}\left[\int_{(1-L)/2}^{(1+L)/2} Nu_{in} dx \Big|_{z=(1-L)/2} + \int_{(1-L)/2}^{(1+L)/2} Nu_{in} dx \Big|_{z=(1+L)/2} + \int_{(1-L)/2}^{(1+L)/2} Nu_{in} dz \Big|_{x=(1-L)/2} + \int_{(1-L)/2}^{(1+L)/2} Nu_{in} dz \Big|_{x=(1+L)/2} \right] \quad (34)$$

$$\overline{Nu}_{o} = \frac{1}{4}\left[\int_{0}^{1} Nu_{o} dx \Big|_{z=0} + \int_{0}^{1} Nu_{o} dx \Big|_{z=1} + \int_{0}^{1} Nu_{o} dz \Big|_{x=0} + \int_{0}^{1} Nu_{o} dz \Big|_{x=1} \right] \quad (35)$$

Rayleigh number has been varied from 10^3 to 10^6 such that the flow undergoes a shift from conduction dominated to laminar free convective one. The computations have been carried out with a 41×41 uniform distribution, with time step 0.0001, for Ra upto 10^5. However, for $Ra = 10^6$, number of centers has been doubled and correspondingly time step has been reduced to 0.00001 to retain the stability. Figures 7 and 8 represent the streamlines and isotherms, respectively, obtained in the annular region for Ra from 10^3 to 10^6. From the isotherms for different Ra, it is seen that for small values of Ra, temperature distribution is conductive in nature, while for $Ra > 10^4$ effect of natural convection is more dominant. The average Nusselt number at the walls have been compared with [11] and reported in Figure 9.

5 Conclusions

A local radial basis function (RBF) based gridfree scheme has been developed for solving laminar natural convection problems in enclosures. The developed scheme has been discussed elaborately for the governing equations for natural convection in conjunction with fractional step algorithm. The benchmark problems like Natural convection in a square enclosure, Natural convection in an annulus between two concentric square ducts, have been solved and compared with the existing results.

References

[1] E.J. Kansa, "Multiquadrics – A scattered data approximation scheme with applications to computational fluid dynamics – II solutions to parabolic, hyperbolic and elliptic partial differential equations", Comput. Math. Appl., vol.19, pp.147–161, 1990.

[2] Z.M. Wong, Y.C. Hon, T.S. Li, S.L. Chug, E.J. Kansa, "Multizone decomposition of time dependent problems using the multiquadric scheme" , Comput. Math. Appl., vol.37 (8), pp.23–43, 1999.

[3] L. Ling, E.J. Kansa, "A least-squares preconditioner for radial basis functions collocation methods", Advances in Computational Mathematics 23 (1-2) (2005) 31–54.

[4] G.B. Wright and B. Fornberg, "Scattered node compact finite difference-type formulas generated from radial basis functions", J. Comput. Phys., vol.212, pp.99–123, 2006.

[5] G. Chandhini and Y.V.S.S. Sanyasiraju. "Local RBF-FD solutions for steady convection-diffusion problems" , Int. J. Num. Meth. Eng., vol.72 (3), pp.352–378, 2007.

[6] Y.V.S.S. Sanyasiraju and G. Chandhini. "Local Radial Basis Function Based Gridfree Scheme For Unsteady Incompressible Viscous Flows", J. Comput. Phys., vol.227, 8922–8948, 2008.

[7] J. Kim and P. Moin, "Application of a fractional-step method to incompressible Navier-Stokes equations", J. Comput. Phys., vol.59, pp.308–323, 1985.

[8] R. Franke, "Scattered data interpolation: Test of some methods", Math. Comp., vol.48, pp.181–200, 1982.

[9] R. L. Hardy, "Multiquadric equations of topography and other irregular surfaces", J. Geophys. Res., vol.76, pp.1905–1915, 1971.

[10] G. De Vahl Davis, "Natural convection of air in a square cavity: A bench mark numerical solution", Int. J. Num. Meth. Fluids, vol.3, pp.249–264, 1983.

[11] H. Asan, "Natural convection in an annulus between two isothermal concentric square ducts" Int. Comm. Heat Mass Transfer, vol.3, pp.367–376, 2000.

Table 1
Comparison of main features of the solutions of rectangular duct with [10]

Ra	Present	Davis[10]	Ra	Present	Davis[10]
$\mathbf{10^3}$ $\lvert\psi_{mid}\rvert$	1.171	1.174	$\mathbf{10^4}$ $\lvert\psi_{mid}\rvert$	5.048	5.071
$u_{max}(z)$	3.640 (0.813)	3.649 (0.813)	$u_{max}(z)$	16.098 (0.825)	16.178 (0.823)
$v_{max}(x)$	3.693 (0.175)	3.697 (0.178)	$v_{max}(x)$	19.522 (0.125)	19.617 (0.119)
$\overline{Nu}$	1.119	1.118	$\overline{Nu}$	2.243	2.243
$Nu_{1/2}$	1.117	1.118	$Nu_{1/2}$	2.228	2.243
Nu_0	1.120	1.117	Nu_0	2.260	2.238
$\mathbf{10^5}$ $\lvert\psi_{mid}\rvert$	9.081	9.111	$\mathbf{10^6}$ $\lvert\psi_{mid}\rvert$	16.251	16.320
$\lvert\psi_{max}\rvert$	9.583	9.612	$\lvert\psi_{max}\rvert$	16.799	16.750
(x,z)	(0.287,0.600)	(0.285,0.601)	(x,z)	(0.150,0.587)	(0.151,0.547)
$u_{max}(z)$	34.970 (0.862)	34.73 (0.855)	$u_{max}(z)$	70.527 (0.875)	64.630 (0.850)
$v_{max}(x)$	68.133(0.063)	68.590 (0.066)	$v_{max}(x)$	218.003(0.0375)	219.36 (0.0379)
$\overline{Nu}$	4.487	4.519	$\overline{Nu}$	8.574	8.800
$Nu_{1/2}$	4.455	4.519	$Nu_{1/2}$	8.502	8.799
Nu_0	4.551	4.509	Nu_0	8.806	8.817

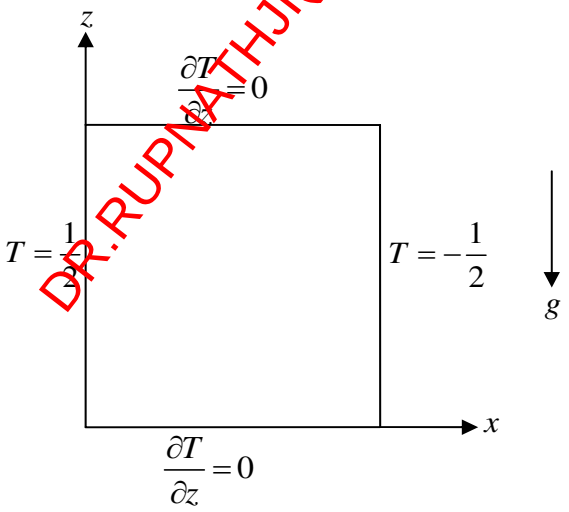

Fig. 1. Geometrical representation of the square duct

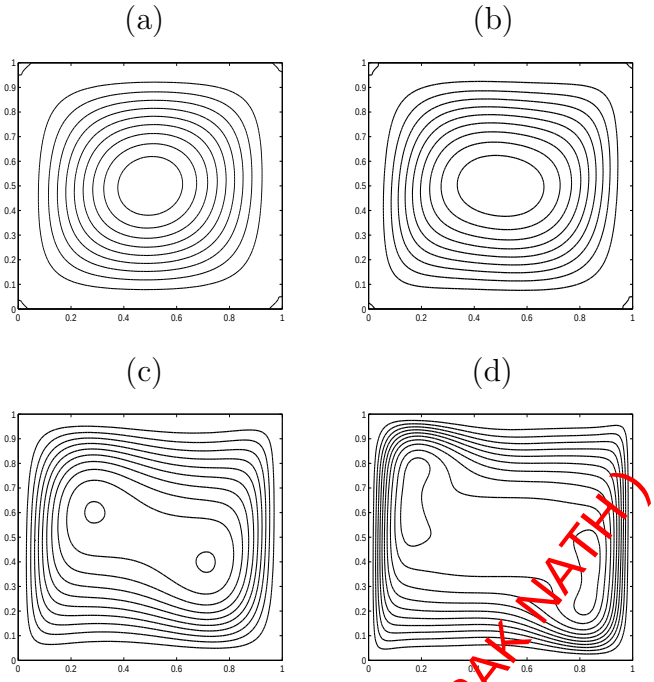

Fig. 2. Streamlines for (a) $Ra = 10^3$, (b) $Ra = 10^4$, (c) $Ra = 10^5$, (d) $Ra = 10^6$

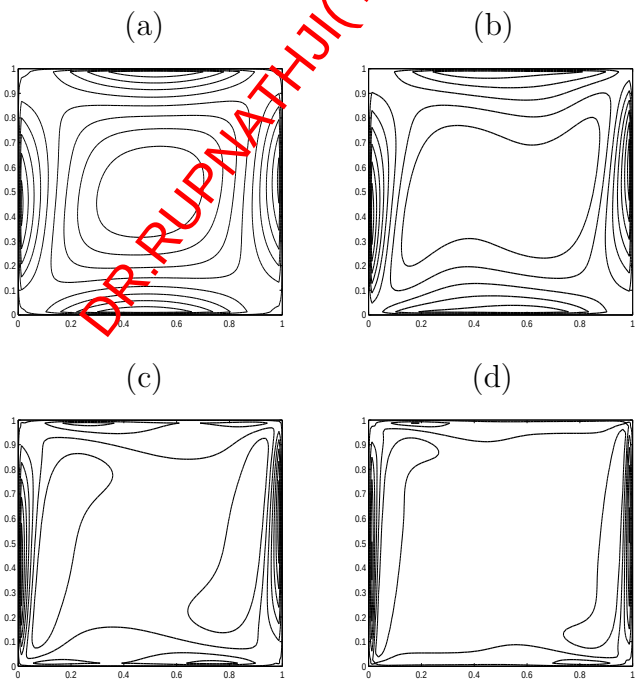

Fig. 3. Vorticity contours for (a) $Ra = 10^3$, (b) $Ra = 10^4$, (c) $Ra = 10^5$, (d) $Ra = 10^6$

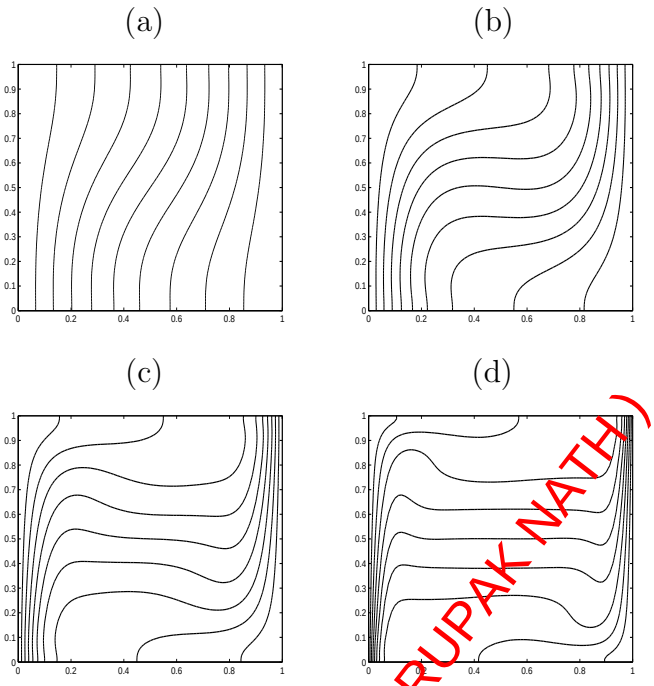

Fig. 4. Isotherms for (a) $Ra = 10^3$, (b) $Ra = 10^4$, (c) $Ra = 10^5$, (d) $Ra = 10^6$

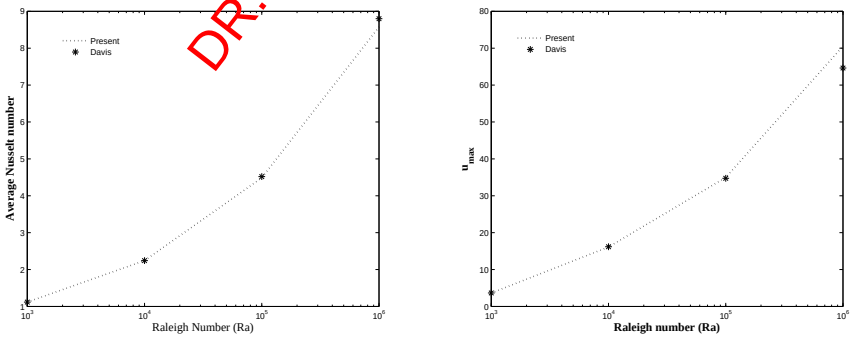

Fig. 5. Comparison of (a)Nusselt number and (b) maximum horizontal velocity (u) with Davis [10]

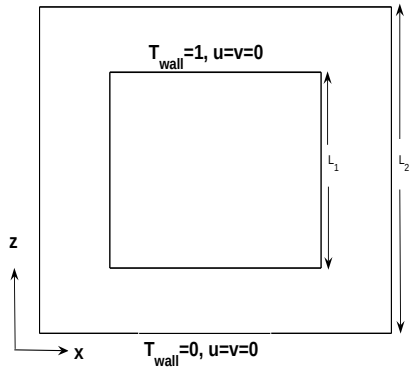

Fig. 6. Geometrical representation of the square annulus

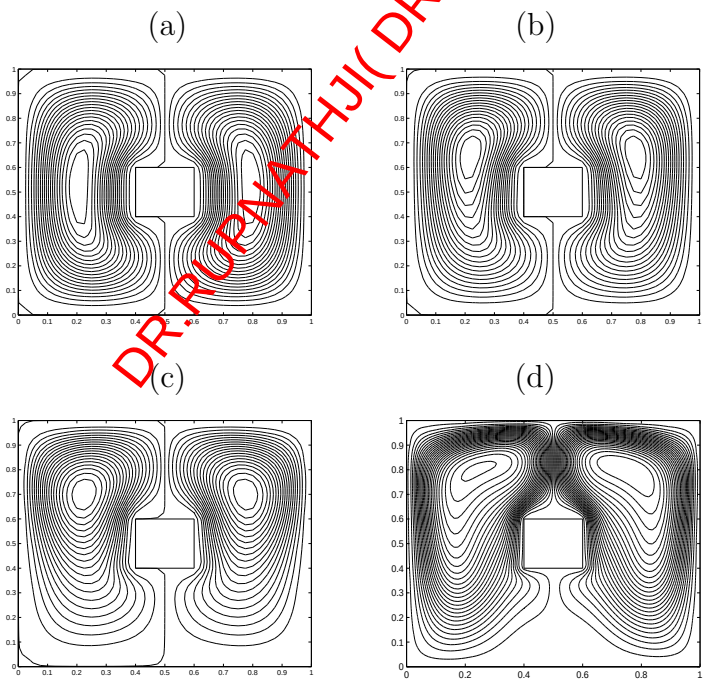

Fig. 7. Streamlines for with (a) $Ra = 10^3$, (b) $Ra = 10^4$, (c) $Ra = 10^5$, (d) $Ra = 10^6$

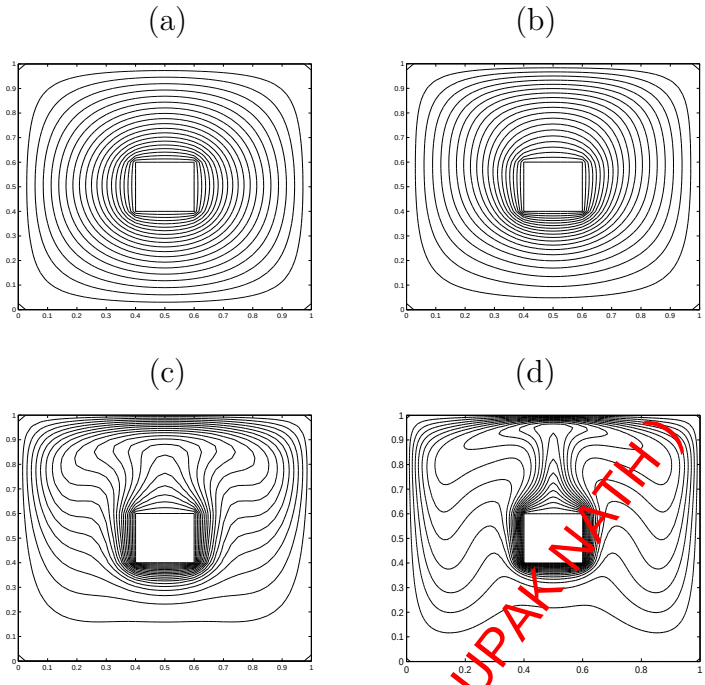

Fig. 8. Isotherms for (a) $Ra = 10^3$, (b) $Ra = 10^4$, (c) $Ra = 10^5$, (d) $Ra = 10^6$

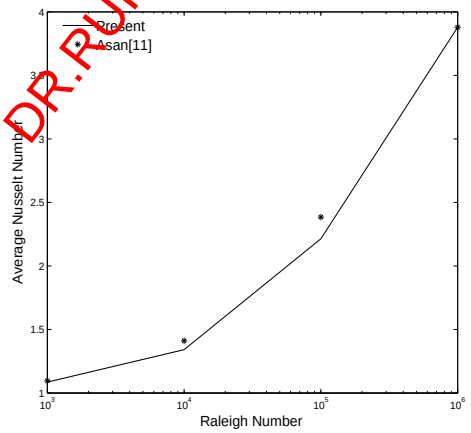

Fig. 9. Comparison of average Nusselt number for outer wall for the dimensions L = 1/5

A Novel Approach to Reduce Semantic Gap in CBIR Using Relevance Feedback: Based on Integration of MSD and MTH Descriptors

Dr.T.Venu Gopal[1]
Associate Professor
Department of CSE
JNTUH College of Engineering
Kondagattu, Karimnagar
AP, INDIA
t_vgopal@rediffmail.com

Kranthi Kumar.K[2]
Assistant Professor
Department of IT
SNIST, Yamnampet, Ghatkesar, Hyderabad
AP, INDIA
kranthikathula@gmail.com

G. Anil Kumar[3]
Associate Professor
Department of IT
Narayana Engineering College, Nellore
AP, INDIA
ganilkumar2@gmail.com

P.Prasanna Rani[4]
Assistant Professor
Department of ECE
Geetanjali College of Engineering and Technology
Cheeryala, Keesara, Hyderabad
AP,India
prasannarani.p@gmail.com

Abstract--- **Image retrieval is an important topic in the field of pattern recognition and artificial intelligence. There are three categories of image retrieval methods: text-based, content-based and semantic-based. In Content based Image Retrieval (CBIR), images are indexed by their visual content, such as color, texture, shapes. A new image feature detector and descriptor, namely the micro-structure descriptor (MSD) is discussed to describe image features via micro-structures. The micro-structure is defined based on the edge orientation similarity, and the MSD is built based on the underlying colors in microstructures with similar edge orientation. Content-based image retrieval (CBIR) is the mainstay of image retrieval systems. To be more profitable relevance feedback techniques are incorporated into CBIR such that more precise results can be obtained by taking user's feedbacks into account. The semantic gap between low-level features and high-level concepts handled by the user is one of the main problems in image retrieval. On the other hand, the relevance feedback has been used on many CBIR systems such as an effective solution to reduce the semantic gap. The gap is reduced by using the Multitexton Histogram descriptor (MTH) .**

In this paper, we propose a novel approach to reduce semantic gap in CBIR using relevance feedback based on the MSD and MTH descriptors to achieve high efficiency and effectiveness of CBIR in coping with the large-scale image data. For that reason this paper proposes a method of relevance feedback based on the Microstructure descriptor (MSD) for efficient feature extraction of an image and Multitexton Histogram descriptor to represents the effective feature representations. By using this method, high quality of image retrieval on Relevance Feedback can be achieved in a small number of feedbacks. In terms of efficiency, iteration of feedback is reduced substantially by using the navigation patterns discovered from the user query log, which reduce the computational processing time.

Keywords--- **CBIR, Relevance Feedback, Semantic Gap, Microstructure descriptor (MSD), Multitexton Histogram descriptor.**

I. INTRODUCTION

With the steady growth of computer power, rapidly declining cost of storage and ever-increasing access to the Internet, digital acquisition of information has become increasingly popular in recent years. This trend has motivated research in image databases, which were nearly ignored by traditional computer systems due to the enormous amount of data necessary to represent images and the difficulty of automatically analyzing images. Currently, storage is less of an issue since huge storage capacity is available at low cost. In many areas of commerce, government, academia, and hospitals, large collections of digital images are being created. Many of these collections are the product of digitizing existing collections of analogue photographs, diagrams, drawings, paintings, and prints. The Content Based Image Retrieval System (CBIR) is a system, which retrieves the images from an image collection where the retrieval is based on a query, which is specified by content and not by index or address. The query image is an image in which a user is interested and wants to find similar images from the image collection. The primary goal of the CBIR system is to construct meaningful descriptions of physical attributes from images to facilitate efficient and effective retrieval.

A way to retrieve this information is through the CBIR systems, although a large amount of research has been developed in this field, the performance in this system has not yet been successful due to the existence of semantic gap. Because of we use high-level concepts such as keywords or text descriptions to describe images

content and/or to measure their similarity. While that the computer-vision systems can automatically extracted low-level features from images such as color, shape, texture and spatial relationships. On the other hand there is also subjectivity of human perception of visual content of the images because of different persons or the same person under different circumstances, may perceive the same visual content differently during the information retrieval process [1], [2]. In that sense the CBIR systems try to reduce the semantic gap through relevance feedback based on the event activated human computer interaction model, which is a challenging task. The relevance feedback (RF), adapts the response of a system according to the relevant information fed back to it so that the adjusted response is a better approximation to the users information needs [3].

While there is much research effort addressing content-based image retrieval issues, the performance of content-based image retrieval methods are still limited, especially in the two aspects of retrieval accuracy and response time. The limited retrieval accuracy is because of the big gap between semantic concepts and low-level image features, which is the biggest problem in content-based image retrieval [4]. For a given query, the system first retrieves a list of ranked images according to predefined similarity metrics, which are often defined as the distance between feature vectors of images. In order to improve the retrieval accuracy of content-based image retrieval systems, research focus has been shifted from designing sophisticated low-level feature extraction algorithms to reducing the 'semantic gap' between the visual features and the richness of human semantics.

The micro-structures are defined based on an edge orientation similarity, and the MSD [5] is built based on the underlying colors in microstructures with similar edge orientation. With microstructures serving as a bridge, the MSD extracts features by simulating human early visual processing and it effectively integrates color, texture and shape and color layout information as a whole for image retrieval.

In each iteration of the RF method, the system returns some images as the result for a query image and then the user evaluates the results according to his/her demands and preferences, and tells the system which images are relevant and which are irrelevant. The MTH is a new feature representation and descriptor to retrieval contend image which integrates the advantages of co-occurrence matrix and histogram by representing the attribute of co-occurrence matrix using histogram. The generation process of the tree is based on the results of similarity between images using the MTH descriptor, the assignment of weights and the user interaction.

The rest of this paper is organized as follows. The related work is described in Section II. Section III deals with the proposed work which describes the relevance feedback approach for CBIR system, and finally section IV concludes the paper.

II. RELATED WORK

Guang-Hai Lieu .al, [5] proposed that human visual attention is enhanced through a process of competing interactions among neurons, which selects a few elements of attention and suppresses irrelevant materials. In order to extract features via simulating visual processing procedures and effectively integrate color, texture, shape features and im age color layout information as a whole for image retrieval, a novel feature detector and descriptor, namely microstructures descriptors (MSD). The MSD has advantages of both statistical and structural texture description approaches. In addition, the MSD algorithm simulates human visual perception mechanism to some extent. Ja-Hwung e, al, [6] described that conventional approaches for image retrieval are based on the computation of the similarity between the user's query and images via a query by example (QBE) system. Despite the power of the search strategies, it is very difficult to optimize the retrieval quality of CBIR within only one query process. The hidden problem is that the extracted visual features are too diverse to capture the concept of the user's query. To solve such problems, in the QBE system, the users can pick up some preferred images to refine the image explorations iteratively. The feedback procedure, called Relevance Feedback (RF), repeats until the user is satisfied with the retrieval results.

Marakakis et .al, [7]introduced new relevance feedback (RF) approach for content-based image retrieval (CBIR), which uses Gaussian mixture (GM) models as image representations. The GM of each image is obtained as an adaptation of a universal GM which models the probability distribution of the features of the image database. In each RF round, the positive and negative examples provided by the user until the current round are used to train a support vector machine (SVM) to distinguish between the relevant and irrelevant images according to the preferences of the user. Lu Hui et. A,l [8] introduces a relevance feedback system for CBIR with both short-term relevance feedback and long-term learning. In short-term relevance feedback, query reweighting algorithm, support vector machines (SVM), and genetic algorithm are adopted. In long-term learning, the expanded-judging model with index table is used for analyzing the historical log data. Through using the expanded judging model to analyze the historical feedback records, the system finds the semantic support to refine the similarity measure and improve the retrieval performance.

In [9], Mahmoudi et al. proposed the edge orientation autocorrelogram (EOAC) for shape-based image indexing and retrieval. It can be used for edge-based image indexing and retrieval without segmentation. The EOAC is invariant to translation, scaling, color, illumination, and small viewpoint variations, but it is not appropriate for texture-based images retrieval. Lowe [10] proposed a very effective algorithm, called scale-invariant feature transform (SIFT), in computer vision to detect and describe local features in images. It has been widely used in object recognition, robotic mapping and navigation, image stitching, 3D modeling, gesture

recognition, video tracking, etc. Banerjee et al. [11] proposed to use edge-based features for CBIR. The algorithm is computationally attractive as it computes different features with limited number of selected pixels.

The texton co-occurrence matrices (TCM) proposed in [12] can describe the spatial correlation of textons for image retrieval. It has the discrimination power of color, texture and shape features. Kiranyaz et al. [13] proposed a generic shape and texture descriptor over multi-scale edge field for image retrieval, which is the so called 2-D walking ant histogram (2D-WAH). As a shape descriptor, it deals directly with natural images without any segmentation or object extraction preprocessing stage. When tuned as a texture descriptor, it can achieve good retrieval accuracy especially for directional textures.

Luo et al. [14] developed a robust algorithm called color edge co-occurrence histogram (CECH), which is based on a particular type of spatial- color joint histogram. This algorithm employs perceptual color naming to handle color variation, and pre-screening to limit the search scope (i.e. size and location) of the object. A simple and interactive method which shows effectiveness in natural image retrieval using relevance feedback through the generation of trees based on the Multitexton Histogram descriptor - MTH [18]. MTH descriptor analyzes the spatial correlation between neighboring color and edge orientation based on four special texton [15] types. Because in the natural scenes the color and texture have close relationship in terms of fundamental elements and they are considered as atoms for pre-attentive human visual perception. RF confronts the subjectivity of humans in perceiving visual content and also eliminates the gap between high-level semantics and low level features, which are often used for content description and modeling [16], [17].

Guang-Hai Liu et. al, [18] presented a novel image feature representation method, called multi-texton histogram (MTH), for image retrieval. MTH integrates the advantages of co-occurrence matrix and histogram by representing the attribute of co-occurrence matrix using histogram. The MTH method is based on Julesz's textons theory, and it works directly on natural images as a shape descriptor. Meanwhile, it can be used as a color texture descriptor and leads to good performance. MTH can represent both the spatial correlation of texture orientation and texture color based on textons. MTH is well suited for large-scale image dataset retrieval.

III. PROPOSED SYSTEM

Fig.1. shows the general scheme of the proposed system using relevance feedback in CBIR. The basic idea of relevance feedback is to shift the burden of finding the right query formulation from the user to the system.

Algorithm for proposed system is as follows:

Step1: The user gives query image to the proposed system.

Step2: On given query image the system is first extract the low-level features of the image using the microstructure descriptor.

Step3: System will transform the low-level features to high-level features of the image will represents using the Multitexton histogram descriptor technique which is discussed in the following sections.

Step4: On the result of step 3, Performs the similarity measure of given image with the images in the image database.

Step5: Based on the similarity measure values the set of images will be visualized.

Step6: This set is supplied to the next phase of the proposed system i.e. relevance feedback, here the system represents the knowledge of the image. From it finds the high-level semantics of image.

Step7: On the result of step 6 is the image set displays to the user.

Step8: On this set user will give the feedback whether retrieved images are relevant or irrelevant to the query image. If images are relevant to the query image then system will be terminate and gives the final set of result to user. Else, repeat the steps from step 2 to step 7 until user satisfies with the result.

The proposed system architecture consists of two main phases

(i) Query Processing Phase.
(ii) Relevance Feedback.

(i) Query Processing Phase (QPP): In this step, the system will extract the low-level features from the image using the Micro Structured descriptor (MSD) and then on it, applies the Multilayer Neural network (MNN) to transform the high-level features of query image and features of an image will represents with Multitexton Histogram descriptor. After this, it is given to the next step to perform the similarity measure in between the queried image and images in the database, according to the similarities the system will automatically gives the ranks to the image. So that the user can easily finds the most relevant images by checking the ranks given by the system. In this step our proposed system, gives the promising results (most relevant images) to the user.

(ii) Relevance Feedback (RF): This step divided into two main parts. The first part is knowledge representation and second is high-level semantics. Using these two steps, the system will be transforms the low-level features into high-level vectors.

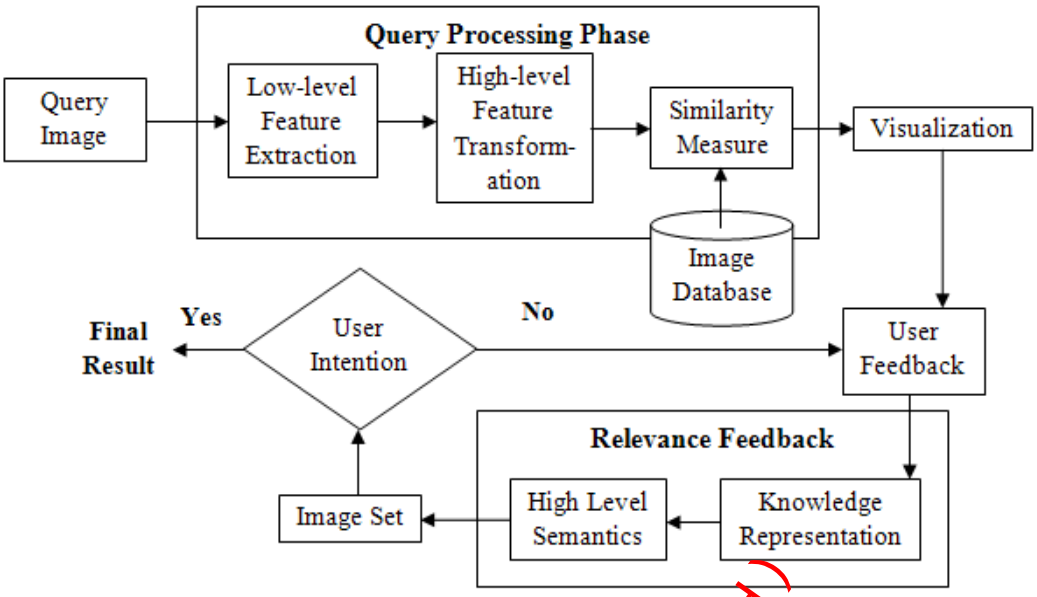

Fig.1. Proposed Relevance Feedback system architecture

The following sections describes in detail about important steps of proposed system. They are as follows:

3.1 MICROSTRUCTURE DESCRIPTOR (MSD)

The contents in digital images can vary significantly so that directly comparing them is infeasible for applications such as image retrieval. However, the local structures of images from the same class (e.g. textile, mountains, etc.) often show a certain amount of similarity. The structural approach assumes that texture is formed with simple primitives called ‘‘texels’’ (texture elements) by following some placement rules. For example, the local binary pattern [19] can be considered as a type of texture elements. A typical example of ‘‘texels’’ is Julesz’s textons theory [20] [21], but it emphasizes on regular texture images. To address this problem, the concept of micro-structures is proposed in this paper for image retrieval. In some sense, we may think that the meaningful content of natural images is composed of many universal micro-structures. Therefore, if we could extract these micro-structures and describe them effectively, they can serve as common bases for the comparison and analyses of different images. This is the essential idea of this paper, and we call the proposed technique micro-structure descriptor (MSD).

3.2 MICROSTRUCTURED IMAGE

Natural scenes are rich in color, texture and shape information and it can be considered as a mosaic of regions with different colors, textures and shapes. In general, textons are defined as a set of blobs or emergent patterns sharing a common property. Here, in fig.2. micro-structures are defined as the collection of certain underlying colors which have similar or the same edge orientation in uniform color space that combines color, texture and shape cues as a whole. In order to find the micro-structures, which have similar attributes such as edge orientation and color distribution, we partition the image into many small blocks, which can be a grid of size 2x2, 3x3, 5x5, 7x7 and so on. For the convenience of expression, the 3x3 block is used in the following development of microstructure analysis. In the 3x3 block, if one of the eight nearest neighbors has the same value as the center pixel, then it is kept unchanged; otherwise it is set to empty.

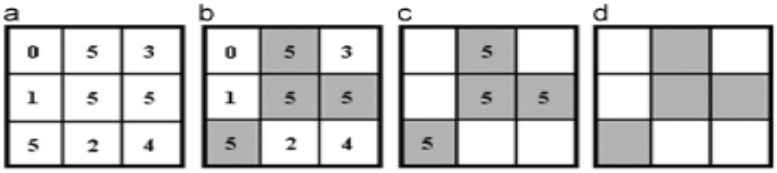

Fig.2 (a) edge orientation map; (b)–(c) show the microstructure detection process; and (d) shows the detected microstructure

In Fig.3. it shows the illustration of micro-structure map extraction process. In Fig.4. shows the steps to Microstructure image formation. In Fig.5. shows the two examples of an MSD: (a) sailing ship and (b) bus.

3.3 SIMILARITY MEASURE

Suppose there is an edge orientation map y(x, y) of size WxN. When we move the 3x3 block from left-to-right and top-to-bottom throughout the image, the detected fundamental microstructures in a neighborhood can overlap.

The following steps are used to obtain the micro structured image:

(1) Starting from the origin (0,0), we move the 3x3 block from left-to-right and top-to-bottom throughout the edge orientation image y(x,y) with a step-length of three pixels along both horizontal and vertical directions. Then, we will obtain a micro-structure map, denoted by M1(x,y), where 0<x <W-1, 0<y<N-1.

(2) Starting from the location (1,0), we move the 3x3 block from left-to-right and top-to-bottom with a step-length of three pixels along both horizontal and vertical directions. Then, a micro-structure map M2(x,y) is obtained, where 1<x<W-1, 0<y<N-1.

(3) Similarly starting from location (0, 1), we can have the third micro-structure map M3(x,y), where 0<x<W-1, 1<y<N-1.

(4) Starting from location (1, 1), we can have the fourth microstructure map M4(x,y),where 1<x<W-1, 1<y<N-1.

(5) The final micro-structure map, denoted by M(x,y), is obtained by fusing the four maps based on the following rule: $M(x,y)=Max\{M_1(x,y),M_2(x,y),M_3(x,y),M_4(x,y)\}$

3.4 MULTITEXTON HISTOGRAM DESCRIPTOR (MTH)

Liu et al. [22] [23] presents a novel image feature representation method, called multitexton histogram (MTH), for image retrieval. MTH integrates the advantages of co-occurrence matrix and histogram by representing the attribute of co-occurrence matrix using histogram. It can be considered as a generalized visual attribute descriptor but without any image segmentation or model training. a new descriptor namely multi-texton histogram - MTH, for natural image retrieval which represents the spatial correlation between neighboring color and edge orientation based on textons [15] MTH integrates the advantages of co-occurrence matrix and histogram. Natural scenes are usually rich in both color and texture, and a wide range of natural images can be considered as a mosaic of regions with different colors and textures [18]. For that reason in these natural scenes the Color and texture have close relationship in terms of fundamental elements and they are considered as atoms for pre-attentive human visual perception [26] [27].

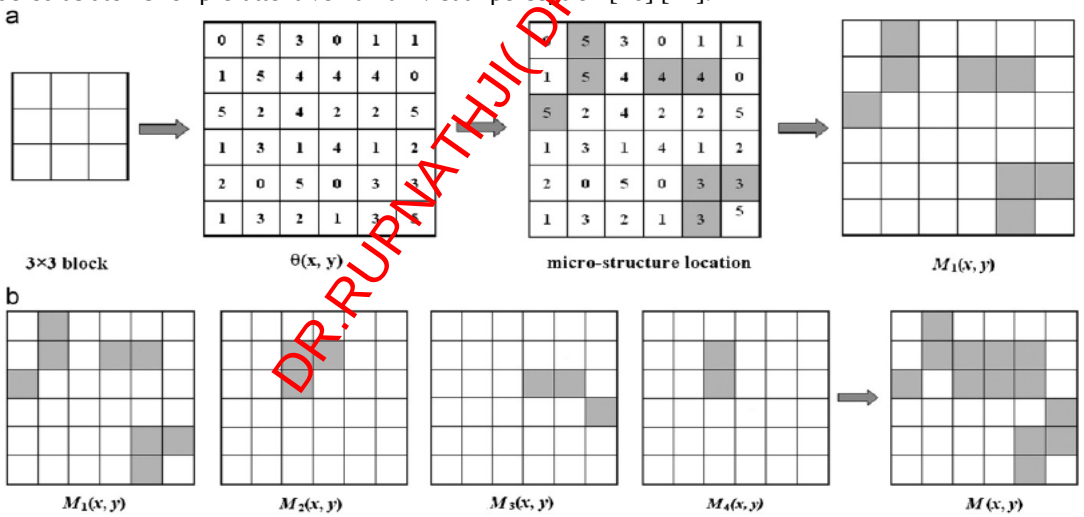

Fig.3. Illustration of microstructure map extraction process

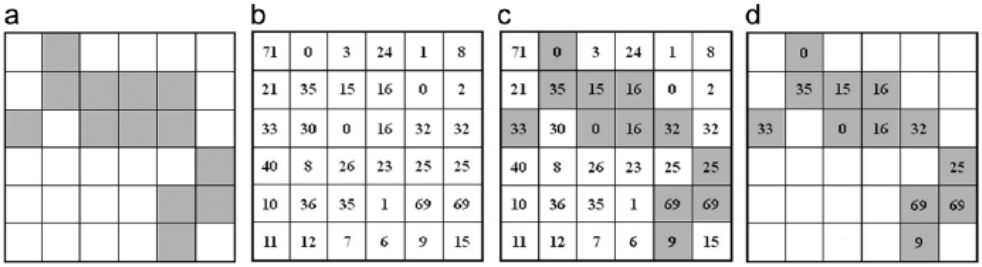

Fig.4. Micro-structure image formation.

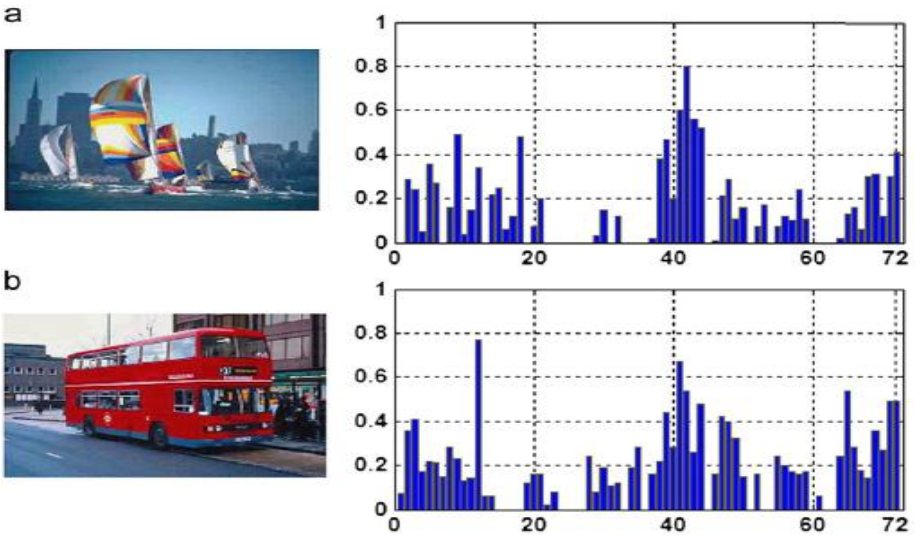

Fig.5. Two examples of an MSD: (a) sailing ship and (b) bus.

In this sense MTH represents an image by two matrices to analyze independently the spatial correlation between neighboring color and edge orientation based on four special texton types which are represented by four grids as shown in Fig. 6 (a). To each texton if the two pixels highlighted have the same value, then the grid will form a texton. Fig. 6 ((b), (c), (d) and (e)) shows the four special texton types of the proposed MTH.

The working mechanism of texton detection is illustrated in Fig.4. The 2x2 grids are moved from left-to-right and top-to-bottom throughout the edge orientation index image to detect textons with 2 pixels as the step-length. If a texton is detected, the original pixel values in the 2x2 grids are kept unchanged. Otherwise it will have zero value. Finally, the texton image is obtained, Fig. 6(e), which is used such as a mask to detect textons in the color index image.

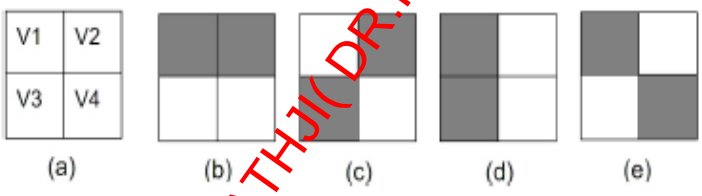

Fig.6. Four texton types (a) 2x 2 grids, (b) T1, (c) T2, (d) T3, (e) T4

In order to get the spatial correlation between neighboring color and edge orientation based on textons, MTH considers four orientations 0%, 90%, 45% and 135% with one of distance. Then to each orientation MTH forms a feature vector with 82 dimensions, where the first 64 dimensional vectors represent the spatial correlation between neighboring texture orientation by using color information and the last 18 dimensional vectors represent the spatial correlation between neighboring colors by using the texture orientation information. Finally, MTH descriptor calculates the average of the histograms to four different orientations. The Fig.5 shows an example of an original image with this MTH descriptor.

The working mechanism of texton detection is illustrated in Fig. 7. In the color index image C(x, y), we move the 2X2 block from left-to-right and top-to-bottom throughout the image to detect textons with 2pixels as the step-length. If a texton is detected, the original pixel values in the 2X2 grids are kept unchanged. Otherwise it will have zero value. Finally, we will obtain a texton image, denoted by T(x,y). The four texton types used in MTH contain richer information than those in TCM because the co-occurring probability of two same-valued pixels is bigger than that of three or four same-valued pixelsina2X2 grid. As for the texton detection procedure, MTH is also faster than TCM. In the texton detection of TCM, the 2X2 grid moves throughout the image with one pixel as the step-length, and the detected textons in a neighborhood may overlap. The final texton image needs to be fused by the overlapped components of textons, and this will increase the computational complexity. Therefore, in this paper the step- length is set to two pixels to reduce the computational cost.

3.5 RELEVANCE FEEDBACK

The Relevance Feedback is a technique that has been used quite successfully in human computer interaction; because of it allows users express better their needs in the specification of a query. In order to achieve this, after a user submits a query by a given sample, the system

will return a set of similar images to the user. The returned images may not be fully relevant to the user's targets. In order to learn the query concept of the user, relevance feedback is engaged as a query refinement technique for helping the retrieval task. The relevance feedback [24] mechanism solicits the user to mark the relevance on the retrieved images and then refines the results by learning the feedbacks from the user, at the same time that the system adjusts the low-level features of the images. The relevance feedback procedure is repeated again and again until the targets are found [28].

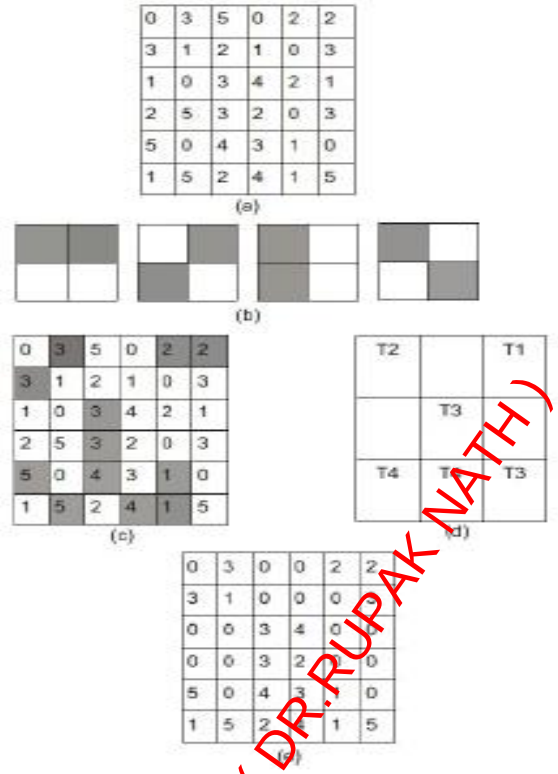

Fig.7. Mechanism of texton detection to get the texton matrix

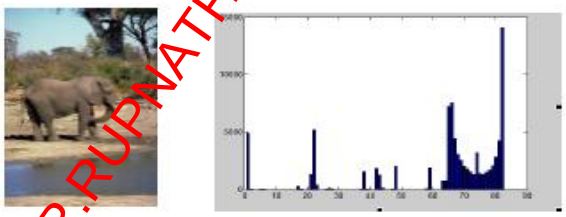

Fig.8. MTH Descriptor to the image of elephant in his habitat (a) original image (b) MTH descriptor

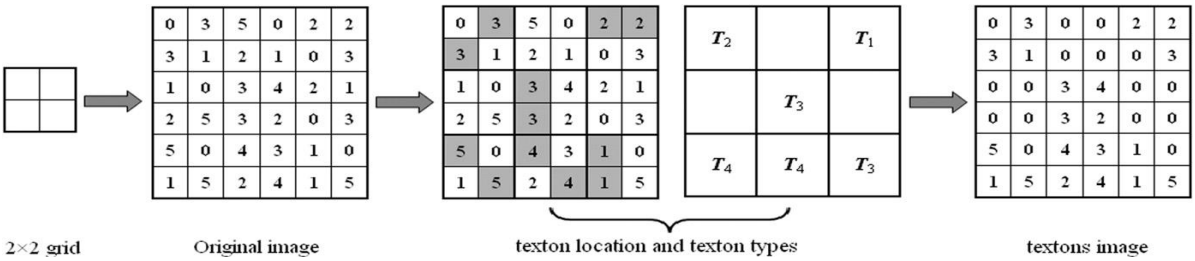

Fig.9. Illustration of the texton detection process.

A typical scenario for relevance feedback in content-based image retrieval is as follows: [29]:

i. Machine provides an initial retrieval results, through query-by-keyword, sketch, or example, etc.

ii. User provides a judgment on the currently displayed images as to whether, and to what degree, they are relevant or irrelevant to her/his request.

iii. Machine learns and tries again. Go to step 2.

This process is illustrated in Fig.10.

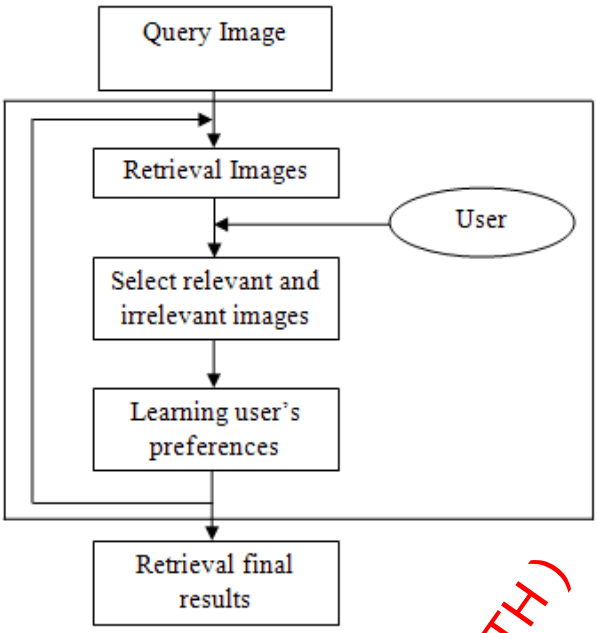

Fig.10. A typical Relevance Feedback process

Within the traditional approach to relevance feedback are for example the method of the readjustment of weights of the feature query vector [17], where the user has to precisely decompose his information need into different feature representations and precisely specify all the weights associated with them, the proposed interactive approach allows the user to submit a coarse initial query and continuously refine his information need via relevance feedback.

Another classic approach is the query point movement method (QPM), which aggregates the positive examples as a new query point at each feedback. After several a forceful changes of locations and contours, query point can be very close to a convex region of user's interest. This method is based on the Rocchio's formula which has been used in numerous applications [30].

IV. IMPLEMENTATION DETAILS

The Query Processing Phase discussed above has been implemented which involves the generation of Micro Structured Image based on the given query. The implementation includes.

4.1 COREL DATASETS

This section describes the test done based on the proposed model and optimization obtained by the model. Corel dataset has become a default standard in demonstrating the performance of CBIR systems. In this section, we evaluate the performance of our method by using Corel dataset. All Corel images contain around 500 images. Corel image database contains a large amount of images of various contents ranging from animals and outdoor sports to natural scenarios.

4.2 DISTANCE MEASURE

For each template image in the dataset, an M-dimensional feature vector T= [T1, T2, y, TM] is extracted and stored in the database. Let Q=[Q1, Q2, y, QM] be the feature vector of a query image, the L1 distance between them is simply calculated as

$$D(T, Q) = \sum_{i=1}^{M} |T_i - Q_i| \quad (1)$$

4.3 PERFORMANCE EVALUATION METRICS

The precision and recall indices are used to evaluate the performance of the proposed method. The two indices are the most commonly used measurements for evaluating image retrieval performance. Precision is the ratio of the number of retrieved similar images to the number of retrieved images, while recall is the ratio of the number of retrieved similar images to the total number of similar images. They are defined as follows:

$P = I_N/N$ (2)

$R = I_N/K$ (3)

where I_N is the number of similar images retrieved,
N is the total number of images retrieved and
K is the total number of similar images.

IV. CONCLUSION

In this paper we proposed a new method to reduce the semantic gap in CBIR using relevance feedback image retrieval based on Multitexton Histogram descriptor. To deal with the long iteration problem of CBIR, can be reduced using Micro Structure Descriptor .In summary, the main feature of Relevance Feedback is to efficiently optimize the retrieval quality of interactive CBIR. Initially, the feature representation done with Multitexton Histogram, then generated micro structured image is used in retrieving images from the database. Later, from the retrieved image set user feedback is given for a pattern-based search to match the user's intention. Finally the most relevant set of images are retrieved from the database. As a result, traditional problems such as visual diversity and exploration convergence are solved.

REFERENCES

[1] Rui, Y., Huang, T. S., and Mehrotra, S. (1998b). Relevance feedback techniques in interactive content-based image retrieval. In Storage and retrieval for image and video Databases, pages 25–36.

[2] Zhou, X. S. and Huang, T. S. (2003). Relevance feedback in image retrieval: A comprehensive review. Multimedia System, 8(6):536–544.

[3] Tai, X., Wang, L.-D., Chen, Q., Ren, F., and Kita, K.(2009). A new method of medical image retrieval based on colortexture correlogram and gti model. International Journal of Information Technology and Decision Making, pages 239–248.

[4] Y. Rui, T. Huang, M. Ortega, and S. Mehrotra, "Relevance Feedback: A Power Tool for Interactive Content-Based Image Retrieval," IEEE Trans. Circuits and Systems for Video Technology, vol. 8, no. 5, pp. 644-655, Sept. 1998.

[5] G.Liu,Z.Li, L.Zhang and Y. Xu, "Image Retrieval based on Microstructure Descriptor," Elsevier publications, Science Direct.Pattern Recognition, February 2011.

[6] Ja-Hwung Su, Wei-Jyun Huang, Philip s. Yu, Fellow," Efficient Relevance Feedbackfor Content-Based Image Retrieval by Mining Use Navigation Patterns", IEEE Transactions on Knowledge and Data Engineering, vol. 23, no. 3, march 2011.

[7] Marakakis,G. Siolas ,N. Galatsanos,A. Likas3 A. Stafylopatis ," Relevance Feedback Approach For Image Retrieval

[8] Wei Jiang, Guihua Er, Qionghai Dai, "Boost SVM active learning for content-based image retrieval," Proc. IEEE Conference Record of The Thirty-Seventh Asiloma Conference on Signals, Systems and Computers, IEEE Press, Nov. 2003.

[9] F. Mahmoudi, J. Shanbehzadeh, et al., Image retrieval based on shape similarity by edge orientation autocorrelogram, Pattern Recognition 36 (8) (2003) 1725–1736.

[10] D.G. Lowe, Distinctive image features from scale-invariant keypoints, International Journal of Computer Vision 60 (2) (2004) 91–110.

[11] M. Banerjee, M.K. Kundu, Edge based features for content based image retrieval, Pattern Recognition 36 (11) (2003) 2649–2661.

[12] G.-H. Liu, J.-Y. Yang, Image retrieval based on the texton co-occurrence matrix, Pattern Recognition 41 (12) (2008) 3521–3527.

[13] S. Kiranyaz, M. Ferreira, M. Gabbouj, A generic shape/texture descriptor over multiscale edge field: 2-D walking ant histogram, IEEE Transactions on Image processing 17 (3) (2008) 377–390.

[14] J. Luo, D. Crandall, Color object detection using spatial-color joint probability functions, IEEE Transactions on Image Processing 15 (6) (2006) 1443–1453.

[15] Julesz, B. (1981). Textons, the elements of texture perception, and their interactions. Nature, 290:91–97.

[16] Rui, Y., Huang, T., Ortega, M., and Mehrotra, S. (1998a). Relevance feedback: a power tool for interactive content-based image retrieval. IEEE Trans. Circuits and System for Video Technology, 8(5):644–655.

[17] Ajorloo, H. and Lakdashti, A. (2011). A feature relevance estimation method for content-based image retrieval. International Journal of Information Technology Decision Making (IJITDM), 10(05):933–961.

[18] G. Liu, L. Zhang,Y. Hou, Z. Li and J. Yang, "Image Retrieval Based on Multi-Texton Histogram," Elsevier publications, Science Direct.Pattern Recognition, Volume 43, Issue 7, pp. 2380-2389, July 2010.

[19] T. Ojala, M. Pietikanen, T. Maenpaa, Multi-resolution gray-scale and rotation invariant texture classification with local binary patterns, IEEE Transactions on Pattern Analysis and Machine Intelligence 24 (7) (2002) 971–987.

[20] B. Julesz, Textons, the elements of texture perception and their interactions, Nature 290 (5802) (1981) 91–97.

[21] B. Julesz, Texton gradients: the texton theory revisited, Biological Cybernetics 54 (1986) 245–251.

[22] B.Jyothi , Y.Madhavee Latha, V.S.K.Reddy." Relvance Feed Back Content Based Image Retrieval Using Multiple Features ", IEEETransactions on Knowlwdge and Data Engineering, 2010.

[23] Liu, G. H. and Yang, J. Y. (2008). Image retrieval based on the texton co-occurrence matrix. Pattern Recognition, 41:3521–3527.

[24] Chenga, P.-C., Chienb, B.-C., Kec, H.-R., and Yangd, W.-P. (2008). A two-level relevance feedback mechanism for Image retrieval. Expert Systems with Applications, 34:2193–2200.

[25] Hoi, C.-H. and Lyu., M. (2004b). A novel log-based relevance feedback technique in content-based image retrieval. pages 24–31.

[26] Jhanwar, N., Seetharaman, S. C. G., and Zavidovique, B. (2004). Content based image retrieval using motif coocurrence matrix. Image and Vision Computing, 22(14):1211–1220.

[27] Liu, G.-H., Li, Z.-Y., Zhang, L., and Xu, Y. (2011). Image retrieval based on micro-structure descriptor. Pattern Recognition, 44(9):2123–2133.

[28] Hoi, C.-H. and Lyu., M. (2004b). A novel log-based relevance feedback technique in content-based image retrieval. pages 24–31.

[29] Zhou, X. S. and Huang, T. S. (2003). Relevance feedback in image retrieval: A comprehensive review. Multimedia System, 8(6):536–544.

[30] Ye, Z., He, B., Huang, X., and Lin, H. (2010). Revisiting rocchio's relevance feedback algorithm for probabilistic models. Lecture Notes in Computer Science (including subseries Lecture Notes in Artificial Intelligence and Lecture Notes in Bioinformatics), 6458 LNCS: 151–161.

Dr.T.Venugopal Associate Professor in Computer Science and Engineering Department at JNTUH College of Engineering, Nachupally, Karimnagar, obtained his B.E(E.C.E) from Osmania University Hyderabad in 1994., M.Tech(C.S.E) from JNTU Hyderabad in 2003. Completed Ph.D in Computer Science Engineering discipline from JNTU Hyderabad in October 2009. He has 17 years of teaching experience. He has delivered several key note addresses in Conferences, Workshops and Technical Symposiums organized by various Engineering Colleges. He has organized six workshops among them two were funded by TEQIP. He has 25 publications in various national/international journals/ conferences. He has worked as NSS program officer, Coordinator in the examination branch. Presently he is Training and placement officer of the college.

Kranthi Kumar K. is currently with Sreenidhi Institute of Science and Technology, Hyderabad, India, working as Asst. Professor in the department of Information Technology. He has 10 years of experience in Teaching. Graduated in B.Tech (CSE) from JNTU Hyderabad in 2003. Masters Degree in M.Tech (CSE), from JNT University, Anantapur, AP in 2007. He is pursuing his Ph.D in Computer Science & Engineering from JNT University, Hyderabad. His areas of Interests are Image Processing, Information Retrieval Systems, Database Management Systems, Distributed Databases, Computer Networks and etc.,.

G.Anil Kumar. is currently with Narayana College of Engineering, Nellore, AP,India, working as Head & Associate Professor in the department of Information Technology. He has 11 years of experience in Teaching. Graduated in B.Tech (CSE) from JNTU Hyderabad in 2001. Masters Degree in M.Tech (CSE), from JNT University, Anantapur, AP in 2007. His areas of Interests are Image Processing, Information Retrieval Systems, Database Management Systems, Compiler Design, Computer Networks and etc.,.

P.Prasanna Rani Working as Assistant Professor in **Geethanjali College of Engineering and Technology**, Hyderabad in the Department of ECE. She completed his Graduation in B.Tech (ECE) From JNTU Hyderabad in 2006 and Post Graduation in M.Tech (Embedded Systems) From JNTU Hyderabad in the year 2009. She got More Than 4 years Teaching Experience in different Engineering Colleges. Her Areas of interest includes Image Processing, Information Retrieval Systems, Computer Networks, and Embedded Systems.

An Adaptive Calibration Circuit for Ultrasonic Flow Sensor using Optimized ANN

Santhosh K V
Dept of Electrical Engineering
National Institute of Technology, Silchar
Silchar, India
kv.santhu@gmail.com

B K Roy
Dept of Electrical Engineering
National Institute of Technology, Silchar
Silchar, India
bkr_nits@yahoo.co.in

***Abstract*— This paper proposes an adaptive calibration circuit for flow measurement technique by ultrasonic transducers using an Optimized Artificial Neural Network (OANN). The objectives of the present work are (i) to extend the linearity range of measurement to 100% of full scale input range, (ii) to make the measurement technique adaptive to variations in (a) pipe diameter, (b) liquid density, (c) liquid temperature, and (iii) to achieve objectives (i) and (ii) by using an optimized neural network. The output of ultrasonic transducer is frequency. It is converted to voltage by using a suitable data conversion unit. A suitable optimal ANN is added, in place of conventional calibration circuit, in cascade to data conversion unit. ANN is trained, and tested with data considering variations in pipe diameter, liquid density, and liquid temperature. Results show that the proposed technique has fulfilled the desired objectives.**

Keywords- Artficial Neural Network; Calibration; Linearization; Ultrasonic flow sensor; Sensor modelling

I. INTRODUCTION

Flow measurement has evolved over the years in response to measure new products, measure old products with new condition of flow, and for higher accuracy requirement as the value of fluid has gone up. Flow measurement is the quantification of fluid movement. Flow can be measured in a variety of ways, may be by contact type or non-contact type of sensor. Positive-displacement flow meters accumulate a fixed volume of fluid and then count the number of times the volume is filled to measure flow. Other flow measurement methods rely on forces produced by the flowing stream as it overcomes a known constriction, to indirectly calculate flow. Flow may be measured by measuring the velocity of fluid over a known area. Accurate flow measurement is not only an essential and vital requirement from qualitative view point but also highly essential from economic aspect. Among the non contact type of flow measurement, ultrasonic flow measurement is widely used method to measure flow, because of its advantage, like, high resolution, less interference of noise on output. However, non linear characteristics of Ultrasonic Flow Meter (UFM) have restricted its use.

Literature review suggests that several techniques are adopted to calibrate the UFM. In [1], linearization of UFM is discussed using look up table designed on a processor. In [2], calibration of UFM was carried on with the help of neural network algorithm. In [3-5], [13] calibration of flow meter using several hardware circuits is discussed. In [6], calibration of flow meter using curve fit algorithm of LabVIEW is discussed. In [7], [10] Calibration of UFM and compensation of temperature effect is discussed using neural network algorithm. Temperature compensation is also done by using a redundant sensor. In [8], calibration of flow sensor is discussed using fuzzy algorithms. In [9], calibration of flow sensor is discussed using polynomial equations. In [11], calibration of flow sensor is discussed using neural network algorithms. In [12], calibration is discussed using curve fitting polynomial equations. In [14], calibration of UFM and making it independent of pipe diameter, liquid density and temperature is discussed using Levenberg Marquardt Algorithm (LMA) of ANN is discussed. In [15], effect of liquid temperature on flow measurement is discussed. Reference [16] shows the effect of liquid density on flow measurement. In [17], effect of physical dimensions of flow meter is discussed.

To overcome the restriction faced due to nonlinear response characteristics of the ultrasonic flow meter, several techniques, as stated above, have been reported. But some of these are tedious and time consuming. Further, the process of calibration needs to be repeated or calibration circuit need to be replaced/ tuned whenever there is a change in pipe diameter or liquid density. The problem of nonlinear response characteristics of a UFM further aggravates when there is a change in liquid temperature, since the output of an UFM is also dependent on temperature.

An intelligent flow measurement technique is proposed in this paper which is made linear for the full scale input range and adaptive of variations in pipe diameter, liquid density, and liquid temperatures. The paper is an extended version of [14]. The extended version uses an optimized ANN instead of an arbitrary scheme and algorithm of ANN as considered in the original paper. The optimized ANN is achieved considering five different algorithms and schemes and comparing their MSE and Regression. The ANN model which gives least MSE and Regression close to one is considered as optimized ANN. Further, in this extended version, the proposed technique is subjected to practical data for validation.

The paper is organised as follows: after introduction in Section-I, a brief description on ultrasonic flow meter is given in Section-II. The output of the ultrasonic flow meter is frequency; a brief discussion on data conversion i.e. a

Frequency to voltage converter is discussed in Section-III. Section-IV deals with the problem statement followed by proposed solution in Section-V. Result and discussion is given in Section-VI, and the paper is ended with conclusion and future scope of work in Section-VII.

II. ULTRASONIC FLOWMETER

Ultrasonic flow meters have gained a lot of attention over the past years, primarily because of their ability to measure custody transfer of natural gas. They are replacing differential pressure and turbine flow meters in many natural gas applications. UFMs are also widely used to measure liquid flow. This is not limited to clean liquids only. UFM can accurately measure the flow of slurries and liquids with many impurities

Ultrasonic flow meters are one of the most interesting types of meters used to measure flow in pipes. The most common variety, transit time, has both a sending and a receiving transducer. Fig. 1 shows the arrangement of one such UFM. Both sending and receiving transducers are mounted on either side of the flow meter, or pipe wall. The sending transducer sends an ultrasonic signal at an angle from one side of the pipe which is received by the receiving transducer. The flow meter measures the time that the ultrasonic signal takes to travel across the pipe in forward and reverse direction. When the signal travels along the direction of the flow, it travels more quickly compare to the condition of no flow. On the other hand, when the signal travels against the direction of flow, it slows down. The difference between the "transit times" of the two signals is proportional to flow rate [18], [19].

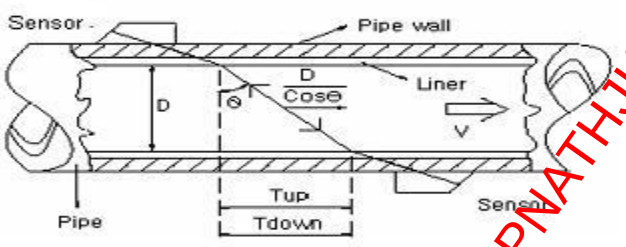

Figure 1. Arrangement of Ultrasonic flow meter

For Fig.1, we have

$$T_{up} = \frac{M*\frac{D}{\cos\theta}}{C_o + v\sin\theta} \quad (1)$$

$$T_{down} = \frac{M*\frac{D}{\cos\theta}}{C_o - v\sin\theta} \quad (2)$$

$$\Delta T = T_{up} - T_{down} \quad (3)$$

Frequency, $f_{IN} = 1/\Delta T$

where:

M – No of times ultrasonic signal travels in forward/ backward direction

C_o – Velocity of ultrasonic signal in static fluid

D – pipe diameter

v – velocity of fluid

The velocity of ultrasonic signal depends on [14], [16], [19], [20] density of liquid as,

$$C_o = \sqrt{k/\rho} \quad (4)$$

with

k – bulk modulus and

ρ – Density of liquid

Effect of temperature on density [14-16], [19-21] can be given by

$$\rho_1 = \left[\frac{\rho_0}{1+\alpha(t_1 - t_0)}\right] / \left[1 - \frac{(P_{t1} - P_{t0})}{E}\right] \quad (5)$$

where:

ρ_1 – specific density of liquid at temperature t_1

ρ_0 - specific density of liquid at temperature t_0

P_{t1} – pressure at temperature t_1

P_{t0} – pressure at temperature t_0

E– Modulus of elasticity of the liquid

α – temperature coefficient of liquid

III. DATA CONVERSION UNIT

The block diagram representation of the proposed technique is given in Fig.2.

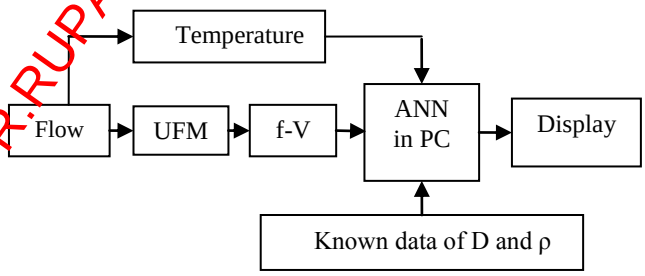

Figure 2. Block diagram of the proposed flow measurement technique

The LM2917 series are monolithic frequency to voltage (f-V) with a high gain op amp/comparator designed to operate a relay, lamp, or other load when the input frequency reaches or exceeds a selected rate [22].

The op amp/comparator is fully compatible with the sensors and has a floating transistor as its output. The collector may be taken above V_{CC} up to a maximum V_{CE} of 28V.

$$V_{OUT} = f_{IN} * R * C * V_{CC} \quad (6)$$

IV. PROBLEM STATEMENT

In this section, characteristic of ultrasonic flow meter is simulated to understand the difficulties associated with the available measurement technique. For this purpose, simulation is carried out with three different pipe diameters. These are D = 0.1 m, 0.2 m, and 0.3 m. Three different liquid densities are considered. These are ρ = 500 Kg/m^3, 1000 Kg/m^3, and 1500 Kg/m^3. Three different liquid temperatures are considered.

These are t = 25 ^{o}C, 50 ^{o}C, and 75 ^{o}C. The output frequency of UFM is calculated using eqn. 3, 4, and 5, with respect to various values of input flow considering a particular pipe diameter, liquid density, and temperature. These output frequencies are used as input of frequency to voltage converter circuit and by using eqn. 6, the output voltages are generated. The MATLAB environment is used of and the following characteristics are found.

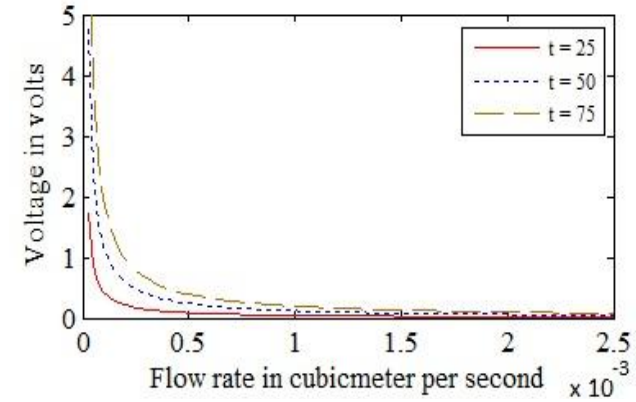

Figure 3. Output of data conversion unit for various flow rates and temperatures when liquid density is 500 Kg/m^3 and pipe diameter is 0.1 m

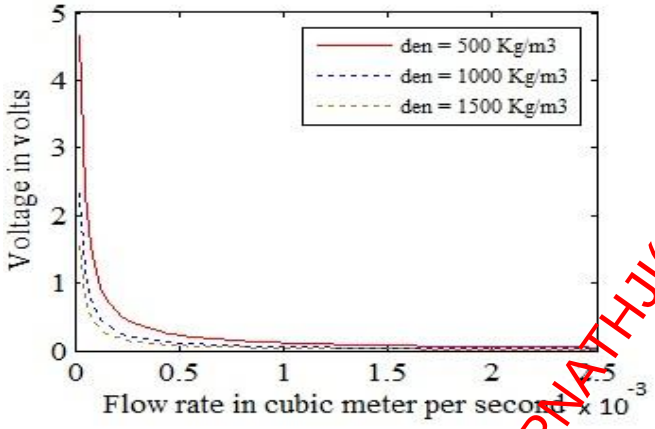

Figure 4. Output of data conversion unit for various flow rates and liquid densities when temperature is 50 ^{0}C and pipe diameter is 0.3 m

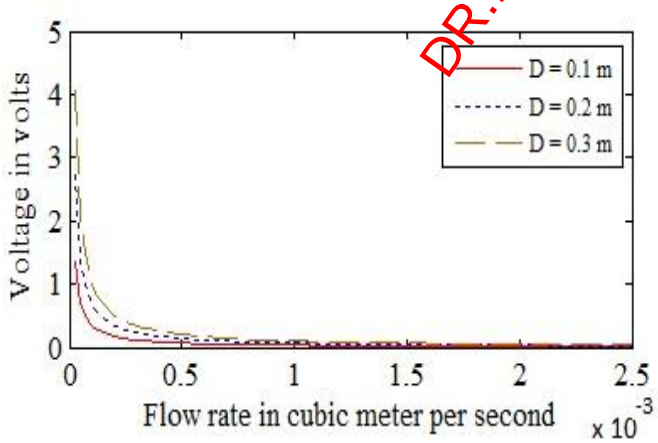

Figure 5. Output of data conversion unit for various flow rates and pipe diameters when liquid density is 1500 Kg/m^3 and temperature is 75 ^{0}C

Fig.3, Fig.4, and Fig.5 show the variation of voltages with the change in flow rate considering different values of pipe diameter, liquid density, and temperature. It has been observed from the above graphs that the output from the frequency to voltage converter circuit has a non linear relation. Datasheet of ultrasonic suggests that of 10% to 50% of full scale input range is used in practice. The output voltage varies with the change in pipe diameter, liquid density, and temperature. These are the reasons which have made the user to go for repeated calibration techniques using some circuits. These conventional calibration techniques have drawbacks that these are time consuming and need to be recalibrated whenever pipe diameter, and/or liquid density, and/or liquid temperature is changed in the system. Further the use is restricted only to a portion of full scale of input range.

To overcome these drawbacks, this paper makes an attempt to design a flow measurement technique using UFM incorporating intelligence to produce linear output for the full range of input scale and to make the system adaptive of variation in pipe diameter, liquid density, and temperature using neural network taking an optimized ANN model.

Problem statement: *given an arrangement for measurement of flow consisting of UFM in cascade with frequency to voltage converter circuit, design an intelligent non contact flow measurement technique using optimized neural network model and having the following properties:*

i. Adaptive to variations in diameter of the pipe.
ii. Adaptive to variations in liquid density.
iii. Adaptive to variations in liquid temperature.
iv. Output bears a linear relation with the input flow rate
v. Full scale input range can be measured.
vi. All using an optimized ANN.

V. PROBLEM SOLUTION

The drawbacks discussed in the earlier section are overcomed by adding an optimized ANN model in cascade with data converter unit replacing the conventional calibration circuit. This model is designed using the neural network toolbox of MATLAB.

The first step in developing a neural network is to create a database for its training, testing, and validation. The output voltage of data conversion unit for a particular flowrate, pipe diameter, liquid temperature, and liquid density is stored as a row of input data matrix. Various such combinations of input flowrate, pipe diameter, liquid temperature, liquid density, and their corresponding voltage at the output of data conversion unit are used to form the other rows of input data matrix. The output matrix is the target matrix consisting of data having a linear relation with the input flowrate and adaptive of variations in pipe diameter and/or liquid density and/or liquid temperature as shown in Fig 6.

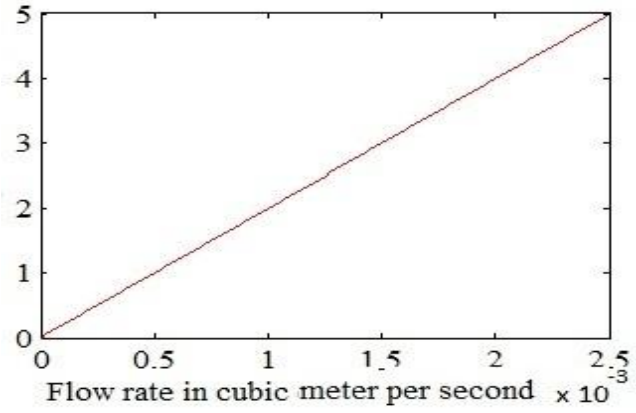

Figure 6 Target graph

The process of finding the weights to achieve the desire output is called training. The optimized ANN is found by considering different algorithms in first step and then by varying the transfer functions of neurons in second step to find an optimized structure with minimum number of hidden layers subject to MSE less than the predefined value. MSE is the average squared difference between outputs and targets. Lower values of MSE are better. Zero means no error.

Four different algorithms with back propagation scheme are used to find the optimized ANN in first step. These are Back Propagation (BP) trained by Ant Colony Optimization (ACO) [23 - 25], Back Propagation trained by Artificial Bee Colony (ABC) [26], [27], Back Propagation (BP) trained by Genetic Algorithm (GA) [28 - 30], and Back Propagation trained by Particle Swarm Optimization (PSO) [31], [32]. Training of ANN is first done assuming only one hidden layer. MSE values are noted. Hidden layer is increased to 2 and training is repeated. This process is continued up to 5 hidden layers. In all cases MSE are noted and shown in Table 1. MSE's corresponding to different algorithms and number of hidden layers is shown pictorially in Fig. 6. Table.1 and Fig.6 very clearly shows that BP trained by PSO yields most accurate results. BP trained by PSO with 1 hidden layer is considered as the most optimized ANN for desired accuracy of result. Details of the optimized neural network is given in Table-3

TABLE I. COMPARISON OF MSE FOR NEURAL NETWORK MODELS

Layers	BP_ ACO	BP_ ABC	BP_GA	BP_PSO
1	1.00E-4	8.68E-5	6.28E-5	4.11E-5
2	5.84E-7	3.47E-7	1.08E-7	9.12E-8
3	1.85E-9	9.12E-10	7.85E-10	5.89E-10
4	1.11E-11	8.61E-12	6.38E-12	4.85E-12
5	2.58E-13	1.01E-13	7.96E-14	5.47E-14
6	1.01E-15	8.67E-16	5.22E-16	3.87E-16

Different transfer functions of neuron are used in literature. In second step training, testing, and validation are repeated with ten different transfer functions of neuron on the optimized ANN. BP_PSO with one hidden layer obtained in the first step. The effect of neuron TFs in terms of MSE are noted and tabulated in Table-2. Axon TF is finally used in the optimized ANN based on the outcome of second step, as shown in the Table-2.

TABLE II. COMPARISON OF DIFFERENT NEURON TRANSFER FUNCTION

Sl.no	Transfer function	MSE
1.	Tanh	1.38E-5
2.	Sigmoid	1.02E-5
3.	Linear Tanh	8.87E-6
4.	Linear sigmoid	7.92E-6
5.	Softmax	3.08E-6
6.	Bias	2.08E-5
7.	Linear	4.11E-5
8.	Axon	2.72E-6
9.	Tansig	5.87E-6
10.	Logsig	3.99E-6

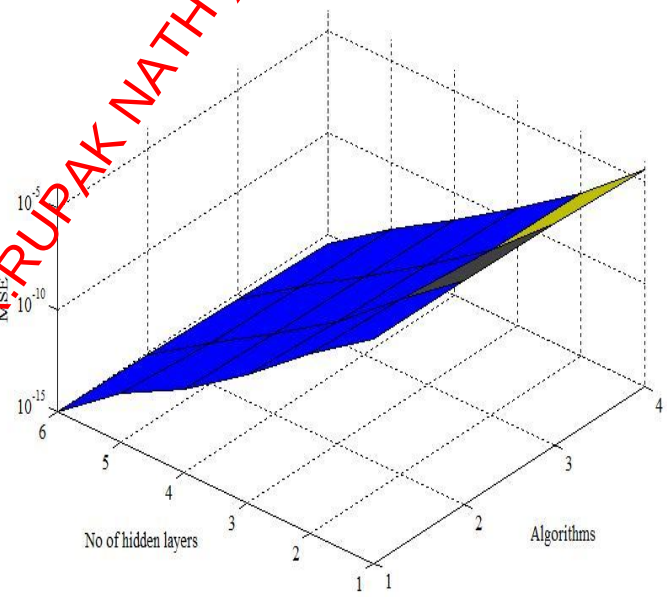

Figure 6. Mesh of variation of MSE with algorithm and hidden layer

TABLE III. DETAILS OF OPTIMIZED NEURAL NETWORK MODEL.

Optimized parameters of the neural networks model					
Database		Training base		100	
		Validation base		33	
		Test base		33	
No of neurons in		1st layer		10	
Transfer function of		1st layer		Axon	
		Output layer		linear	
Input		Flow in m^3/s	D in m	Density in Kg/m^3	Temp in ^oC
	min	0.000	0.1	500	25
	max	0.0025	0.3	1500	75

VI. RESULTS AND CONCLUSION

The proposed optimized ANN is trained, tested, and validated with the simulated data. Once the training is over, the flow measurement system is subjected to various test inputs corresponding to different flow rates at a particular pipe diameter, liquid density, and temperature, all within the specified range. For testing purposes, the range of flow is considered from 0 to 0.0025m^3/s, the range of pipe diameter is 0.1 to 0.3 m, the range of liquid density is 500 to 1500 Kg/m^3, and temperature ranges from 25^{o}C to 75^{o}C. The outputs of the proposed technique with optimized ANN are noted corresponding to various input flow rate with different values of pipe diameter, liquid density, and temperature. The results are listed in table-4.

Table IV suggests that measured flow rates are same as actual flow rate. Mean square of % error for 15 different simulated test conditions is 0.0403. It may be noted that the test conditions in Table IV are different from the training data set. Table IV show that the proposed system is made adaptive of variations in pipe diameter, liquid density, and liquid temperature, and thus repeated calibration can be avoided.

Available reported works have discussed different techniques for calibration of flow measurement, but these are not adaptive of variations in pipe diameter, liquid densities, and temperatures. Hence, repeated calibration is required for any change of these parameters. Some time the calibration circuit may itself be replaced which is a time consuming and tedious procedure. Further, most of the reported works have not utilized the full scale of measurement. In comparison to these, the proposed flow measurement technique achieves linear input output characteristics for full scale input range and makes the output adaptive of variations in pipe diameter, liquid density, and temperature. All these have been achieved by using an optimized ANN model. Four different models are considered for this purpose. BP trained by PSO algorithm with neuron transfer function as axon, is found to have achieved the desired MSE with only one hidden layers. This is in contrast to an arbitrary ANN used in most of the earlier reported works.

REFERENCES

[1] E Aziz, Z Kanev, M Barboucha, R Maimouni, M Staroswiecki, "An Ultrasonic Flowmeter Designed According to Smart Sensors Concept", *Proc. Electrotechnical Conference*, Italy, May, 1996.

[2] T T Yeh, P I Espina, Stephen A Osella, "An Intelligent Ultrasonic Flow Measurement and Flow Calibration Facility", *Proc. IEEE Instrumentation and Measurement Technology Conference*, Budapest, Hungary, May, 2001.

[3] O Keitmann-Curdes, B Funck, "A New Calibration Method for Ultrasonic Clamp-On Transducers", *Proc. IEEE Ultrasonic Symposium*, Beijing, China, November, 2008.

[4] Satish Chandra Bera, Badal Chakraborty, "A Novel Technique of Flow Measurement for a Conducting Liquid", *IEEE Transactions on Instrumentation and Measurement*, vol. 58, no.8, August 2009.

[5] Ziquang Dong, Qing-An Huang, Ming Qin, Guangping Shen, "An Intelligent Flow Sensor System with Zero Drift Self Calibration Function", *Proc. 3rd International Conference on Nano/Molecular Medicine and Engineering*, Taipan, Taiwan, October 2009

[6] Huang Ming-jian, Tang Zhen-juan, Zhu Jiang, Sun Shi-xiang, Xu Cui-cui, "Calibration System of Large Diameter Flowmeter Base on LabVIEW", *Proc. International workshop on Intelligent System and Applications*, Wuhan, China, 2009.

[7] G Yan-xia Wang, Zhi-hao Li, "Temperature Compensation of Ultrasonic Flow Measurement Based on the Neural Network", *Proc. International Conference on Artificial Intelligence and Computational Intelligence*, Shanghai, China, November, 2009.

[8] Elangeshwaran Pathmanthan, Rosdiazli Ibrahim, "Development and Implementation of Fuzzy Logic Controller for Flow Control Application", *Proc. International Conference on Intelligent and Advanced Systems*, Manali, Philiphines, June, 2010.

[9] Dailiang Xie, Ning Cheng, Shan Tao, Ting Fang, Guowei Liang, "The Study on Measurement Characteristics of Fluidic Flowmeters Sensors with CFD", *Proc. World Congress on Intelligent Control and Automation*, Jinan, China, July, 2010.

[10] Yan-xia Wang, Zhi-hao Li, Ting-hu Zhang, "Research of Ultrasonic Flow Measurement and Temperature Compensation System based on Neural Network, *Proc. International Conference on Aritifical Intelligence and Computational Intelligence*, Sanya, China, October, 2010.

[11] Meng Hua, Wang Hui, Li Mingwei, "High-precision Flow Measurement for An Ultrasonic Transit Time Flowmeter", *Proc. International Conference on Intelligent System Design and Engineering Application*, Hunan, China, October, 2010.

[12] Han Xiao, Jianzhong Zhou, Zhiwei Huang, Mengqi Yang, "A Method of Multi-Channel Ultrasonic Flow Rate Measurement Based on Piecewise Curve Fitting", *Proc. 2nd International Conference on Control, Instrumentation and Automation*, Shirz, Iran, December, 2011.

[13] Yi Liu, Lijun Sun, Lei Qi, Shengjie Li, Yanxing Wei, "Development of a Gas Flow and Velocity Calibration Facility", *Proc. International Conference on Consumer, Electronics, Communications and Networks*, Three Gorges, China, April, 2012.

[14] Santhosh K V, B K Roy, "An Intelligent Flow Measuring Scheme Using Ultrasonic Flow Meters, *31st IASTED International Conference on Modeling, Identification and Control*, Phuket, Thailand, 4-6 April, 2012.

[15] Taleb Moazzeni, Jian Ma, Yintao Jiang, Ning Li, "Flow Rate Measurement in a High- Temperature Radioactive, and Corrosive Environment", *IEEE Transactions on Instrumentation and Measurement*, vol. 60, no. 6, pp. 2062-2069, June, 2011.

[16] Kaurosh Kolahi, Thorsten Shroder, Helmut Rock, "Model-Based Density Measurement With Coriolis Flowmeter", *IEEE Transactions on Instrumentation and Measurement*, vol. 55, no.4, pp. 1258-1262, August, 2006.

[17] Zhang Ha, Yu Gu, "A New Design for Ultrasonic Gas Flowmeter", *Proc. World Congress on Intelligent Control and Automation*, Dalian, China, June, 2006.

[18] DVS Murty, *Transducer and Instrumentation*, Prentice Hall India, 2003.

[19] Bela G Liptak, Instrument Engineers' Handbook: Process Measurement and Analysis, 4th Edition, CRC Press, June, 2003.

[20] Rodrigo J. Plaza, Sink or Swim: The Effects of Temperature on Liquid Density and Buoyancy, California state science fair, 2006.

[21] Density of Fluids - Changing Pressure and Temperature, The Engineering toolbox, 2004.

[22] LM 2917 Data sheet, National Semiconductor Corporation, 2006.

[23] Jeng-Bin Li, Yun-Kung Chung, "A Novel Back propagation Neural Network Training Algorithm Designed by an Ant Colony Optimization", IEEE/PES Transmission and Distribution Conference & Exhibition: Asia and Pacific Dalian, China, 2005.

[24] L. Bianchi, L.M. Gambardella, M.Dorigo, "An ant colony optimization approach to the probabilistic travelling salesman problem", Proc. of PPSN-VII, Seventh Inter17 national Conference on Parallel Problem Solving from Nature, Springer Verlag, Berlin, Germany, 2002.

[25] T Poggio, F Girosi, "Networks for approximation and learning", Proc. IEEE 78(9), pp. 1484-1487, 1990.

[26] D. Karaboga, "An idea based on honey bee swarm for numerical optimization", Technical report-tr06, Erciyes university, engineering faculty, computer engineering department, 2005.

[27] R. Venkata Rao, "Multi-objective optimization of multi-pass milling process parameters using artificial bee colony algorithm. Artificial Intelligence in Manufacturing", Nova Science Publishers, USA, 2004.

[28] Davis, L., Ed. "Handbook of Genetic Algorithms",Van Nostrand Reinhold, New York, NY, 1991.

[29] S Rajasekaran, G A Vijayalakshmi Pai, "Neural Networks, Fuzzy Logic and Genetic Algorithms", PHI Learning Pvt. Ltd, August, 2004.

[30] Eberhart, R. C, R. W Dobbins, "Neural Network PC Tools: A Practical Guide", Academic Press, San Diego, CA , 1990.

[31] Millonas, M. M. Swarms, "Phase transitions, and collective intelligence. In C. G. Langton, Ed., Artijicial Life III". Addison Wesley, Reading, MA, 1994.

[32] James Kennedy, Rusell Eberhart, "Particle Swarm Optimization", Proc. Conf. Neural Networks, vol. 4, 1995.

TABLE V. SHOWS THE RESULTS OF PROPOSED TECHNIQUE FOR VARIOUS INPUT CONDITIONS

Actual flow in m^3/s	Pipe dia in m	Liquid density in Kg/m^3	Temp in ^oC	Data conver o/p in V	ANN o/p in V	Measured flow in m^3/s	Error in %
0.0005	0.15	500	75	3.65	0.9985	0.0004992	0.160
0.0005	0.20	600	70	3.97	1.0025	0.0005012	-0.240
0.0005	0.25	700	65	4.13	0.9992	0.0004986	0.280
0.0010	0.30	800	60	1.09	1.9987	0.0009996	0.040
0.0010	0.10	900	55	1.18	2.0062	0.0010035	-0.350
0.0010	0.125	1000	50	1.43	2.0084	0.0010012	-0.120
0.0015	0.175	1100	45	0.41	2.9967	0.0014991	0.060
0.0015	0.225	1200	40	0.55	2.9986	0.0014988	0.080
0.0015	0.275	1300	35	0.63	3.0081	0.0015022	-0.147
0.0020	0.325	1400	30	0.50	4.0068	0.0020018	-0.090
0.0020	0.075	1500	25	0.88	4.0031	0.0020029	-0.145
0.0020	0.050	550	20	0.51	3.9991	0.0019988	0.060
0.0025	0.20	650	70	0.61	4.9993	0.0024998	0.008
0.0025	0.10	750	33	0.80	5.0029	0.0025003	-0.012
0.0025	0.30	850	48	0.69	5.0051	0.0025008	-0.032

Measuring Effectiveness of Information Retrieval on the basis of User Preferences

Rekha Jain[1] Rupal Bhargava[2] G.N Purohit[3]
Banasthali Vidyapith, Jaipur
C-62, Sarojini marg, C-scheme, Jaipur-302001
Phone no: 0141-5118721, Fax no: 0141-2375322
rekha_leo2003@yahoo.com[1]
bhargava.rupal@gmail.com[2]
gn_purohitjaipur@yahoo.co.in[3]

Abstract:
With the tremendous growth of the web it becomes hard to cope up with the increasing demand of information on web, up to the level of user's expectation. Users always want most appropriate results. For this purpose Search Engines use Page Ranking Algorithms. Ranking Algorithms line up the results according to the user priority. This paper deals with "Page Rank Algorithm" which is used in the most famous search engine "Google". Our proposed algorithm acts as a layer onto the search engine which in turn gives better results to the user by disambiguating the query. To prove that our algorithm improves the results we have used Precision and Recall measures and compared both the algorithms on these measures.

Paper description:
A new Ranking algorithm is proposed in this paper which is a way better than the majorly used Page Rank algorithm.

Keywords:
Information retrieval, Page Rank Algorithm, Precision, Ranking Algorithm, Recall

I. INTRODUCTION

"World Wide Web" these words are embedded into our lives to such an extent that we cannot even think of separating them from ourselves. And if we do so it will affect our lives largely. Today, with such an increasing demand of information and network building, search engines have served a great purpose. With them information access has become a work of seconds. But the question arises whether these Search Engines are providing results according to user demand / perspective or they are giving just an another generalized results? To some extend we can say they are just giving generalized result on the user queries. For e.g. when a user enters "Cricket" Search engine will result the web pages related to sports as well as the insect. But it doesn't identify the need of the user i.e. if user wants to search for cricket (insect) or cricket (sports). In this paper we are going to propose a framework which resolves such type of ambiguities.

II. LITERATURE REVIEW

Information retrieval is the activity of obtaining information resources relevant to an information need from a collection of information resources. Searches can be based on metadata or on full-text indexing. Today Search Engines are highly used for the purpose of Information Retrieval and with such a high demand it becomes essential to refine the results and present user with the most appropriate top ranked results. Web Mining is the field which deals with such concepts. R. Cooley, B. Mobasher and J. Srivastava [9] proposed the definition of Web Mining, its taxonomy. They also proposed architecture of Web Usage Mining. In July 2000, R. Kosala, H. Blockeel [10] pointed some confusion regarding the usage of the term Web Mining and its categories. Besides this they explored the connection between the Web mining categories and their related agent paradigm. David Hawkin [2] gave the descriptive view of Web Search engines and its components. Eric J. Glover, Steve Lawrence, Michael D. Gordon, William P. Birmingham, C. Lee Giles [3] proposed a search engine which not only produces the relevant results but also allow users to provide preferences in the form of an information need category. With the help of such information search engine provides more valuable results than by considering only the query.

To provide users with the results ranking mechanism is used. Till now many Ranking Algorithms have been proposed. S. Brin and L. Page [7][11] proposed the ranking algorithm "Page Rank Algorithm" which is used in most popular search engine Google which prioritize web pages according to its inbound links. They used the concept of citation analysis such that a link coming from an important page was given high weight whereas page which was not so important was given a low weight. Also they gave a formula to calculate the Page Rank of pages in an iterative manner.

J.Kleinberg [5][6] gave us algorithm "Hyperlink Induced Topic Search" (HITS). He recognized two different forms of web pages called hubs and authorities. Authorities are pages having important contents whereas Hubs are pages that act as resource lists guiding users to authorities. Thus a good hub page for a subject points to many authorities pages on that content, a good authority page is pointed by any good hub pages on the same subject. Kleinberg said that a page may be a good hub and good authority at the same time and this circular relationship lead to the definition of an iterative algorithm HITS. This algorithm was used in search engine "CLEVER" but was not successful because of topic drift and efficiency problems. Also this algorithm worked on both Web Structure Mining as well as Web Content Mining.

Wenpu Xing and Ali Ghorbani [12] proposed "Weighted Page Rank" (WPR) algorithm which is an extension of Page Rank algorithm. This algorithm assigns a larger rank values to the more important pages rather than dividing the rank value of a page evenly among its outgoing linked pages. This algorithm is based on Web Structure Mining.

III. WEB MINING

Web Mining is a branch of Data Mining that automates the extraction of information from Web documents and services. Web Mining can be categorized into three as shown in figure 1:

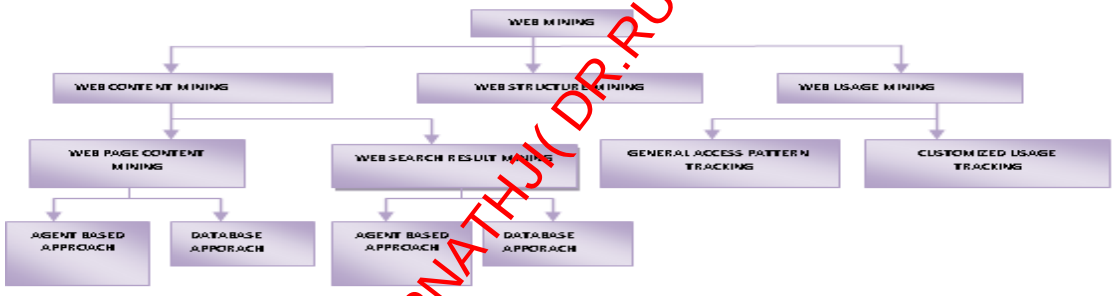

Figure 1. Categories of Web Mining

Web Content Mining helps exploring useful and relevant information from the content of web. Web Structure Mining helps find structure that exists between different web pages. Web Usage Mining considers the usage pattern of the user to find out the relevant data.

IV. RANKING ALGORITHMS

Ranking Algorithms plays an important role in ordering the results of search engine according to the user priority. Different ranking algorithms work on different perspective. Some ranking algorithms work on link structure, some on content analysis and others on the usage pattern of user. With the differing nature of ranking algorithm, many ranking algorithms have been developed. To understand the basic nature and use following algorithms are discussed in the next section.

A. PAGE RANK ALGORITHM

Page Rank Algorithm was developed by Brin and Page [7][11] during their thesis at Stanford University. This algorithm is a graph based algorithm which uses link structure of web pages and considers back links for the calculation of ranks of web pages.

For this purpose Brin and Page [7][11] proposed a formula to calculate Page rank of a Page 'A' where T_1, $T_2 \ldots T_n$ are pages pointing to it. Formula is as follows:

$$PR(A) = (1-d) + d\left(\frac{PR(T_1)}{C(T_1)} + \frac{PR(T_2)}{C(T_2)} + \cdots + \frac{PR(T_n)}{C(T_n)}\right) \quad \ldots\ldots\ldots\ldots\ldots (1)$$

Where,

d, damping factor (whose value is generally 0.85).It is used to stop other pages having too much influence)

C (T_i), number of links going out of T_i

PR (T_i), Page rank of Page T_i

Sum of page rank of all web pages corresponds to 1. It uses an iterative approach to calculate actual page rank of web pages initiating with page rank 1 for all web pages.

B. WEIGHTED PAGE RANK ALGORITHM

Weighted Page Rank algorithm was proposed by Wenpu Xing and Ali Ghorbani. [12] It is an extended version of Page Rank algorithm which decides the rank of pages on basis of both in links and out links of the pages. It doesn't divide the rank equally among all the outgoing links; instead it works on the basis of importance of Web pages. Wenpu Xing and Ali Ghorbani [12] gave the modified formula as:

$$PR(u) = (1-d) + d \sum PR(v) W^{in}_{(v,u)} W^{out}_{(v,u)} \quad \text{..... (2)}$$

Where,

d, damping factor (whose value is generally 0.85).It is used to stop other pages having too much influence)

PR (T_i), Page rank of Page T_i

$$W^{out}_{(v,u)} = \frac{O_u}{\sum_{p \epsilon R(v)} O_p} \quad \text{..... (3)}$$

$$W^{in}_{(v,u)} = \frac{I_u}{\sum_{p \epsilon R(v)} I_p} \quad \text{..... (4)}$$

I_u *and* I_p represent the number of in links of page u and page p, respectively.

O_u *and* O_p represent number of out links of page u and page p, respectively

R (v) denotes the reference page list of page v.

C. HYPERTEXT INDUCED TOPIC SELECTION (HITS)

Kleinberg [5][6] categorized web pages into two forms, hubs and authorities. Where authorities were the pages that contain important content or information specific to the query and hubs were the pages that contain links to authorities. Hence for a hub to be a good hub it should point to many authoritive pages on the specific content whereas a authority to be a good authority it should be pointed by many good hubs. Kleinberg said that pages may be a good authority and hub at the same time. This iterative relation formed the basis for HITS. In HITS there are two major steps:

- Sampling: A set of relevant pages to the query are collected from the complete set of web pages.
- Iterative Step: Finds hubs and authorities using formulas given below:

$$H_p = \sum_{q \in I(p)} A_q \quad \text{..... (5)}$$

$$A_p = \sum_{q \in B(p)} H_q \quad \text{..... (6)}$$

Where

H_p is hub weight of p

A_p is authority weight of p

$I_{(p)}$ is set of reference pages

$B_{(p)}$ is set of reference pages

V. PROPOSED WORK

Our proposed algorithm acts as a layer to the Page Rank Algorithm. It resolves the ambiguity of the query and rearranges the results as per the user requirements. For e.g. If user enters the query "Cricket" it may refer to Cricket as a sport or as a insect. Our algorithm resolves the ambiguity of these words and produces results according to the user preference. The framework of the proposed algorithm is given in fig 2.

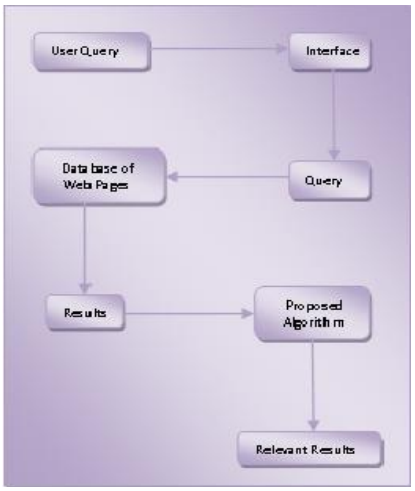

Fig 2. Framework of Proposed Algorithm

VI. RESULTS

When the user enters a the word cricket, to be searched, Google results returns the pages both for cricket(sport) and cricket(insect) but the cricket(sports) pages are on the top priority and user need to traverse result pages for finding the cricket(insects). The results of Google are shown in fig 3. The results produced by our algorithm were much efficient as when we applied the measures on both the algorithms. We have compared both the algorithms (Page Rank and newly developed algorithm) on the basis of Precision and Recall measures. Precision is a measure of the ability of a system to present only relevant items. Recall is a measure of the ability of a system to present all relevant items.

Fig3.Google Results

PRECISION		
	GOOGLE	PROPOSED ALGORITHM
Top 1	0	1
Top 2	0	1
Top 3	0	1
Top 4	0	0.75
Top 5	0	0.6
Top 6	0	0.5
Top 7	0.1429	0.4286
Top 8	0.125	0.375
Top 9	0.1111	0.4444
Top 10	0.1	0.4
Top 11	0.0909	0.3636
Top 12	0.0833	0.3333
Top 13	0.0769	0.3077
Top 14	0.0714	0.2857
Top 15	0.0667	0.2667
Top 16	0.0625	0.25
Top 17	0.1176	0.2941
Top 18	0.1111	0.2778
Top 19	0.1053	0.2632
Top 20	0.1	0.25

Table1. Comparison for Precision

RECALL		
	GOOGLE	PROPOSED ALGORITHM
Top 1	0	0.0278
Top 2	0	0.0556
Top 3	0	0.0833
Top 4	0	0.0833
Top 5	0	0.0833
Top 6	0	0.0833
Top 7	0.0278	0.0833
Top 8	0.0278	0.0833
Top 9	0.0278	0.1111
Top 10	0.0278	0.1111
Top 11	0.0278	0.1111
Top 12	0.0278	0.1111
Top 13	0.0278	0.1111
Top 14	0.0278	0.1111
Top 15	0.0278	0.1111
Top 16	0.0278	0.1111
Top 17	0.0556	0.1389
Top 18	0.0556	0.1389
Top 19	0.0556	0.1389
Top 20	0.0556	0.1389

Table2. Comparison for Recall

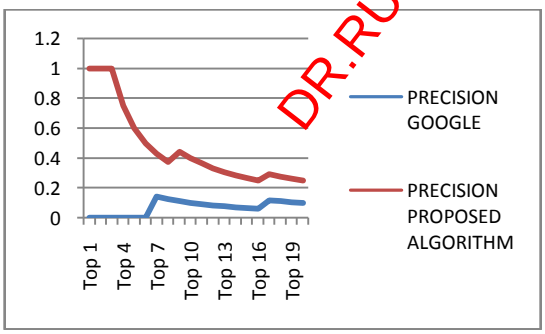

Fig 4. Comparative graph for Precision

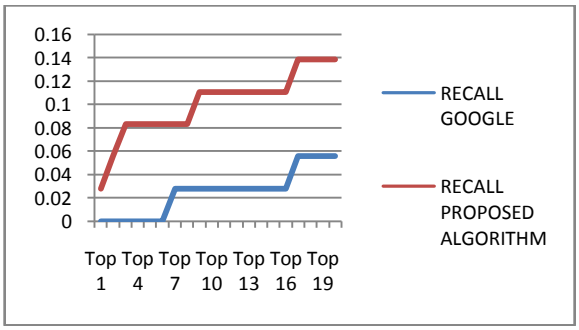

Fig 5. Comparative graph for Recall

VII. CONCLUSION

Different ranking mechanisms are used for different purpose out of which Page Ranking algorithm is most widely used. In this paper we have proposed an extension of Page Rank algorithm which helps to resolve ambiguities of search queries and provide appropriate results to users. Also we have compared both the algorithms (Page Rank algorithm and the proposed algorithm) on the basis of Precision and Recall measures.

REFERENCES

[1] Ashutosh Kumar Singh, Ravi Kumar P, "A Comparative study of Page Ranking Algorithms for Information Retrieval", International Journal of Electrical and Computer Engineering 4:7 , pp. 469-480, 2009

[2] David Hawkin,"Web Search Engines", CSIRO ICT Center, pp. 86-90

[3] Eric J. Glover, Steve Lawrence, Michael D. Gordon, William P. Birmingham, C. Lee Giles, "Web Search – Your Way", ACM Digital library Volume 44 Issue 12, pp. 97-102 , December 2001

[4] "Information Retrival" available at http://en.wikipedia.org/wiki/Information_retrieval

[5] J. Kleinberg, "Authoritative Sources in a Hyper-Linked Environment", Journal of the ACM 46(5), pp. 604-632, 1999.

[6] J. Kleinberg, "Hubs, Authorities and Communities", ACM Computing Surveys, 31(4), Article No. 5, 1999.

[7] L. Page, S. Brin, R. Motwani, and T. Winograd, "The Pagerank Citation Ranking: Bringing order to the Web". Technical Report, Stanford Digital Libraries SIDL-WP-1999-0120, pp. 1-17, 1999.

[8] "Precision and Recall" available at http://en.wikipedia.org/wiki/Precision_and_recall

[9] R. Cooley, B. Mobasher and J. Srivastava, "Web Minig: Information and Pattern Discovery on the World Wide Web". Proceedings of the 9th IEEE International Conference on Tools with Artificial Intelligence, pp. (ICTAI'97), 1997.

[10] R. Kosala, H. Blockeel, "Web Mining Research: A Survey", SIGKDD Explorations, Newsletter of the ACM Special Interest Group on Knowledge Discovery and Data Mining Vol. 2, No. 1 pp 1-15, 2000.

[11] S. Brin, and L. Page, "The Anatomy of a Large Scale Hypertextual Web Search Engine", Computer Network and ISDN Systems, Vol. 30, Issue 1-7, pp. 107-117, 1998.

[12] W. Xing and Ali Ghorbani, "Weighted PageRank Algorithm", Proc. Of the Second Annual Conference on Communication Networks and Services Research (CNSR '04), IEEE, 2004.

A COMPARATIVE ANALYSIS ON IMAGE FUSION TECHNIQUES

G. Dheepa *, PhD scholar, E-mail: *dheep.thiya@gmail.com*
Prof. Dr. S. Sukumaran, *Associate Professor of Computer Science.*
Erode Arts and Science College, Erode-638009.Tamilnadu

Abstract

The development of new imaging methods in various fields arises the need of meaningful combination of all available image datasets. Image fusion is the process that combines information from multiple images of the same scene without the introduction of distortion or loss of information. The aim of image fusion is to integrate complementary as well as redundant information from multiple images to create a fused image output. The new image generated should contain a more accurate description of the scene than any of the individual source images and is more suitable for human visual and machine perception or further image processing and analysis tasks. ln recent years, image fusion has attracted increasing attention in a wide variety of applications such as concealed-weapon detection, remote sensing, intelligent robots, medical diagnosis, defect inspection, and military surveillance. This paper presents in detail the various categories, techniques and algorithms for image fusion with a comparative study.

Keywords: Image fusion, image registration, spatial domain fusion, transform domain fusion, wavelet based fusion,PCA fusion.

1.0 INTRODUCTION

1.1 Image fusion

Image fusion is the process that combines information from multiple images of the same scene, captured from different sensors. The main concept behind all image fusion algorithms is to detect strong salient features in the input sensor images and fuse these details to the synthetic image and the resulting image is referred as fused image.

Let $x_1(r)$.... $x_t(r)$ represent T images of size M_1 x M_2 capturing the same scene, where $r=(i,j)$ refers to pixel co-ordinates (i,j) in the image. The process of combining the important features from the original T images to form a single enhance image $y(r)$ is usually referred to as image fusion[20]. We categorize the image fusion according to the data entering the fusion and the fusion purpose[6].

* corresponding author

1.2 Image fusion categories

1.2.1 Multi view fusion

It is the fusion of images from same modality which are taken at the same time but from different view points.

1.2.2 Multi modal fusion

It the fusion of images coming from different modalities such as PET, CT, MRI, visible, ultraviolet, infra red etc.

1.2.3 Multi temporal fusion

It refers to the fusion of images taken at different times in order to detect changes between them or to synthesize realistic images of objects which were not photographed in a desired time.

1.2.4 Multi focus fusion

It is the fusion of the images of 3D scene taken repeatedly with various focal length.

1.2.5 Fusion for image restoration

It is of fusing two or more images of same scene and, each of them blurred and noisy may lead to a deblurred and denoised image. Multichannel deconvolution is a typical representative of this category. This approach can be extended to super resolution fusion where blurred images of low spatial resolution are fused to provide us a high resolution images.

1.3 Basic stages of image fusion

In each of the above said category,while fusing the images, due to the different sensor viewpoints, there might exist some mis-correspondence between several points of the observed scene .Therefore registration of images is done before fusing the images. Image Registration is the process of establishing point-by-point

correspondence between a number of images, describing the same scene. Image registration works usually in four steps.

1.3.1. Feature detection

The salient and distinctive objects (corners,line intersections, edges, contours, closed boundary regions etc.)are manually, or preferably automatically detected.

1.3.2 Feature matching

In this step, the correspondence between the features detected in the reference image is established.

1.3.3 Transform model estimation

Here, the type and parameters of the so called mapping functions, aligning the sensed image with the reference image are esti mated.

1.3.4 Image re-sampling and transformation

In this step,the sensed image is transformed by means of the mapping functions. Image values in non-integer co-ordinates are estimated by an appropriate interpolation technique.

2.0 IMAGE FUSION TECHNIQUES

There are various techniques that have been developed to perform image fusion[2]. They can be broadly classified into two groups

1. Spatial domain fusion techniques
2. Transform domain fusion techniques.

2.1.Spatial domain fusion technique

In this technique, the input images are fused in the spatial domain i.e using localized spatial features such as gradient, spatial frequency and local standard deviation. Assuming that *g(.)* represents the fusion rule, spatial domain fusion technique can be summarized as follows,

$$Y(r) = g(x_1(r), x_2(r) \ldots\ldots x_t(r))$$

The fusion process deals with the original pixel values[7]. Pixel level fusion uses a transformation on to perform data fusion. Some of the spatial domain fusion methods are,

- Averaging Method
- Brovey Transform method
- PCA Method
- IHS method

2.1.1 Averaging method

This is a basic and straight forward technique and fusion could be achieved by simple averaging corresponding pixels in each input images. Let the input images be $I_1(x,y)$ and $I_2(x,y)$, then

$$I_f(x,y) = \frac{I_1(x,y) + I_2(x,y)}{2}$$

2.1.2 Brovey transform based image fusion

The basic procedure of the Brovey transform first multiplies each MS band by the high resolution PAN band, and then divides each product by the sum of the MS bands. The algorithm is shown in the equation below.

$$DNFused = DNpan \times DN_{b1} / (DN_{b1} + DN_{b2} + DN_{b3})$$

where DNfused means the digital number (DN) of the resulting fused image; DNb1, DNb2 and DNb3 stand for pixel values of three bands of multiple spectral image; DNpan stand for pixel values of high resolution Pan band.

2.1.3 Principal Component Analysis (PCA) based image fusion

The PCA transform converts inter-correlated multi-spectral (MS) bands into a new set of uncorrelated components. To do this approach first we must get the principle components of the MS image bands. After that, the first principle component which contains the most information of the image is substituted by the panchromatic image. Finally the inverse principal component transform is done to get the new RGB (Red, Green, and Blue) bands of multi-spectral image from the principle components[2].

2.1.4 Intensity-hue-saturation (HIS)based image fusion

The intensity-hue-saturation (HIS) fusion converts a color MS image from the RGB space into the IHS color space. The HIS components can be defined as follows:

$I=(R+G+B)/3$

$H=(B-R) / 3(I-R)$, $S=1-R/I$,where $G=MIN(R,G,B)$

$H=(R-G) / 3(I-G)$, $S=1-G/I$,where $G=MIN(R,G,B)$

$H=(G-B)/ 3(I-B)$, $S=1-B/I$, where $B=MIN(R,G,B)$

where I,H,S stand for Intensity, Hue and Saturation components respectively; R, G, B mean Red, Green, and Blue bands of multi-spectral image.

Because the intensity(I) band resembles a panchromatic (PAN) image, it is replaced by a high-resolution PAN image in the fusion. A reverse IHS transform is then performed on the PAN together with the hue (H) and saturation (S) bands, resulting in an IHS fused image.

These image fusion methods are often successful at improving the spatial resolution, however, they tend to distort the original spectral signatures to some extent[5].

2.2 Transform domain fusion techniques.

In this technique, source images are projected onto localized bases which are usually designed to represent the sharpness and edges of an image and therefore describe the image using a more meaningful representation that can be used to detect and emphasize the salient feature of images which are more clearly depicted than in the spatial domain.

Let $T\{.\}$ represents a transform operation and g(.) represents a transform rule. Transform domain fusion technique can be outlined as follows,

$$Y(r)=T^{-1}\{g(T\{x1(r)\},.....\{x_T(r)\})$$

It was found that better results were obtained if the fusion was performed in the transform domain. The basic idea is to perform multi resolution decomposition on each source image, then integrate all these decompositions to form a composite representation, and finally reconstruct the fused image by performing an inverse multi resolution transform.

The decade of 1980's saw the introduction of pyramid transform - a fusion method in the transform domain. An image pyramid [16] consists of a set of low pass or bandpass copies of an image, each copy representing pattern information of a different scale. At every level of fusion using pyramid transform, the pyramid would be half the size of the pyramid in the preceding level and the higher levels will concentrate upon the lower spatial frequencies.

The basic idea is to construct the pyramid transform of the fused image from the pyramid transforms of the source images and then the fused image is obtained by taking inverse pyramid transform. Most commonly used pyramid transform fusion methods are

1. Laplacian Pyramid
2. Filter Subtract Decimate Pyramid
3. Morphological pyramid
4. Ratio-of-low pass Pyramid

With the development of wavelet theory , the multi-scale wavelet decomposition has taken the place of pyramid decomposition[11].The wavelet theory was introduced as a mathematical tool in 1980s and it has been extensively used in image processing that provides a multi-resolution decomposition of an image in a biorthogonal basis and results in a non-redundant image representation.

An alternative to fusion using pyramid based multi- resolution representations is fusion in the wavelet transform domain. The wavelet transform decomposes the image into low-high, high-low, high-high spatial frequency bands at different scales and low-low band at the coarsest scale[15].

Wavelet transform fusion schemes offer several advantages over similar pyramid based fusion schemes .

(1) wavelet transform provides directional information while the pyramid representation does not introduce any spatial orientation in the decomposition process.

(2) In pyramid based fusion, the fused images often contains blocking effects in the regions where the input images are significantly different. There are no such artifacts in similar wavelet based fusion results.

(3) Images generated by wavelet image fusion have better signal-to-noise ratios than images generated by pyramid image fusion when the fusion rules are used.

(4) When subject to human analysis also,wavelet fusion results are better perceived.

The information flow in one level of 2-D image decomposition is illustrated in Fig. 3 and 3 levels of decomposition is shown in fig 4.

Wavelet separately filters and down

samples the 2-D image in the vertical and horizontal directions (separable filter bank). The input (source) image is I(x,y) filtered by low pass filter L and high pass filter H in horizontal direction and then down sampled by a factor of two (keeping the alternative sample) to create the coefficient matrices IL(x,y) and IH (x,y) .

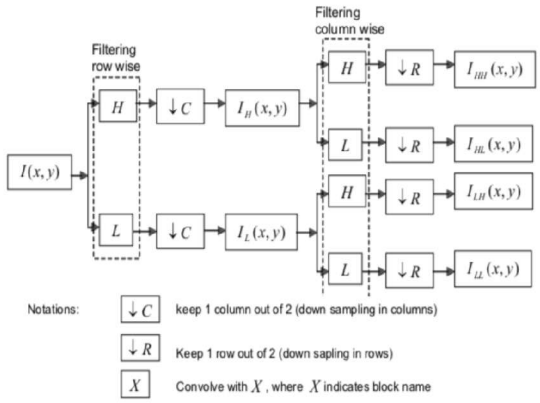

Fig.3. Information flow of one-level of 2-D decomposition

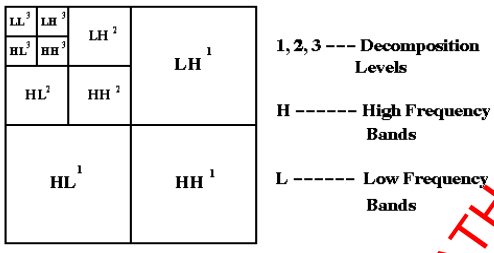

Fig.4. 3 levels of 2-D decomposition

The coefficient matrices IL(x,y) and IH(x,y) are both low pass and high pass filtered in vertical direction and down sampled by a factor of two to create sub bands (sub images) ILL(x,y) , ILH(x,y) , IHL(x,y) , and IHH (x,y) .

The $I_{LL}(x,y)$ contains the average image information corresponding to low frequency band of multi scale decomposition. It could be considered as smoothed and sub sampled version of the source image $I(x,y)$.It represents the approximation of source image $I(x,y)$. $I_{LH}(x,y)$, $I_{HL}(x,y)$ and $I_{HH}(x,y)$, are detailed sub images which contain directional (horizontal, vertical and diagonal) information of the source image $I(x,y)$, due to spatial orientation. Multi-resolution could be achieved by recursively applying the same algorithm to low pass coefficients from the previous decomposition[14].

Inverse 2-D wavelet transform is used to reconstruct the image $I(x,y)$, from sub images $I_{LL}(x,y)$, $I_{LH}(x,y)$, $I_{HL}(x,y)$ and $I_{HH}(x,y)$, as shown in fig. 5. This involves column up sampling (inserting zeros between samples) and filtering using low pass $\tilde{L}$ and high pass filter $\tilde{H}$ for each sub images. Row up sampling and filtering with low pass filter $\tilde{L}$ and high pass filter $\tilde{H}$ of the resulting image and summation of all matrices would construct the image $I(x,y)$

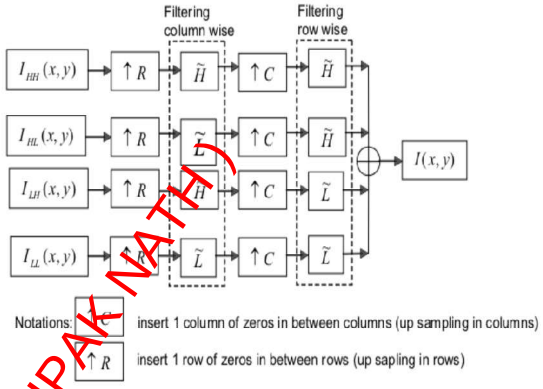

Fig.5. Information flow of one-level of 2-D reconstruction

2.3 Image Fusion by Discrete Wavelet Transform(DWT)

The information flow diagram of discrete wavelet- based image fusion algorithm is shown in *Fig.6*

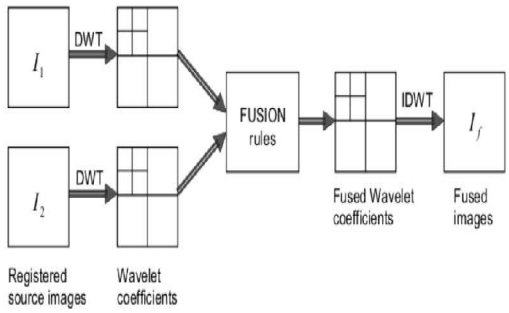

Fig.6. Information flow of discrete wavelet based image fusion

The fused image ($I_f(x,y)$) could be obtained by taking the inverse discrete wavelet transform (IDWT) as:

$$I_f(x,y) = IDWT \left[\phi\{DWT(I_1(x,y)), DWT(I_2(x,y))\}\right]$$

3. FUSION METHODS COMPARISON

Meaningful comparison of image fusion methods is often dependent on the application. For some applications (e.g medical image fusion) the aim of the fusion is to combine perceptually salient image elements such as edges and high contrast regions. Evaluation of fusion techniques for such applications can only be effectively based on a perceptual comparison. Apart from visual appearance quantitative analysis is done over the fused images . Therefore the comparison is of two types.

1. Qualitative comparison
2. Quantitative comparison

3.1 Qualitative comparison

For the visual evaluation the following criterion is considered:natural appearance , brilliance contrast,presence of complementary features,enhancement of common features etc.

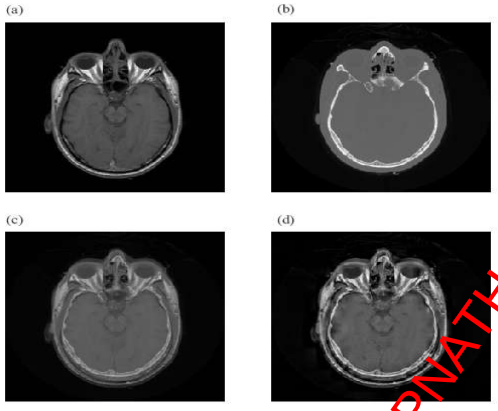

Fig .8. (a) First image (MR) of medical test set (b) Second Image(CT) of medical test set (c) Fused image using Average Pixel values (d) Fused Image using DWT

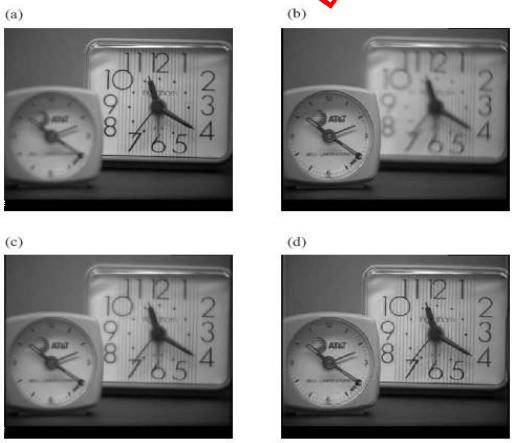

Fig .9. (a) First image of Multi focus test set (b) Second Image of Multi focus test set (c) Fused image using Average Pixel values (d) Fused Image using DWT

By visual Comparison,Fig .8 shows that DWT preserves the subtle regions of the brain in the MR image better than the average pixel method. Also Fig.9. shows that DWT gives more clear multi focus fused image than average pixel method.

3.2 Quantitative comparison

For Quantitative comparison, firstly a "ground truth" image has to be created that can be quantitatively compared to the fusion result images. This is produced using a single cut-and-paste technique, physically taking the "in focus" areas from each image and combining them. The qualitative measure used to compare the cut-and-paste image to the fused image was taken from [21].

$$\rho = \sqrt{\frac{\sum_{i=1}^{N}\sum_{j=1}^{N}[I_{gt}(i,j) - I_{fd}(i,j)]^2}{N^2}}$$

where I_{gt} is the cut-and-paste "ground truth" image , I_{fd} is the fused image and N is the size of the image. Lower values of ρ indicate greater similarity between the images I_{gt} and I_{fd} and therefore more successful fusion in terms of quantitatively measurable similarity.

4. EXPERIMENTAL RESULTS AND ANALYSIS

The qualitative measure ρ is calculated for Average Pixel, PCA and DWT fusion methods which are given in table .1

Fusion method	ρ
Average pixel	8. 3553
PCA	8. 3737
DWT	7. 6551

Tab 1. Results of Average Pixel, PCA, DWT methods

Table1. shows the results of comparison of ρ values of all the three methods. It depicts that the value for average pixel value method is higher than PCA and DWT. So it gives only a baseline result. The PCA method gives a equivalent but still it is also a worse result. These methods have poor results when compared to DWT method .

5.0 CONCLUSION

This paper presents the various categories, stages and techniques for image fusion. For an effective fusion of images, a technique should aim to retain important features from all input images. These features often appear at different positions and scales. Simple non-resolution methods of image fusion such as averaging and PCA methods produces only limited results. DWT method provide better results when compared qualitatively and quantitatively. So we inference that DWT fusion methods provide computationally efficient image fusion techniques and is most used among all the discussed methods in this paper .

References

[1] K.Shivsubramani, P soman, Krishnamoorthy, "Implementation and Comparative Study of Image Fusion Algorithms", *International Journal of Computer Applications (0975 – 8887) Volume 9– No.2,* November 2010,pp 3-6

[2] Anjali Malviya and S.G.Bhirud ,"Image Fusion of Digital Images" , *International Journal of Recent Trends in Engineering,* Vol.2, No.3, November 2009.pp.2-4

[3] V.P.S Naidu and J.R.Raol, "Pixel level Image fusion using wavelets and Principal component analysis". *Defence science Journal,Vol.58,No.3, May 2008*, pp 338-352.

[4] S. G. Nikolov , D. R. Bull ,C. N. Canagarajah , M. Halliwell and P. N. T. Wells " 2D image fusion by multiscale edge graph combination" in *3 rd International Conference on Image fusion (Fusion 2000).Paris,France, 10-13 July* , International Society of Image Fusion (ISIF)vol 1,.2000b. pp. MOD 3-16-22

[5] Z. Zhang and R. Blunm ," A categorization of Multiscale-decomposition-based image fusion schemes with a performance study of digital camera application" , *Proceedings of IEEE* , 1999.pp.1315-1358

[6] Dr.Nikolaos Mitianoudis ," Image -Fusion: Theory and Applications", *Http://www.iti.gr/iti/files/document/ seminars/iti_mitianoudis_280410.pdf*

[7] A. Goshtasby and S. G. Nikolov, "Image fusion: Advances in the state of the art" *Editorial- Science Direct , Special Issue on Image fusion,* 8(2),April 2007: pp.114-118.

[8] N. Mitianoudis and T. Stathaki, "Pixel-based and region-based image fusion schemes using ICA bases". I*nformation Fusion, Special Issue on Image fusion: Advances in the state of the art, 8 (2):April 2007, pp.131-142,*

[9] *http://en.wikipedia.org/wiki/ Principal_components_analysis*

[10] H.Wang, J. Peng, &W. Wu,"Fusion algorithm for multisensor image based on discrete multiwavelet transform", *IEEE Proc. Visual Image Signal Process.*,2002, 149(5).

[11]Mitra Jalili-Moghaddam,"Real-time multi-focus image fusion using discrete wavelet transform and Laplasican pyramid transform",*Masters thesis Chalmess University of Technology, Goteborg, Sweden*,2005.

[12] G. Pajares and J. M. Cruz ," A wavelet based Image fusion tutorial", *Pattern Recognition* ,vol 37, No.9 2004 . pp.1855-1872

[13] Nedeljko Cvejic, Artur Loza, David Bull & Nishan Cangarajah, "A similarity metric for assessment of image fusion algorithms". *International Journal of Signal Process.*, 2005, 2(3), pp.178-82.

[14] Blum, S. Rick & Liu Zheng, "Multi-sensor image fusion and its applications", *CRC Press, Taylor & Francis Group, Boca Raton*, 2006.

[15] Eduardo Fernandez Canga. ," Image Fusion", *Eng. Project Report, University of Bath ,June 2002.*

[16] Peter J. Burt and Edward H. Adelson ," The Laplacian Pyramid as a compact image code", *IEEE Transactions on Communications* ,vol-com 31, No.4 1983 . pp.532-540

[17] P. J. Burt and R. J. Kolzynski , "Enhanced image capture through Fusion", *Proceedingss of the 4 th International conference on computer vision"*,1993,pp. 173-182.

[18*http://en.wikipedia.org/wiki/mathematical_morphology*

[19] J. J. Lewis, R. J. O'Callaghan, S. G. Nikolov, D. R. Bull and N. Canagarajah, "Pixel- and region-based image fusion with complex wavelets." *Information Fusion, Special Issue on Image fusion: Advances in the state of the art*, 8(2):April 2007,pp.119-130,

[20] T.Stathaki ,"Image fusion:Algorithms and Applications" .New York:Academic, 2008

[21] Stavri Nikolov, Paul Hill, David Bull and Nishan Cangarajah,"Wavelets for Image Fusion", Center for Communications Research,University of Bristol, Bristol, UK , 2001, pp.23 -24

Gesture Recognition: An interactive communication system

Bhavish Sushiel Agarwal
Yahoo R&D
Bangalore, India
Bhavag@yahoo-inc.com

Jyoti R. Desai
Freelance academician
New Delhi, India
Jyothirdesai@pes.edu

***Abstract*— Gesture recognition has gained a lot of importance over the past few years. With the progress in technology, the need for faster communication between different devices has taken the priority. As has been the method so far, a number of clicks are required by the user before the actual communication between devices or data transfer from one place to another takes place. A better system would entail the user performing simple hand gestures towards the device and corresponding actions will take place in the system. Thus, with minimal effort from the user, efficient interaction can take place with and between systems.**

In this paper we propose an interactive system, which uses human gestures to perform an activity such as transfer of data between different devices (e.g mobile devices, computers, tablets, PC)

***KeyWords*— HCI, Gesture Recognition, Mobile devices, Natural Actions, Applications of mobile embedded systems.**

I. INTRODUCTION

Portable devices such as mobile phones, laptops, tablet etc. have turned into the basic necessities of the day. With the constant improvements in these fields, there is a tremendous use of mobile devices for various purposes like taking pictures, writing documents, showing presentations etc.

Gesture recognition is an effective tool in language generation process [6]. Engineering research also strives to create a system of device control using gesture recognition. In the present paper the authors aim to present a novel method of gesture recognition.

The advancement in the operating system for mobile devices allows users to develop vast range of applications. At the end of the day there is also a need to use the same data on multiple systems or devices as well, for example the pictures might need to be edited before they can be shown to the rest of the world or there might be a need to add some notes using a tablet to be used on the system.

Devices like Kinect controllers allow some easy interaction between the user and the gaming system and enhance the user experience. Such a system can also be used to communicate with the computer. But such systems suffer from noise disturbances where any third person can come between the user and the system and thus spoil the experience for the user.

Also a number of online applications are available wherein the user can synchronize his/her files with another system. Yet again the total interaction needed for this purpose is not as user friendly as it could be.

Mobile devices are very common and majority of the people use smart phones in their daily lives. Their interactions with these devices can be made easier by using such gesture recognition features. For example, if the user needs to transfer a file from his mobile device to the tablet or a computer in front of him, he can simply perform the drop action and the transfer will be done. To perform a move operation to another window, he can move the phone to the left or right depending on whichever side he wants to move the window to.

All the concerned data will be stored over the cloud pertaining to the current user and no one else can access this data apart from that particular user. This adds to constraints where we need the user to be logged in to an application in the mobile devices and computer. The data transfer or the actions only take place if the user is authenticated to the system. Once this is done the user can simply transfer or control the other system using his hand or mobile device.

This authentication before the use of API also helps improve security. Thus the inclusion of facial or voice recognition along with gesture recognition feature ensures a secure access to the services even after prolonged usage of the software and the hardware.

Once the user's face or voice is recognized, an unhindered use of the gesture recognition feature is allowed for the next hour based on the security needs for the device after which the key will be issued again by the cloud.

II.RELATED WORK

[10] is a survey paper which speaks about the various gesture recognition techniques with an emphasis on hand gestures and facial recognition. [12] Talks about gesture recognition using Bezier curves from registered 3D data. [2] Presents a very novel method of gestures by using quadratic curves to recognize the gesture. [15] Talks about dynamic hand gestures via the use of Kalman filter based hand tracking and a HMM based temporal characterization scheme.[13] is another HMM based algorithm where time-sequential images is transformed into an image feature vector sequence, and eventually to a symbol sequence by vector quantization. [18] Explains a seamless way of passing data among multiple users and devices.

Viola and Jones proposed an algorithm, called Haar Classifiers, to rapidly detect any object, including human faces, using AdaBoost classifier cascades that are based on Haar-like features and not pixels [7].

Haar classifier [3] is used to accurately detect facial features. Recognizing other gestures like hand movements requires that the Haar classifier cascades be trained first.

Intel developed an open source library devoted to easing the implementation of computer vision related programs called Open Computer Vision Library (OpenCV). The OpenCV library, designed to be used in conjunction with applications that pertain to the field of HCI, robotics, biometrics, image processing, and other areas where visualization is important and includes an implementation of HAAR classifier detection and training [4].

III.FRAMEWORK

Libraries are developed so that the developers can easily integrate the API calls to the data cloud without breaking any previous known functionality of the application. Libraries run asynchronously parallel to the application thread, hence the performance of the application is untouched. We use a simple application that communicates using the API, explaining how the above procedure happens.

Application first needs to authenticate the user by calling the Authentication API of the system. Once the authentication key is sent to the user, the application now registers all the events that gesture or device framework should look out for. Whenever the user performs a hand gesture over the camera or moves the phone in a particular gesture, event is fired by the system and the call back takes over to send the information to the cloud. The information here can be anything from a URL, or an image, a video or a document that is to be stored against a particular user. Any type of data can be stored over in the cloud to the user. If the application does not need to store and can function only by making use of the event services then it can disable the data usage while registering the API use. The services are split into two parts, one is the hand gesture recognition API's and the other is the device based gestures. The latter is for mobile devices that include a gyroscope and an accelerometer. Now we take a couple of use cases and see how they are combined and used. Authentication by default is assumed.

A. Application on the desktop

When the user needs to transfer a file from the desktop to another mobile device or another computer on the cloud, he does the natural action of grabbing the file from the current window and then going to the other system and dropping it in front of it. The current data on the device window, which may be a URL or a file, is transferred to the data cloud. And the other side where the drop action is performed is notified about the user activity and then the URL is transferred to the application where it can then be used appropriately.

B. Application on the phone to other devices

If there is a file transfer from the phone to another device, the user needs to perform simple drop action like moving the phone downwards towards the system and the file that needs to be transmitted will be transferred to the system. Again the receiving system will notify the user once the download is finished on the system. For the live actions like switching windows or moving in the presentation, an initial pairing of the system with special parameters needs to be performed. Then the user can move his phone in different directions, without even being in the proximity of the system and perform all the required actions with the system. If we need to switch to the next window screen we move the phone from the horizontal position to vertical position. Fig.1 explains how one application is transferring a video on the phone over to the user's browsers.

IV.THE SYSTEM OVERVIEW

1. 1. The application is synchronized to the cloud after the user is authenticated. Henceforth it will run in the background of the application.
2. 2. It waits and scans for events to be generated by the user.
3. 3. When the user performs a gesture, the event is recognized and is sent to the data cloud. If there is data present then it is sent along with the event to the cloud.

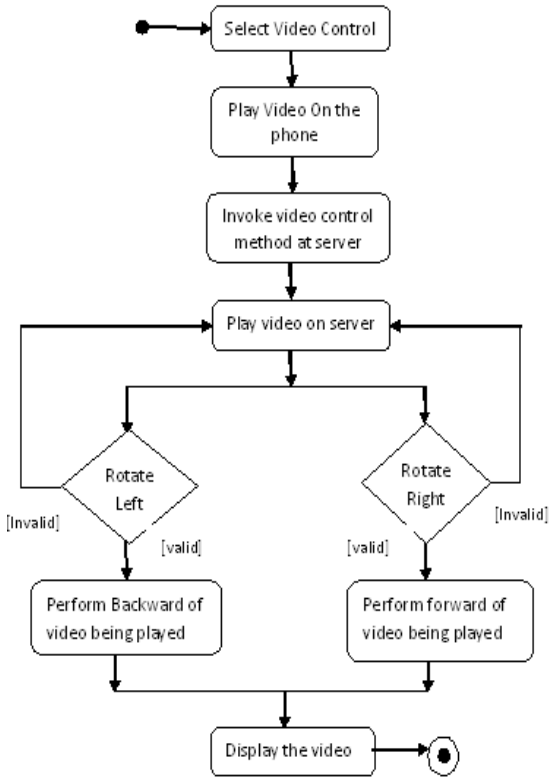

Fig.1

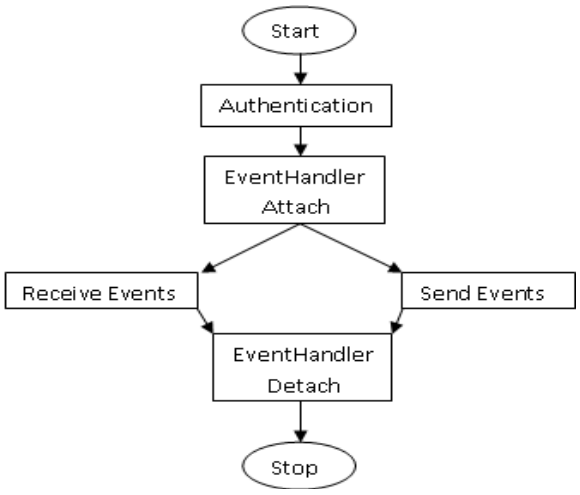

Fig 2.Over all Architecture

4. Data cloud stores history of the activity performed by the user along with the data pertaining to the application where the activity is performed.
5. When the user performs another action on the same application that the previous action that was performed then will be a transfer depending to the particular type of event.
6. The application downloads the information in the required format use it to perform further processing.
7. After every hour, for security the user face recognition must be performed, to get fresh key to the application which then can be used again.

A. Mobile Gesture and Actions

A mobile device has an accelerometer and gyroscope which is what we make use of to find out what gesture the user is performing. Accelerometer is a dynamic sensor capable of a vast range of sensing. Accelerometers that can measure acceleration in one, two, or three orthogonal axes are available. They are typically used in one of the following three modes:

- As an inertial measurement of velocity and position;
- As a sensor of inclination, tilt, or orientation in 2 or 3 dimensions, as referenced from the acceleration of gravity (1 g = 9.8m/s^2);
- As a vibration or impact (shock) sensor

A gyroscope is a device for measuring or maintaining orientation, based on the principles of angular momentum. In essence, a mechanical gyroscope is a spinning wheel or disk whose axle is free to take any orientation. Although this orientation does not remain fixed, it changes in response to an external torque much less and in a different direction than it would without the large angular momentum associated with the disk's high rate of spin and moment of inertia. Since mounting the device in gimbals minimizes external torque, its orientation remains nearly fixed, regardless of any motion of the platform on which it is mounted.

From the above we derive the Rotational vector sensor that we can use in the device. The rotation vector represents the orientation of the device as a combination of an angle and an axis, in which the device has been rotated through an angle θ around an axis (x, y, or z). The following code shows you how to get an instance of the default rotation vector sensor.The three elements of the rotation vector are expressed as follows:

x*sin(θ/2) y*sin(θ/2) z*sin(θ/2)

Where the magnitude of the rotation vector is equal to sin(θ/2), and the direction of the rotation vector is equal to the direction of the axis of rotation. The three elements of the rotation vector are equal to the last three components of a unit quaternion (cos(θ/2), x*sin(θ/2), y*sin(θ/2), z*sin(θ/2)). Elements of the rotation vector are unit less. The x, y, and z axes are defined in the same way as the acceleration sensor. The reference coordinate system is defined as a direct orthonormal basis (see figure 3). This coordinate system has the following characteristics:

X is defined as the vector product Y x Z. It is tangential to the ground at the device's current location and points approximately east.

Y is tangential to the ground at the device's current location and points toward the geomagnetic North Pole.Z points toward the sky and is perpendicular to the ground plane.

Now since we have the rotational values of the phone we can use that to find out what kind of moment the phone has moved. This is similar to tilt of the phone. But since the movement can be highly rotational in nature we use the above one. To improve the kind of actions we can use with the user we also use the accelerometer reading to figure out what the user is going to do. The values x , y , z, p , q , r that we derive from the above, where x, y, z are the acceleration values , p, q, r are the rotational vector values , compare with the data that we have predefined in the system. When the values have the distance less than the threshold to decide what action has occurred then we decide what event to rise. The Server is then notified about the action that is performed. If there is a drop action then the files are uploaded to the server. The server sends a notification to the mobile once the action has been completed on the device.

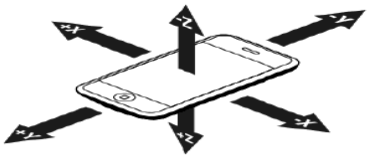

Fig 3

B. The other client

If the phone is the device that was used to instantiate the communication then the other devices receiving the actions are possibly another mobile device and a computer. For the system to know where the particular data must be transferred from the previous screen so that a 1-1 communication is done, it must be in ready state, always checking the environment for any sort of events that can occur. One thing that the system does is template matching to look out for any phone action that was performed by the user in front of the particular system.

Template matching is a technique in digital image processing for finding small parts of an image, which match a template image. For templates without strong features, or when the bulk of the template image constitutes the matching image, a template-based approach may be effective. Since template-based template matching may potentially require sampling of a large number of points, it is possible to reduce the number of sampling points by reducing the resolution of the search and template images by the same factor and performing the operation on the resultant downsized images (multi-resolution, or pyramid, image processing), providing a search window of data points within the search image so that the template does not have to search every viable data point, or a combination of both. The next feature that it tracks is the hands using the fast HAAR classifier to find the hand in the frames of the image, which then follows the use of cam-shift to track the various hand positions. Now if an object like another phone or if a hand is found in the screen then we flag them and we follow their actions. If the server replies back with the positive saying a communication was done with the system then we can do the data transfer to the system.

C. Data Cloud

It acts as a middleman and keeps all the systems in sync with each other. The server has the job of pairing the systems up if there is an action taken, and a job to allow the transfer of the data if the transfer action is performed by the user. When the request comes in from the client, the entire request class is pushed into the request queue and action queue of the system. And once the other client tells the download gesture was made to this system, the last action is popped from the queue and sent to this system. If the request was made for actions between the two systems, then these 2 systems are paired by sending the IP address to each other. Also the server pops the request from the action queue. Direct p2p communication between the two systems is initiated. It prevents the additional latency that may occur if the transfer is not made directly between the two systems. The Queues are maintained so that the data is sent in a sequential order to the user. The queues are flushed after a given amount of time if the user does not perform any action of transfer on the other system. Also devices that have been enabled for p2p communication for actions to happen are checked at regular intervals so make sure that the communication is live between those systems.

D. Efficiency

The system on the whole works as a background process and only communicates when there is a particular event that is triggered by the the system. All the communication that occurs in the system happens with minimal data transfer between the systems hence the bandwidth of the user is not affected. No additional need of hardware resources is needed. It can be implemented across various platforms which have a camera and accelerometer installed in them.

V.FUTURE ENHANCEMENTS

- *Security:*

To verify that the hand gestures are performed by an authorized person, the face recognition of the user feature is to be added. The user is required to verify him/her before using the gesture recognition feature. Once the face is verified, the gesture can be performed. We can also assure secured gesture recognized data transfer by verifying the thumb impression. This verification process can be repeated every hour.

- The file selected by the gesture will be uploaded and will be waiting in the queue. If there is no sequential download action to other devices, then the file selection might not be the intended action. Hence, for the next action for the file transfer still have the same earlier file which will be present in the queue. Therefore we can consider the threshold time and beyond which the file from the queue has to be deleted. In another scenario wherein there are two sequential select actions, then the first file uploaded should be deleted.

REFERENCES

[1] John G. Allen, Richard Y. D. Xu, Jesse S. Jin , Object Tracking Using CamShift Algorithm and Multiple Quantized Feature Spaces, Pages 3-7, IP '05 Proceedings of the Pan-Sydney area workshop on Visual information processing

[2] Qiulei Dong, Yihong Wu, and Zhanyi Hu, Gesture Recognition Using Quadratic Curves. ACCV (1) 2006: 817-825

[3] Bhavish.S.Agarwal, Jyothi Desai and Snehanshu Saha; A Fast Haar Classifier based Gesture Recognition using CamShift Algorithm and Curve Fitting method. IJCSI Vol 1, Iss 4, 21-25

[4] Open Computer Vision Library Reference Manual. Intel Corporation, USA, 2001.

[5]www.itl.nist.gov/div898/handbook/pmd/section1/pmd141.htm

[6] D. McNeill and E. Levy. Conceptual Representations in Language Activity and Gesture, pages 271-295. John Wiley and Sons Ltd, 1982.

[7] Viola, P. and Jones, M. Rapid object detection using boosted cascade of simple features. IEEE Conference on Computer Vision and Pattern Recognition, 2001.

[8] Yaav Freund, Robert E. Schapire. “A decision-Theoritic Generalization of on-Lianer and an Application to boosting”

[9] An algorithm for restricted least square regression , RL Dykstra - Journal of the American Statistical Association, 1983 – JSTOR

[10] Gesture Recognition: A Survey ,SushmitaMitra, Senior Member, IEEE, and TinkuAcharya, Senior Member, IEEE,IEEE transactions on System , Man and Cybernetics.

[11] Recognition System, MokhtarM.Hasan, Pramod K. Mishra, HSV Brightness Factor Matching for Gesture ,International Journal of Image Processing (IJIP), pages 457-467,Volume (4): Issue (5)

[12] Min C. Shin, Leonid V. Tsap, Dmitry B. Goldgof, Gesture recognition using Bezier curves for visualizationnavigation from registered 3-D data, Pattern Recognition 37 (2004) 1011 – 1024

[13] Yamato, J., Ohya, J., Ishii, K.: Recognizing human action in time-sequential images using hidden markov model. In: Proc. IEEE Conf. Computer Vision and Pattern Recognition, Champaign, IL (1992) 379-385

[14] Kjeldsen, R., Kender, J.: Finding skin in color images. In: Proc. IEEE Workshop on Automatic Face and Gesture recognition, Killington, Vermont, USA (1996) 312-317

[15] Aditya Ramamoorthy, Namrata Vaswani, Santanu Chaudhury, Subhashis Banerjee, Recognition of dynamic hand gestures, Pattern Recognition 36 (2003) 2069 – 2081

[16] http://developer.nvidia.com/

[17] Phillip Ian Wilson , Dr. John Fernandez , Facial feature detection using HAAR classifiers, pages 127-133 , Journal of computing sciences in colleges Volume 21 Issue 4 , April 2006

[18] P. Mistry, S. Nanayakkara, P. Maes. **SPARSH – Touch the Cloud.** To be appear in CSCW2011. Demo. Hangzhou, China. 2011

[19] P. Mistry, S. Nanayakkara, P. Maes. **SPARSH: Passing Data using the Body as a Medium.** To be appear in CSCW2011. Interactive Paper. Hangzhou, China. 2011

RETINAL PATTERN MATCHING USING THE METHOD OF GABOR FILTER

Srikanth Prabhu
Gowardhan Hegde
Tushar Mungle

Department of Computer Science and Engineering
Manipal Institute of Technology, Manipal

Srikanth_prabhu@yahoo.com govardhan.hegde@manipal.edu tushar_mungle@yahoo.co.in

Abstract: In this paper we give an innovative approach for extracting the crosspoints for various parameters for the same image using the Gabor filter. The different parameters used in Gabor filter are frequency, wavelength, x and y coordinates, phase angle, aspect ratio. Using this method we get different sets of crosspoints for the same image. So better approximate results can be gathered from this method as better clarities can be obtained in terms of classification and matching. Forensic experts get lots of problems when the error between a set of distances are within some specific decimal values. So if different intensities can be targeted using different frequencies, we get an alternative solution to an already existing one when the error is very small. This method also helps the medical physicians as it gives a confirmation whether the person has a disease or no. So we modify the different Shape Extractor algorithms by bringing in frequency as a parameter we get better confirmative results.

Keywords: Biometric, Gabor Filter, crosspoints.

1. INTRODUCTION

Gabor Filters are cosine transform based filters which are harmonic in nature. These filters help to target all feature points in an image as intensities and frequencies are proportional to each other. In this paper we apply the Gabor Filter by first finding the texture of the image. Here the image is the retina. Fig 1 shows the sample image.

Fig 1: Sample image.

One such application on a retina is shown below.

Fig 2: Texture of an image

The texture extracts the region where the arteries and veins are located. We can clearly see it from the figure. The textures for retinas in different directions (left or right) are shown below.

Fig 3: Texture of left eye of fundus image

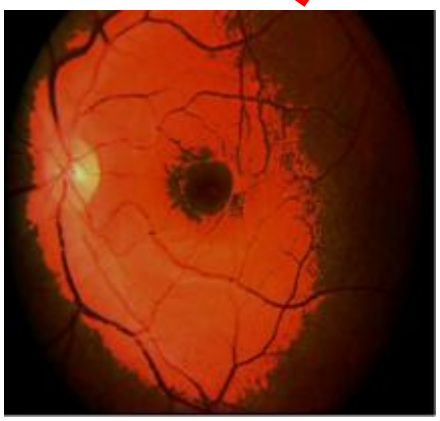

Fig 4: Textures of right eye of fundus images.

The different textures are obtained by applying different thresholds on the intensities of the images [4][8].

Gabor Filter

A Gabor Filter is made up of an exponential term multiplied by cosine term which is a harmonic function. A Gabor Filter function is dependent on the dimension of the image, aspect ratio, wavelength and the phase angle. One example of Gabor matrix is given by:

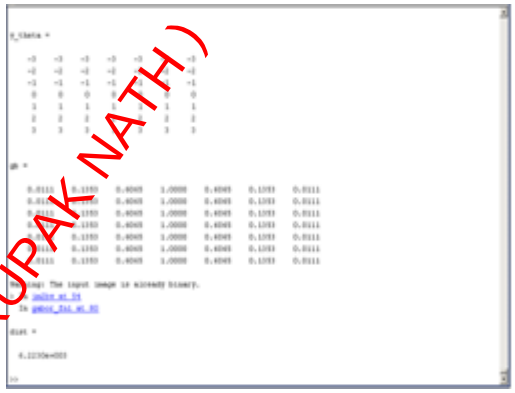

Fig 5: A well generated Gabor Matrix.

The above figure shows a 7 by 7 matrix (Aspect Ratio=1).

2. METHODOLOGY

2.1 Gabor Filter Methodology of extracting the cross points:

Detection of Bifurcation Points by Extraction of Shapes (Gabor Filter).

After reading the image, it is converted into gray scale and then the maximum pixel intensity minus the minimum pixel intensity is found out for a pixel in a neighborhood. Then we use the line-structuring element for dilating the image. Finally convolve the image with a 3×3 matrix to find the bifurcation points of shapes 'Y'[3][4] and mark these points. From all these methods we gather some information about some extra features

which look to be outside the scope of bifurcation point's extraction. So we thought of going into Disease recognition (Diabetes) because these features mainly correspond to diabetic parameters.11_ 27 Then we thought of calculating the color parameters of these features in terms red, green, blue. From the literature we gathered, we could analyze that green component had a lot of role to play to extract the vessels, exudates and the optical ball where as the red component was significant to extract the micro aneurysms[4] and haemorrhages[4]. These features are a must to be extracted because unlike the fingerprints, retina has always a chance of getting diseased over a period of time. So Biometric systems based on retina also gives some extra information with respect to the behavior of a person in terms of disease.

The steps for Gabor filter are as follows:
(a) Read the image.
(b) Convert the image to black and white.
(c) Find Maximum–Minimum for each pixel.
(d) Find edge of the image using Sobel operator.
(e) Using structuring element as line, dilate the image.
(f) Convolve the image with a three by three matrix which is of shape Y.
(g) Mark those points.

The Gabor Filter takes the form

Step 1: Convolve the Gabor filter as shown below with the image texture.

$$g(x, y; \lambda, \theta, \psi, \sigma, \gamma) = \exp\left(-\frac{x'^2 + \gamma^2 y'^2}{2\sigma^2}\right) \cos\left(2\pi \frac{x'}{\lambda} + \psi\right)$$

where

$$x' = x\cos\theta + y\sin\theta$$

and

$$y' = -x\sin\theta + y\cos\theta$$

x, y are co-ordinates λ is wave length, θ is the phase angle, ψ is the phase offset, and γ is the spatial aspect ratio, and specifies the ellipticity of the support of the Gabor function[2][6]. Here x and y takes different values generated from the Grid.

Step 2: Store the Gabor matrix.

The equations supporting Gabor transform are given by:

```
for x = - fix(Sx) : fix(Sx)
    for y = - fix(Sy) : fix(Sy)
        G (fix (Sx) + x + 1 , fix(Sy) + y
+1 ) =
(1/ (2*pi*Sx*Sy)) * exp(-.5*((x/Sx)^2 +
(y/Sy)^2)+2*pi*i*(U*x + V*y)) ;
    end
end
```

where Sx, Sy[6] means the variances in the x and y directions and U and V are centre frequencies respectively. The results are shown in Figure 6(a,b.c.d) from top to bottom.

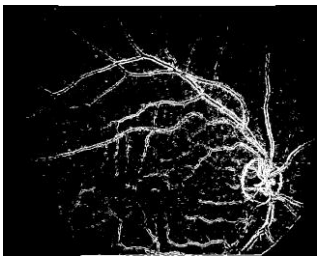

Fig 6.a

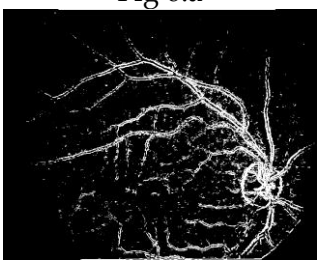

Fig 6.b

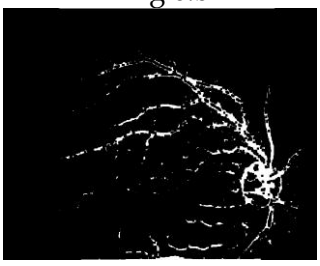

Fig 6.c

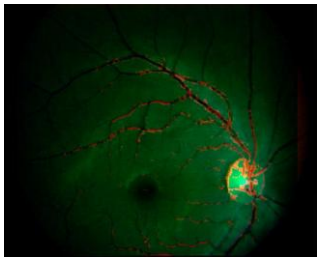

Fig 6.d

Fig 6: The partial segmented image and the bifurcation points as shown in the fourth image

The method applied to sample retinal images is as follows:

Step 1: First the texture is extracted from the retina which gives the shape of the arteries and veins

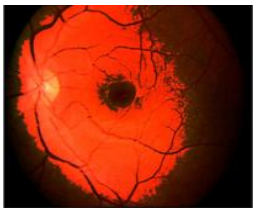

Fig 7.a

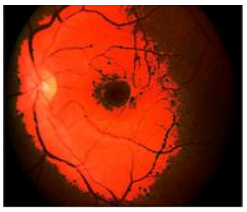

Fig 7.b

Fig 7.c

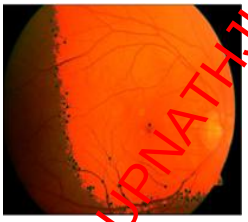

Fig 7.d

Fig 7: Texture of retinal images

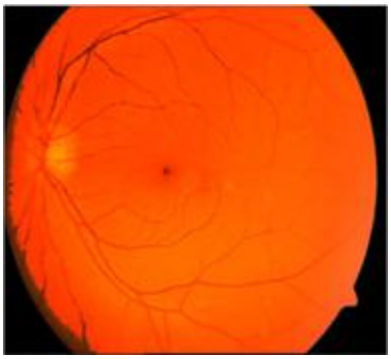

Fig 8.a

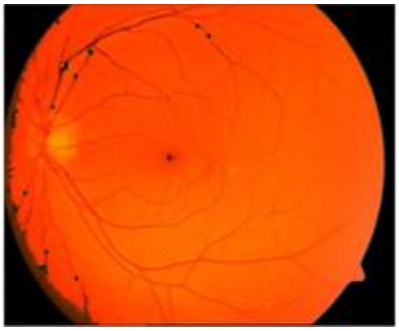

Fig 8.b

Fig 8: Some fundus images with set of crossover points.

The above images show the textures and in addition to step 1, we find the required crosspoints by applying Gabor Filter.

To extract the cross points, the Gabor Matrix is convolved with the texture of different sets of retina.

Now applying this matrix for different sets of frequencies we get,

f=255.

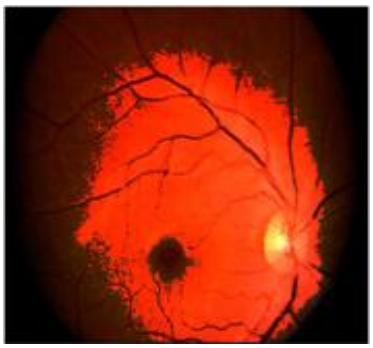

Fig 9.a

Fig 9.b

Fig 9: (a)Texture of image (b)crosspoints of image for f=255

f=90

Fig 10.a

Fig 10.b

Fig 10: (a)Texture of image (b)crosspoints of image for f=90

f=127

Fig 11.a

Fig 11.b

Fig 11: (a)Texture of image (b)crosspoints of image for f=127

f=190.

Fig 12.a

Fig 12.b

Fig 12: (a)Texture of image (b)crosspoints of image for f=90

Step 2: To extract the cross points the Shape Vector is convolved with the image. Here we look for 'Y' shape or 'X' shape.

3. RESULT AND ANALYSIS

In this paper we have developed a novel approach for extracting Cross points for different sets of frequencies which gives a better confirmation of results of a single retina of one person. The logical conclusion of this paper is that

a) The method works fine for dull images

b) The only disadvantage of this method is that we get false points also

4. CONCLUSION

One can use gabor filter method can be used to extract the features of retina. From the above images we conclude higher the threshold, lesser intensity areas are grabbed and lesser the threshold, higher threshold areas are grabbed. We also see that different sets of feature points are gathered for different sets of frequencies.

5. FUTURE WORK

In future, work can be done in the area of number of features for diabetes and also thought can be given to find the diameter of the vessels or the optical ball or the fovea. The major problem for extracting the optical ball and the fovea is that the region of interest for the optical ball falls with the vessels and that for the fovea is that in the gray scale image the intensity values becomes equal to the intensity values for pixels of the vessels.

REFERENCES

1. Characterization of changes in the blood vessels width and tortuosity in retinopathy of prematurity using image analysis, Connor Heneghan, John Flynn, Michael O'Keefe, Mark Cahill, Medical Image Analysis 6 (2002) 407-429.
2. A computer method of understanding Ocular Fundus images, Koichiro Akita and Hidlki Kt GA, Pattern recognition Vol 15, No 6, PP431 443 1982
3. X. Wang, H. Cao, and J. Zhang, Analysis of retinal images associated with hypertension and diabetes, *Proceedings of the IEEE* (2005).
4. C. Heneghan, J. Flynn, M. O'Keefe, and M. Cahill, Characterization of changes in the blood vessels width and tortuosity in retinopathy of prematurity using image analysis. *Medical Image Analysis* 407 (2002).
5. Biometric Iris recognition system using a fast and robust iris localization and alignment procedure, Balaji Ganeshan, Dhananjay Theckedath, Rupert Young, Chris Chatwin, Optics and Lasers in Engineering 44(2006)1-24.
6. Computer based detection of diabetes retinopathy stages using digital fundus images,UR Acharya,et al,Journal of Engg in Medicine,Vol 223.
7. Selected Pigmented Fundus Lesions of Children, Forest Daryel Ellis, MD, August 2005, Journal of AAPOS.
8. Retinal Arterial Wall Plagues in Susac Syndrome, Robert A. Egan, MD, Thuy Ha Nguyen, MD, J. Donald M. Gass, MD, Joseph F. Rrzzo III, MD, John Tivnan, OD, and John O. Susac, MD, 2003 by Elsevier Science Inc.
9. Effect of Axial Length on Retinal

Vascular Network Geometry, Niall Patton, Mrcophth, Rishma Maini, Bsc, Tom Macgillivary, PhD, and Baljean Dhillon, Frcophth, 2005 by Elsevier Inc.

10. Application of data envelops analysis in bench marking Christian N. Madu and Chu-Hua Kuei, International Journal of Quality Science, Vol. 3 No. 4, 1998, pp. 320-327, MCB University Press, 1359-8538.
11. A Combined Method to Detect Fundus features, V. Bevilacqua S. Cambò L. Cariello G. Mastronardi, IEEE Transactions.

Survey of the Multisensor Image Fusion Algorithms

Shalini.N
3rd Sem, Mtech, Dept.of CSE
The Oxford College of Engineering
shalu04.n@gmail.com.

Ms.Varalatchoumy.M
Asst.Prof, Dept.of CSE
The Oxford College of Engineering
kvl186@gmail.com.

ABSTRACT

Image fusion is the process of combining images taken from different sources, to obtain better situational awareness. The objective is to combine the most relevant information from source images into composite image. In the output image there should not be any introduction of artifacts or inconsistencies which will distract human observers or the further processing. There are many image fusion techniques based on signal, pixel, feature and symbol level fusion. The usefulness of the method has been done in various image pairs like multi-focus images, multi-sensor satellite image and medical images of cross-section of human brain. This paper analyses the various image fusion algorithms like the simple image fusion attempts, the pyramid decomposition image fusion, and the basic wavelet transform based image fusion like discrete wavelet transform and Haar wavelet transform. The Pareto optimization method proves that the quality produced by the Haar wavelet is better than other algorithms. Haar wavelet thus produces better results by the proposed gradient and smoothness criterion.

Keywords

Discrete Wavelet Transform, Haar Wavelet, Image fusion,Pareto optimization,Pyramid method.

1. INTRODUCTION

Information makes sense if it is able to convey its contents. Information can be recorded as signs, or transmitted as signals. The quality of the information is very important. Image fusion is the technique used to improve the quality of the information from the set of images.

1.1 Image fusion Definition

Image fusion is the process of combining information from two or more images of a scene into a single composite image. It should be more informative and is more suitable for visual perception or computer processing. Data fusion is a process of dealing with data and information from multiple sources to achieve refined/improved information for decision making. In data fusion the information of a specific scene acquired by two or more sensors at the same time or separate times is combined to generate an interpretation of the scene not obtainable from a single sensor.

Image fusion, a component of data fusion is an effective way for optimum utilization of large volumes of image from multiple sources. Multiple image fusion seeks to combine information from multiple sources to achieve inferences that are not feasible from a single sensor or source. It is the aim of image fusion to integrate different data in order to obtain more information than can be derived from each of the single sensor data alone [1].

1.2 Why Image fusion?

The fusion of images is often required for images acquired from different instrument modalities or for the same scene captured in different ways (like multi-sensor, multi-focus and multi-modal images). Multifocus image fusion is the process of combining information of two or more images of a same scene to result in all scene areas are in focus. When one scene contains objects in different distance, the camera can be focused on each object one after the other, creating set of pictures. Then using image fusion technique, an image with better focus across all area can be generated.

Medical image fusion has become a common term used in medical diagnostics and treatment. The term is used when multiple patient images are registered and merged to provide additional information. Fused images may be created from multiple images from the same imaging modality, or by combining information from multiple modalities, such as magnetic resonance image (MRI), computed tomography (CT). In radiology and radiation oncology, these images serve different purposes. Advantages of Image Fusion are clear with the following Fig.1 where the image fusion mechanism improves the reliability by the redundant information and also improves the capability by complementary information.

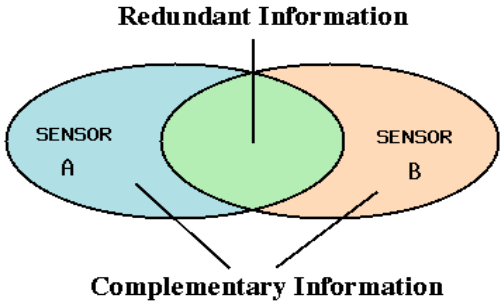

Fig. 1 Advantages of image fusion.

2. GENERIC REQUIREMENTS

The perception of the fused image is of paramount importance. When evaluating different fusion schemes some generic requirements can be imposed on the fusion result. The fused image should preserve as closely as possible all

relevant information contained in the input images [1]. The fusion process should not introduce any artifacts which can distract or mislead the human observer. In the fused image irrelevant features and noise should be suppressed to a maximum extent.

The first step toward fusion, which may be interpreted as a preprocessing step is the registration which brings down the constituting images to a common coordinate system. This step is important as fusion of images is meaningful only when common objects in images have identical geometric configuration with respect to size, location and orientation in all the images [2]. In the next step, the images are combined to form a single fused image through a judicious selection of proportions of different features from different images.

3. IMAGE FUSION ALGORITHMS

The most important issue concerning image fusion is to determine how to combine the sensor images. In recent years, several image fusion techniques have been proposed. The image fusion algorithm from the research is put into three categories as given in the Fig 2. In this section, these three categories are discussed with their limitations and their performances are compared based on simple metrics. The pair of medical images considered for evaluation of image fusion are CT scan image and MRI scan image.

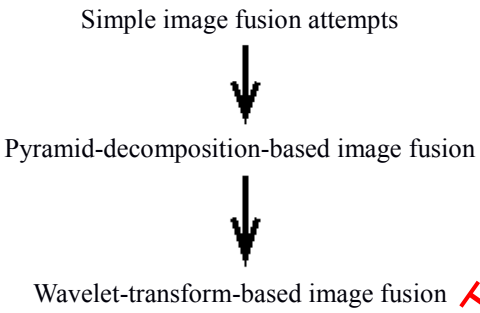

Fig. 2 Evaluation of Image Fusion.

3.1 Simple fusion algorithms

The simple fusion methods perform the fusion on the source images. This method uses the basic operations like addition, subtraction of the pixel intensities of the input images to be fused.

The simple fusion methods are:

- Averaging Method
- Select Maximum/Select Minimum

3.1.1 Averaging Method

This method developed by Burt and Kolczynski [3] uses a normalized correlation between the two images. The resultant coefficient for reconstruction is calculated from weighted average of the two images coefficients that means averaging of every corresponding pixel of input image to get output image. Fig.3 shows the multi spectral images, which are used as input images for the fusion algorithms.

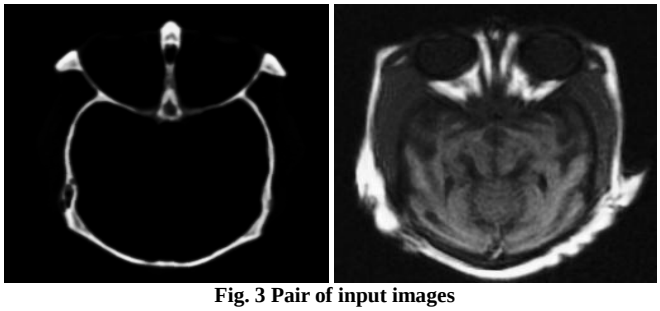

Fig. 3 Pair of input images

3.1.2 Select Maximum/Minimum Methods

This simple scheme just picks the coefficient in each sub-band with the largest magnitude, that is, for every corresponding pixel in the input images the maximum or minimum intensity is selected [4].Fig.4 shows the output images which is fused based on the average and maximum methods.

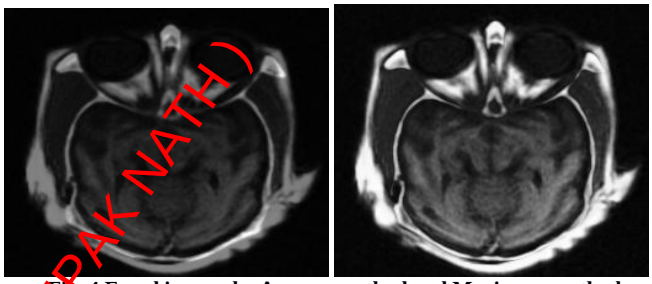

Fig. 4 Fused images by Average method and Maximum method

The output images in Fig. 4 depicts that simple fusion method produces unsatisfactory results. When this direct method is applied, the contrast of feature uniquely presented in either of the images is reduced. This method is good only when the input images have a high brightness and high contrast. To solve this problem, several Pyramid decomposition based image fusion is proposed.

3.2 Pyramid decomposition fusion method

An image pyramid can be described as a collection of low or band pass copies of an original image in which both band limit and sample density are reduced in regular steps. An image pyramid is constructed for each of the input image, and then pyramid is formed for the composite image by selecting coefficients from the input image pyramids. Finally, the fused image is obtained by taking inverse pyramid transform.

Several types of pyramid decomposition based methods developed for image fusion are:

- Laplacian Pyramid
- Ratio-of-low-pass Pyramid
- Gradient Pyramid
- Filter-Subtract-decimate (FSD)
- Morphological Pyramid

Pair of medical images given in Fig. 5 is considered as input for all types of pyramid decomposition method which is mentioned above.

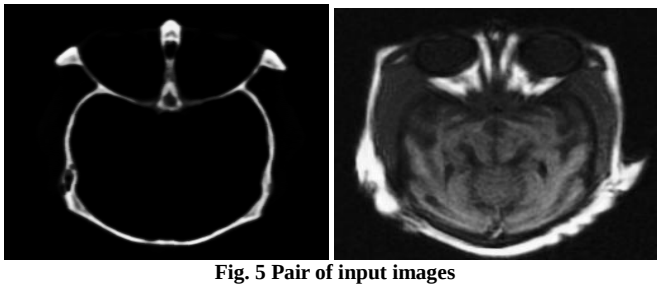

Fig. 5 Pair of input images

3.2.1 Laplacian Pyramid

Burt and Kolczynski [3] introduced the Laplacian algorithm. The lowest level of the pyramid has the same scale as the original image and contains the highest resolution information. A strength measure (sum area, max, min) is used to decide from which source what pixels contribute at each specific sample location. Higher levels of the pyramid are reduced resolution and increased scale versions of the original image.

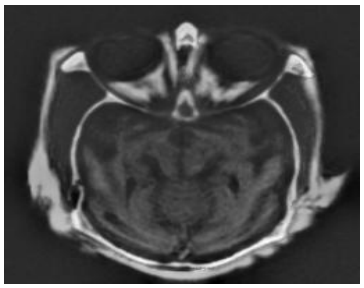

Fig. 6 Fused image by Laplacian pyramid method

The output image in Fig. 6 based on Laplacian pyramid based fusion has the following drawback. Often the fused images contain the blocking artifacts in region where it is going to fuse.

3.2.2 Ratio-of-low-pass Pyramid

Ratio of Low Pass Pyramid [7] is another pyramid in which at every level the image is the ratio of two successive levels of the Gaussian pyramid. In this case the fusion rule is to select at each pixel location i, j at the pyramid level L the pixel value from the largest deviation from unity from source images.

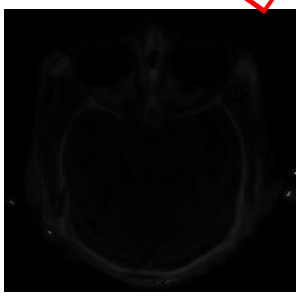

Fig. 7 Fused image by Ratio pyramid method

The output image in Fig.7 based on ratio-of low-pass method has a major drawback where it does not contribute to the sharpness of an image.

3.2.3 Gradient pyramid

Gradient pyramid of an image is obtained by applying gradient operators to every level of its Gaussian pyramid G. The gradient operators are used in the horizontal, vertical, and 2 diagonal directions.

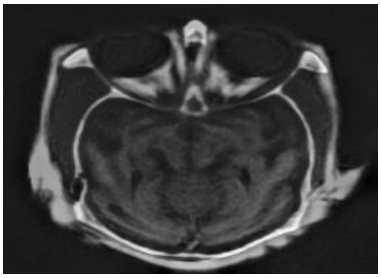

Fig.8 Fused image by Gradient method

Fig. 8 shows the fused output image which is obtained based on Gradient pyramid algorithm. This method considers low pass filters for the decomposition so, results in low quality.

3.2.4 Filter-Subtract-decimate (FSD)

This is similar to Laplacian fusion, the difference being in using FSD pyramid instead of Laplacian Pyramids. FSD Pyramid technique is a more computationally efficient variation of the Gaussian Pyramid.

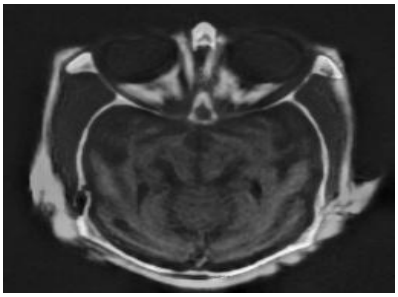

Fig.9 Fused image by FSD method

Fig.9 shows the fused image which is obtained by the FSD algorithm. This method decimates the input image matrices by neglecting every alternate row and column.

3.2.5 Morphological Pyramid

This method typically uses low or band pass filters as part of the process. The filtering operations usually alter the details of shape and the exact location of the objects in the image. This problem has been addressed by using morphological filters to remove the image details without adverse effects. Morphological filters are composed of a number of elementary transformations: closing and opening transformations [10].

The opening operator can be expressed as a composition of two other operators: erosion followed by dilation, both by the same input structural element. The main mechanism under the erosion operator is the local comparison of a shape, called structural element. Structuring element is a matrix used to define a neighborhood shape and size for morphological

operations, including dilation and erosion. It consists of only 0's and 1's and can have an arbitrary shape and size.

Fig. 10 Fused image by Morphological Pyramid method

The Fig. 10 shows the output image which is obtained based on the Morphological pyramid. These algorithms differ in the way the decomposition and recomposition take place. A better fusion results has been achieved by wavelet transform.

3.3 Wavelet transform based image fusion

Transform of a signal is just another form of representing the signal. Mathematical transform are applied to signal to obtain further information which is not present in raw signal. Fourier Transform of a time domain signal gives frequency domain representation. Limitation of Fourier transform are when it is in time domain it will not give information regarding frequency and when it is in frequency domain it will not provide information regarding time. The ultimate solution is the wavelet transform which provides time frequency representation simultaneously. It provides variable resolution such as at high frequency wavelet transform gives good time resolution and poor frequency resolution and at low frequency wavelet transform gives good frequency resolution and poor time resolution. Discrete Wavelet family includes Haar Wavelet, Daubechies Wavelet are discussed here.

3.3.1 Daubechies wavelets

The Daubechies wavelets are a family of orthogonal wavelets defining a discrete wavelet transform. It is characterized by a maximal number of vanishing moments for some given support. With each wavelet type of this class, there is a scaling function (also called father wavelet) [6] which generates an orthogonal multiresolution analysis. A pair of medical images given in the Fig. 11 is considered as input for the fusion by the Daubechies wavelet based algorithms.

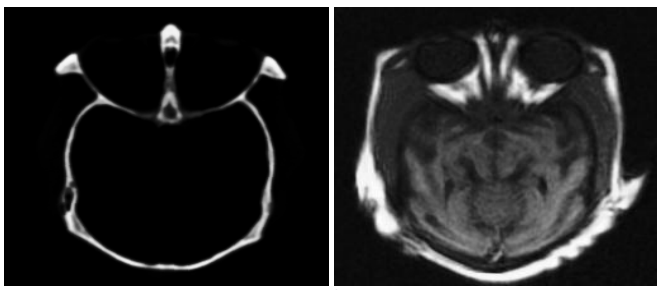

Fig. 11 Pair of input images

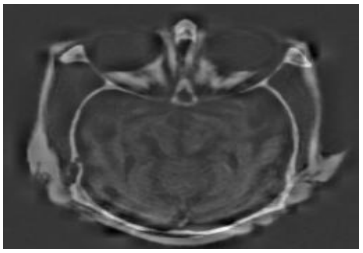

Fig.12 Fused image by Daubechies wavelet

Fig. 12 shows the output image which is obtained by the Daubechies wavelets method. In general the Daubechies wavelets are chosen to have the highest number of vanishing moments so this does not imply the best smoothness.

3.3.2 Discrete wavelet transforms

A common wavelet analysis technique used for fusion is the discrete wavelet transform (DWT) [6] [8] [9].In 2D image, a single level decomposition can be performed resulting in four different frequency bands namely LL, LH, HL and HH sub band and an N level decomposition can be performed resulting in 3N+1 different frequency bands as it is shown in Fig 13. At each level of decomposition, the image is split into high frequency and low frequency components. The low frequency components can be further decomposed until the desired resolution is reached.

In practice when wavelet decomposition is used for image fusion, one level of decomposition can be sufficient, but this depends on the ratio of the spatial resolutions of the images being fused. The conventional DWT can be applied using either a decimated or an un-decimated algorithm. In the decimated algorithm, the signal is down sampled after each level of transformation. In the case of a two-dimensional image, down-sampling is performed by keeping one out of every two rows and columns, making the transformed image one quarter of the original size and half the original resolution. The decimated algorithm can therefore be represented visually as a pyramid, where the spatial resolution becomes coarser as the image becomes smaller. The decimated algorithm is not shift-invariant, which means that it is sensitive to shifts of the input image. The decimation process also has a negative impact on the linear continuity of spatial features that do not have a horizontal or vertical orientation. These two factors tend to introduce artifacts when the algorithm is used in applications such as image fusion.

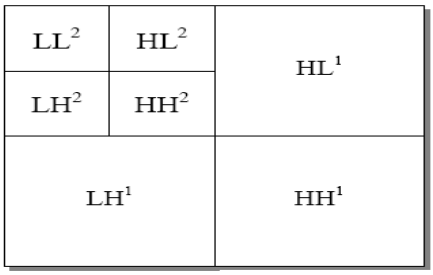

Fig.13 The Decomposition levels.

3.3.3 Haar wavelet

Haar wavelet is a sequence of rescaled "square-shaped" functions which together form a wavelet family or basis as shown in Fig 14. There are a wide variety of popular wavelet algorithms, including Daubechies wavelets, have the disadvantage of being more expensive to calculate than the Haar wavelets. The higher resolution provided by other wavelets is not worth the cost for financial time series, which are characterized by jagged transitions.

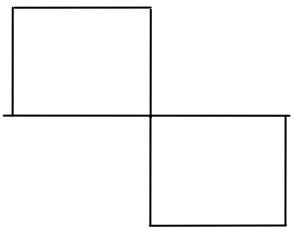

Fig. 14 Haar wavelet

The Haar wavelet's function can be described as

$$\Psi(t) = \begin{cases} 1 & 0 \le t \le ½, \\ 1 & ½ \le t \le 1, \\ 0 & \text{otherwise} \end{cases}$$

Its scaling function can be described as

$$\Phi(t) = \begin{cases} 1 & 0 \le t \le ½, \\ 0 & \text{otherwise} \end{cases}$$

Using the discrete wavelet transform, any sequence of even length can be transformed into a sequence of two-component-vectors. Each vector right-multiplies with the matrix, gets the result of one stage of the fast Haar-wavelet transform. The sequences s and d is usually separated and continues with transforming the sequence s. Sequence s is often referred to as the averages part, whereas d is known as the details part. If a sequence of length is a multiple of four, then blocks of 4 elements can be built. Transform these blocks in a similar manner with the 4×4 Haar matrix which combines two stages of the fast Haar-wavelet transform.

$$H_4 = \begin{bmatrix} 1 & 1 & 1 & 1 \\ 1 & 1 & -1 & -1 \\ 1 & -1 & 0 & 0 \\ 0 & 0 & 1 & -1 \end{bmatrix},$$

The Haar transform is the simplest of other wavelet transforms. This transform cross-multiplies a function against the Haar wavelet with various shifts and stretches. The Haar transform is derived from the Haar matrix. An example of a 4x4 Haar transformation matrix is shown as

$$H_4 = \frac{1}{\sqrt{4}} \begin{bmatrix} 1 & 1 & 1 & 1 \\ 1 & 1 & -1 & -1 \\ \sqrt{2} & -\sqrt{2} & 0 & 0 \\ 0 & 0 & \sqrt{2} & -\sqrt{2} \end{bmatrix}$$

Fig.15 shows the pair of input images used by the Haar wavelet algorithm.

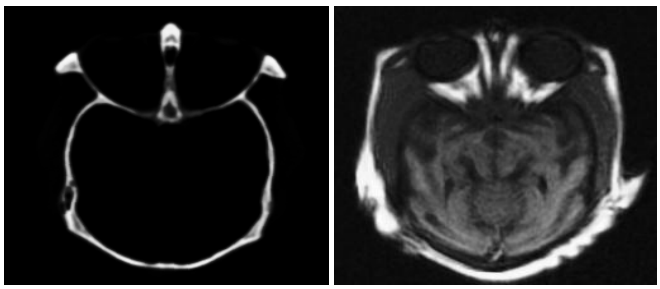

Fig. 15 Pair of input image for Haar wavelet

Fig. 16 Fused image by Haar wavelet

Fig. 16 shows the output image which is produced by Haar method. The Haar wavelet transform has a number of advantages compared to other algorithms.

- It is conceptually simple.
- It is fast.
- It is memory efficient, since it can be calculated in place without a temporary array.
- It is exactly reversible without the edge effects that are a problem with other wavelet transforms.
- The Haar transform is the simplest orthogonal wavelet transform. It is computed by iterating difference and averaging between odd and even samples of the signal. 2-D images needs to compute the average and difference in the horizontal and then in the vertical direction.

Shivsubramani, K P Soman [5] used simple metrics for the comparison of fusion algorithms. The simple metrics are, Mean Squared Error(MSE), Peak Signal to Noise Ratio (PSNR), Average difference(AD), Structural content(SC), Normalized Cross Correlation(NCC), Maximum Difference(MD). These metrics used to assess the best fusion algorithms in terms of quality using Pareto optimality method, which is a commonly used tool in multi optimization

when the different metrics cannot be compared. Table 1.1 gives the information about the image quality metrics which is used by all the image fusion algorithms to validate the results based on the image metrics readings.

Table 1.1 Image metrics for a pair of medical images

Algorithm	MSE	PSNR	AD	SC	NCC	MD
Average	177.28	25.62	-9.57	0.85	1.08	82
Maximum	116.5	27.47	-1.22	0.98	1.01	22
FSD	157.12	26.17	-10. 4	0.09	1.08	96
Laplacian pyramid	305.43	23.28	-16.47	0.08	1.1	92
Gradient Pyramid	146.26	26.48	-9.57	0.86	1.07	74
Ratio-of-low-pass Pyramid	166.11	25.93	-0.58	1	1	56
Morpholo-gical pyramid	1855.1	15.45	-39.29	0.64	1.23	104
Daubechies wavelet	351.2	22.58	-17.07	0.82	1.1	66
Haar wavelet	244.79	24.24	-14.39	0.83	1.09	84

The results are verified based on the image quality metrics. Ten respondents were selected in random and asked to select image they visually understood to be the best quality. It was found that out of the 30 assessments, The Haar based fusion is 63.33% best. The assessment saw that the fused images produced by Morphological pyramid method were rated most low in quality, so it becomes dominated algorithm. Haar wavelet is used for ease of implementation. It produces the output without the loss of generality and to work on any specific types of images. In Haar wavelet the fusion can be done based on proposed gradient and smoothness criterion ensures that the area of uniform intensity is incorporated in the fused images thus the effect of noise is minimized.

4. CONCLUSION

This paper analyses the various image fusion algorithms. The most important issue concerning image fusion is to determine how to combine the sensor images. In recent years, several image fusion techniques have been proposed. The simple fusion schemes perform the fusion right on the source images. One of the simplest of these image fusion methods just takes the pixel-by-pixel gray level average of the source images. This simplistic approach often has serious side effects such as reducing the contrast. With the introduction of pyramid transform some more sophisticated approaches began to emerge. It was found that better results were obtained if the fusion was performed in the transform domain. Several types of pyramid decomposition or multi-scale transform are developed for image fusion but the way the decomposition and recomposition phases differ in each of pyramid algorithms. The multi-scale wavelet decomposition has begun to take the place of pyramid decomposition for image fusion. It retains most of the advantages for image fusion but has much more complete theoretical support. The Haar wavelet which performs the fusion under the proposed gradient and smoothness criterion achieves the best results than other algorithms. Because of its efficient performance Haar wavelet can be considered to be the best method to be used for the fusion of CT and MRI images. The level of information obtained in the fused images using Haar wavelet transform can be highly beneficial in medical field.

REFERENCES

[1] Yufeng Zheng, IMAGE FUSION AND ITS APPLICATIONS, 2011, ch.1, pp. 1-2.

[2] Lisa Gottesfeld Brown, “Survey of image registration technique”, NY 10027, Columbia University New York, 1992 ,ch.2, pp 10-13.

[3] P.J. Burt, R.J. Kolczynski, “Enhanced image capture through fusion”, Proceedings of the 4th International Conference on Computer Vision, pp. 173–182, 1993.

[4] H. Li, B.S. Manjunath, S.K. Mitra, “Multisensor image fusion using the wavelet transform”, GMIP: Graphical Models Image Process, 1995, pp.235-245.

[5] K.P. Soman, Shivasubramani Krishnamoorthy, “Implementation and comparative study of image fusion algorithm”, proceedings of International Journal Of Computer Applications,2010, pp.25-35.

[6] Eduardo Fernández Canga, “Image fusion signal & image processing group”,Department of electronic & electrical Engineering June 2002 pp.1-7.

[7] Firooz Sadjadi, Lockheed Martin Corporation, “Comparative Image Fusion Analysais”,2010.

[8] Paul Hill, Nishan Canagarajah and Dave Bull, “Image Fusion using Complex Wavelets” ,Dept. of Electrical and Electronic Engineering the University of Bristol , BS5, UK, 2002.

[9] M. Sifuzzaman1, M.R. Islam1 and M.Z. Ali, “Application of Wavelet Transform and its Advantages Compared to Fourier Transform”, Journal of Physical Sciences, Vol. 13, 2009, pp.121-134.

[10] Luc Vincent, “Morphological Area Openings and Closings for Greyscale Images”, NATO Shape in Picture Workshop, Driebergen, Springer-Verlag, pp. 197-208, September 1992.

A survey on various computationally intensive parallel applications in High performance Computing System with OpenCL-MPI

Tushar Mungle
Govardhan Hegde
Srikanth Prabhu
N.GopalaKrishna Kini

Department of Computer Science and Engineering
Manipal Institute of Technology, Manipal

tushar_mungle@yahoo.co.in govardhan.hegde@manipal.edu Srikanth_prabhu@yahoo.com ng.kini@manipal.edu

Abstract -As we are in the development phase of our own super computer, we have identified several applications which are highly computationally intensive applications for a normal desktop computer to achieve the solution. These identified applications are related to multidisciplinary like bio-medical, mathematics, fluid-dynamics, genetic algorithms. We are actually identifying the parallel computations involved in each application which are independent to each other and optimizing it to perform better in our design of supercomputer. We basically use clustered node approach in which one master node distributes the jobs to multiple client nodes after identifying parallel computations involved in the application which are independent to each other. The application uses massively computationally intensive huge data which are SIMD based. We have around 20 nodes with 2 GPUs per node to optimize the computation. We have developed a cluster with job scheduler code to distribute the task to multiple clients after identifying parallel computations which are independent. This paper gives us a great satisfaction in studying the concept of high-performance in various fields of computationally intensive applications. The main application we focussed on is retinal pattern matching using shape extractors using the fast computing method of extracting bifurcation points.

KEYWORDS: SIMD, Biometrics, Parallel computing, High Performance Computing.

1. INTRODUCTION

In the field of Forensic Science it has been very difficult to get a Biometric which is unique for any person in the sense that it doesn't change for the same person under any circumstances. Many of the Forensic scientists are concentrating on an area where they are sure of good results in terms of robustness, uniqueness, measure. There were many trials made on the concept of correlation between different biometrics. But since the human

brain has different set of neurons controlling the sensory organs, it is but very difficult to correlate the different biometrics [1]. So Forensic Science and Ophthalmology has made an attempt of finding a Biometric which finds unique features which are unique for a person. Cross points on the retina help to identify diseases and to get other vital information which relates to thermal imaging where in we see the blood flow in the arteries and veins of the retina [1][2]. In case of thermal imaging thresholding is applied to find exactly the mental state of the person at a particular instance of time. Diagrammatically anatomy and physiology of the retina looks like as shown in the figure.

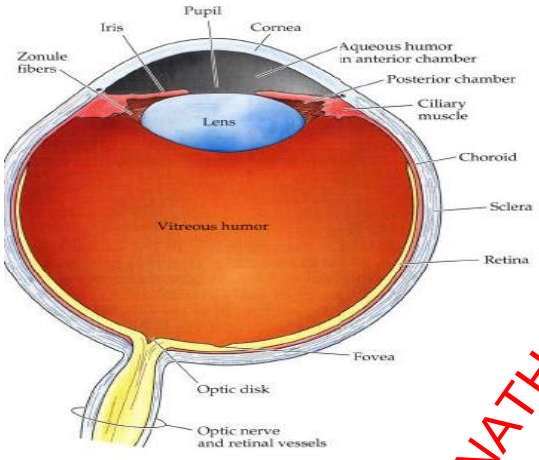

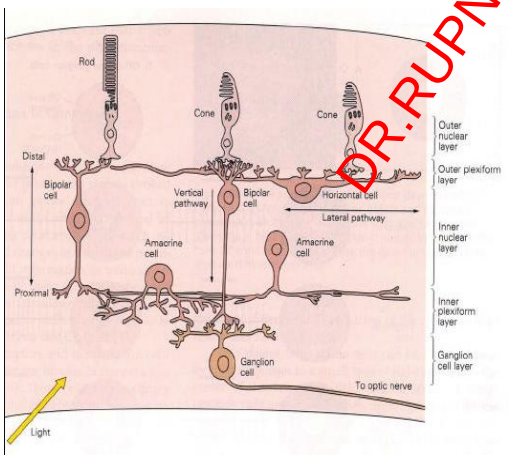

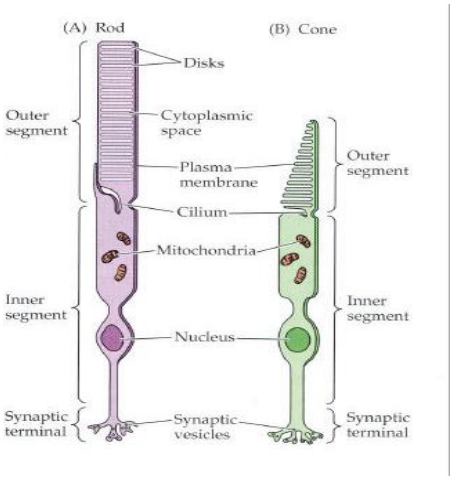

Fig 1: The above figure shows the rods and cones which lead to the formation of Bifurcation points.

This Biometric which is Retina which is located on the back side of the eye has unique points which are Bifurcation points or Crossover points. From the above diagrams, the medical conclusion is that rods and cones lead to the formation of cross points which are otherwise called Bifurcation points.

2. IMAGE PREPROCESSING

In this paper we concentrate on the boundaries of Retina using the Sobel filter. The normal retinal image(1.jpg) sample is shown below.

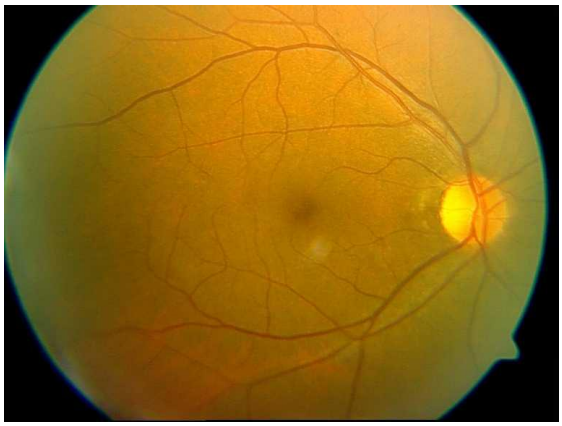

Different instances of edges of 1.jpg are as follows.

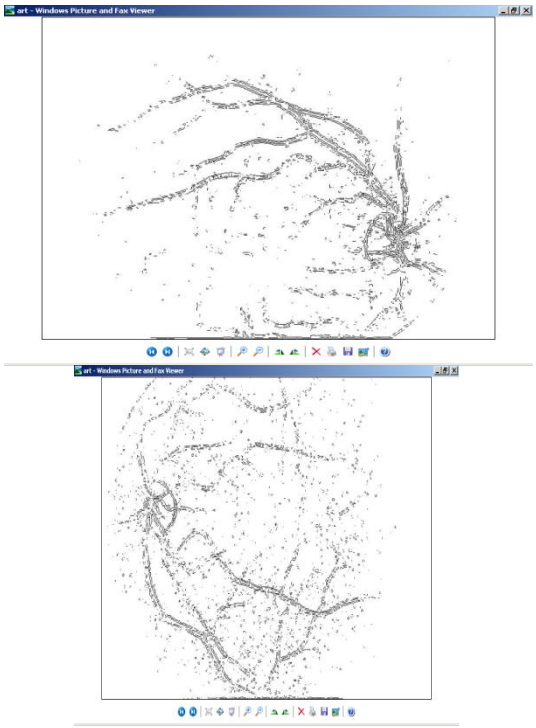

Fig 2: Shows the boundaries of retina.

The boundaries are found since it becomes easy to evaluate the cross over points from the grey level image, when the image is tracked from left to right.

3. BIFURCATION POINT EXTRACTION

The crosses over points on the retina are evaluated by moving a three by three matrix over the retina by applying the principle of convolution.

The matrix looks like:

1	0	1
0	1	0
0	1	0

In a retina shapes can take the following possibilities (along with one mentioned above):

1	1	1
0	1	0
1	0	1

These shapes are analyzed in a three by three neighbourhood [3].

In general if we have a matrix which has a representation

1	0	1
X	0	X
1	0	1

This kind of matrix helps to approximate the shapes of the objects in search to the above two shapes.

The above matrices helps in extracting the shapes of entities where in we can spot the crossover points.

Proceeding further with the above algorithm we have,

Step 1: Extract ‘Y’ or ‘H’ shape from the above retina.

So we have the following possibilities.

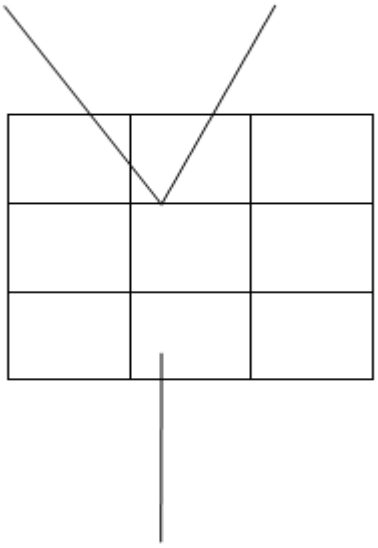

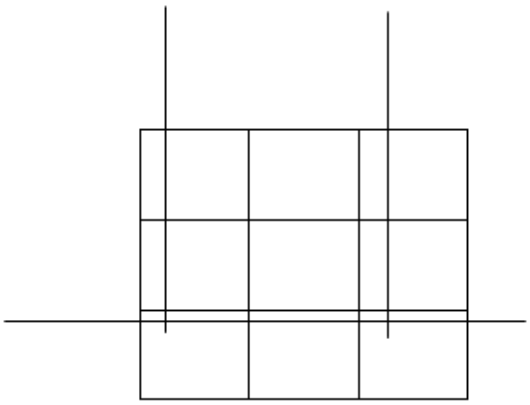

Fig 3: Shows the different shapes for Cross point extraction.

Here the blocks are marked by 00, 01, 02, 10, 11, 12, 20, 21, 22.

Step 2 : Once the shapes of the arteries and veins have been recognized in the above two categories, we mark the central pixel in the matrix which is 11.

The shapes belong to following categories.

Step 3 : The distances between these points is calculated by using the Euclidean Distance formula [6].

$$d(x,y) = \sum_{k} \sqrt{(x_i - x_j)^2 + (y_i - y_j)^2}$$

4. RESULTS AND ANALYSIS

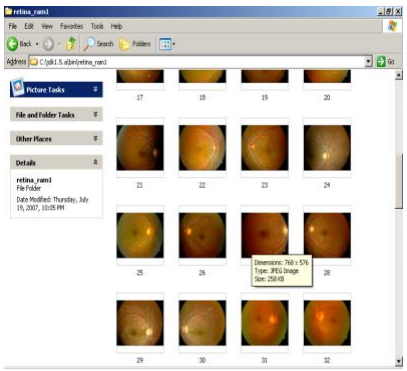

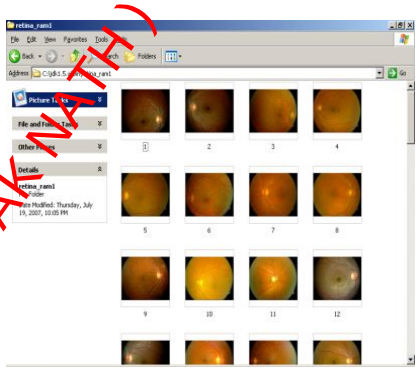

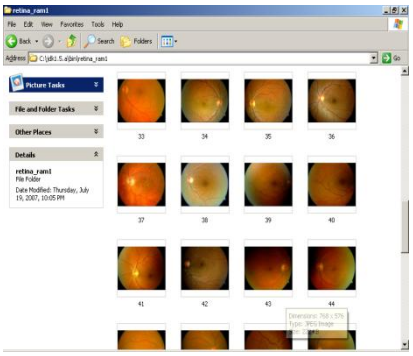

Fig 4: Shows the list of images (retina's)

The crosspoints for an image 1.jpg are

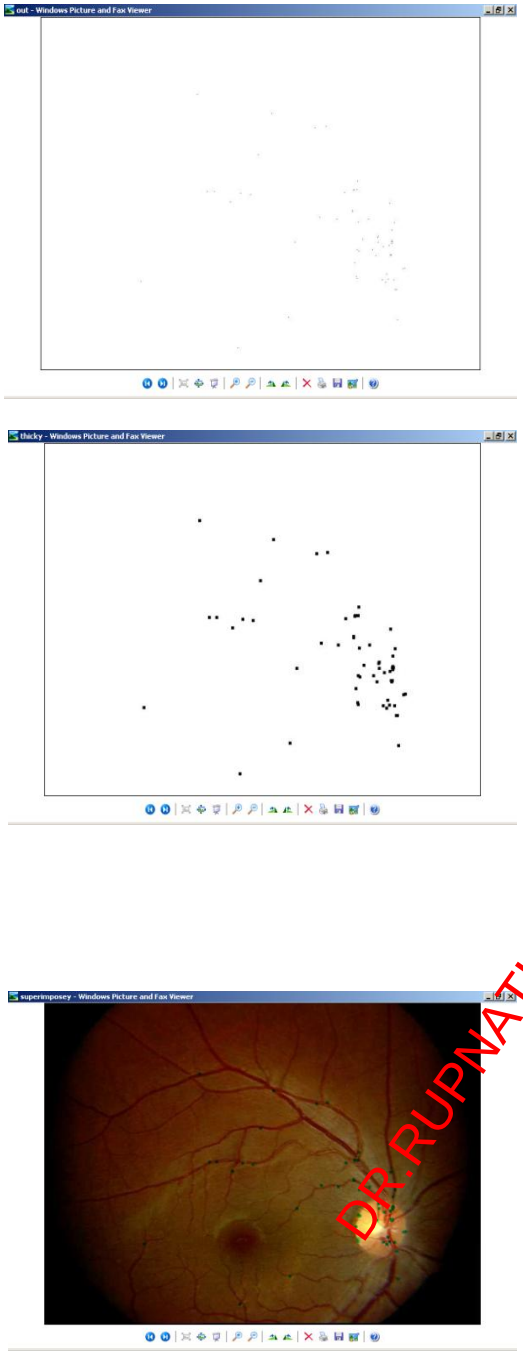

Fig 5: Shows the extraction of Cross points using Shape Extractor.

The above image shows the Bifurcation points or the cross points on the retina(1. jpg).

The real time images taken from Sir Ganga Ram hospital lack clarity due to the diverse set of patients this hospital gets.

By performing a comparative study with the paper by vb, etal, we come to a logical conclusion that our work is an innovative extension of this work since the crossover points are caught on real time images.

One such result from the above paper is shown below:

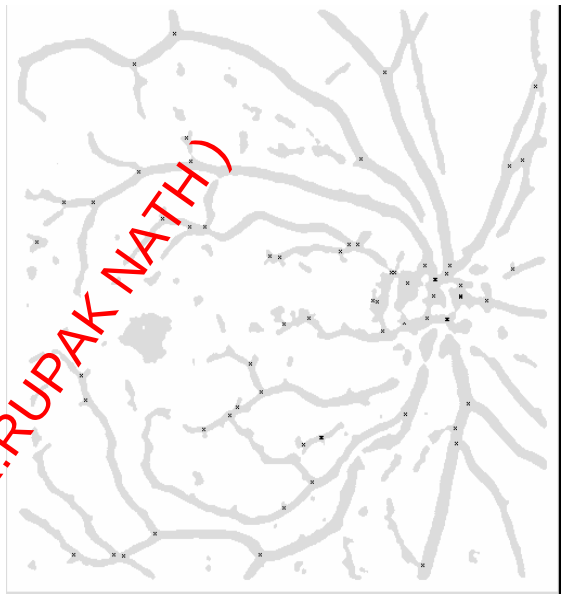

In general we have the following outputs.

The distances stored for all these images between the crossover points are as follows:

12345. 9876

16756. 8876

14567. 9876

13456. 87654

These distances are unique for any person.

Therefore comparing our results with the literature survey's we come to a conclusion that

a) Algorithm for Shape Extraction works very well for a large database for patients of various diversities, which is faster than sequential computing.

b) The distances between all the crossover points is also unique for any individual, which has helped the parallel computing.

c) Algorithm gives good results when the images are not clear in terms of matching. The only disadvantage of the algorithm is that it generates a set of false points, which are undesirable, which can be overcome by image registration.

5. FUTURE WORK

In future, work can be done in the area of number of features for diabetes and also thought can be given to find the diameter of the vessels or the optical ball or the fovea. The major problem for extracting the optical ball and the fovea is that the region of interest for the optical ball falls with the vessels and that for the fovea is that in the gray scale image the intensity values becomes equal to the intensity values for pixels of the vessels. But using color components these parameters can be improved and further work can be continued using Probabilistic Neural Network and also Fuzzy Neural Network.

REFERENCES

1. Characterization of changes in the blood vessels width and tortuosity in retinopathy of prematurity using image analysis, ConnorHeneghan, John Flynn, Michael O'Keefe, Mark Cahill, Medical Image Analysis 6 (2002) 407-429.
2. Biometric Iris recognition system using a fast and robust iris localization and alignment procedure, BalajiGaneshan, DhananjayTheckedath, Rupert Young, Chris Chatwin, Optics and Lasers in Engineering 44(2006)1-24.
3. A computer method of understanding Ocular Fundus images, Koichiro Akita and HidlkiKt GA, Pattern recognition Vol 15, No 6, PP431 443 1982
4. Selected Pigmented Fundus Lesions of Children, ForestDaryel Ellis, MD, August 2005, Journal of AAPOS.
5. Retinal Arterial Wall Plagues in Susac Syndrome, Robert A. Egan, MD, Thuy Ha Nguyen, MD, J. Donald M. Gass, MD, Joseph F. Rrzzo III, MD, John Tivnan, OD, and John O. Susac, MD, 2003 by Elsevier Science Inc.

6. Effect of Axial Length on Retinal Vascular Network Geometry, Niall Patton, Mrcophth, RishmaMaini, Bsc, Tom Macgillivary, PhD, and BaljeanDhillon, Frcophth, 2005 by Elsevier Inc.
7. Application of data envelops analysis in bench marking Christian N. Madu and Chu-HuaKuei, International Journal of Quality Science, Vol. 3 No. 4, 1998, pp. 320-327, MCB University Press, 1359-8538.
8. A Combined Method to Detect Fundus features, V. Bevilacqua S. Cambò L. Cariello G. Mastronardi, IEEE Transactions.

Design of Tilt Angle for Maximum Efficiency in Solar Water Heater – An Implementation using LabVIEW

Chanchal Naskar
Dept of Electrical Engineering
National Institute of Technology, Silchar
Silchar, India
c.naskar12@gmail.com

Santhosh K V
Dept of Electrical Engineering
National Institute of Technology, Silchar
Silchar, India
kv.santhu@gmail.com

***Abstract* — Solar energy is the abundant energy available everywhere at no cost. India is blessed with the tropical climate with a good percentage of solar energy. Solar water heater is one of the household appliances used in most of the Indian houses. A system is proposed in this paper which studies the effect of tilt angle of collectors on the efficiency of water heater. The objective of the proposed work are to calculate the solar noon based on the location, and from the computation of solar noon the tilt angle of the collector is calculated to achieve maximum efficiency. The proposed technique was subjected to several type of solar water heater and the system produced desired outputs**

Keywords- Solar heater, Solar noon, LabVIEW

I. INTRODUCTION

Solar energy is the energy derived from the sun through the form of solar radiation. Solar powered electrical generation relies on photovoltaic's and heat engines. A partial list of other solar applications includes space heating and cooling through solar architecture, day lighting, and solar hot water, solar cooking, and high temperature process heat for industrial purposes. Solar technologies are broadly characterized as either passive solar or active solar depending on the way they capture, convert and distribute solar energy. Active solar techniques include the use of photovoltaic panels and solar thermal collectors to harness the energy. Passive solar techniques include orienting a building to the Sun, selecting materials with favorable thermal mass or light dispersing properties, and designing spaces that naturally circulate air. The solar radiation incident on the surface of the earth can be conveniently utilized for the benefit of human society. One of the popular devices that harness the solar energy is solar hot water system (SHWS). A solar water heater consists of a collector to collect solar energy and an insulated storage tank to store hot water. The solar energy incident on the absorber panel coated with selected coating transfers the hat to the riser pipes underneath the absorber panel. The water passing through the risers get heated up and are delivered the storage tank. The re-circulation of the same water through absorber panel in the collector raises the temperature to 80˚C (Maximum) in a good sunny day. The total system with solar collector, storage tank and pipelines is called solar hot water system. Broadly, the solar water heating systems are of two categories. They are: closed loop system and open loop system. In the first one, heat exchangers are installed to protect the system from hard water obtained from borewells or from freezing temperatures in the cold regions. In the other type, either thermosyphon or forced circulation system, the water in the system is open to the atmosphere at one point or other. The thermosyphon systems are simple and relatively inexpensive. They are suitable for domestic and small institutional systems, provided the water is treated and potable in quality. The forced circulation systems employ electrical pumps to circulate the water through collectors and storage tanks. Based on the collector system, solar water heaters can be of two types [1-10].

We are blessed with Solar Energy in abundance at no cost. The solar radiation incident on the surface of the earth can be conveniently utilized for the benefit of human society. One of the popular devices that harness the solar energy is solar hot water system (SHWS). Electricity is expensive not available due to power cuts in many areas when required for heating water. Solar Water Heater, since it stores hot water in an insulated tank, provides water all the time when required. The aim & objective of this work is to provide basic information on the components, system efficiency and types of solar water heaters currently available and the economic and environmental benefits of owning a system. Beside that we are trying to provide some computer programs which are essential for calculating the efficiency. Also we are trying to focus the effect of tilt angel, aperture area and different storage capacity on the performance [1-10].

In [11], provides a grey-box modeling approach based on fuzzy system to predict the outlet water temperature of a solar water heating system is discussed. A computer simulation to predict the performance of solar domestic hot water systems is discussed in [12]. The economical benefits of utilizing solar water heating systems for low-income dwellings in Brazil have been analyzed in [13]. In [14], a new design of roof-integrated water solar collector by integrating the collector into roof. Its main concept is based on the use of water redistribution for changing the roof configuration. An alternative for a large solar thermal electric plants having steam Rankine Cycle is discussed in [15]. An experimental & numerical study of thermal stratification in a mantle tank has been carried out in [16].

The paper is organised as follows: after introduction in Section-I, a brief description of block diagram is given in Section-II. Section-III deals with the problem statement followed by proposed solution in Section-IV. Result and discussion is given in Section-V.

II. OBJECTIVES OF PROPOSED WORK

Objectives of the proposed work can be stated as

- To test the collector and find out the efficiency
- Provide the efficiency certificate to the manufacture
- Make some computer programming for efficiency calculation
- Discuss the effect of tank capacity, aperture area and tilt angle on the efficiency

III. EXPERIMENTAL SETUP

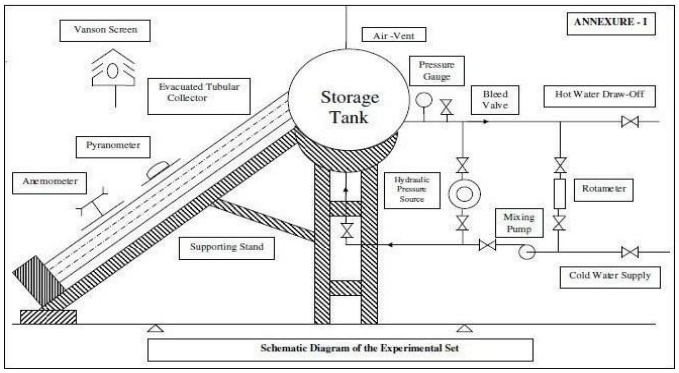

Figure. 1 Block diagram of proposed instrument

Figure 2. Picture of actual model

To find out the efficiency of solar water heating system we need a solar water heater whose efficiency is to be found. In India there are different manufacture companies present who made this type of water heater mainly Anu solar, Kirti solar etc. Mainly 100 liters and 200 liters capacity system are available in the market for domestic water heating. Evacuated tube collector is used in this type of system. The tube length is varies from 1500 mm to 1800 mm mainly. The inner diameter of the tube generally 47 mm and the outer diameter is 58 mm. The total numbers of tubes varies from 10 to 15 for 100 LPD (liter per day) systems. For 200 LPD systems it will be 30. The solar absorbance of the selective coating is greater than 0.86 and the solar emittance is less than 0.08. The components of solar water heating system are

(i) Solar collectors(ETC)
(ii) Insulated storage tank for storing hot water
(iii) Tank and collector stand along with other instrument

All physical measurements, such as, length, width, thickness, etc. shall be measured and reported in mm. Gross area of solar collector is defined as the total area on which solar radiation is falling (taking into account the gap, if any, between the tubes, and also the frame etc.). For flat plate solar collectors, it shall be calculated by multiplying width and length of the collector measured from outer edge to the outer edge. For the solar water heating models using all-glass ETCs, length shall be measured from bottom side of the storage tank to the outer edge of bottom tube holder while width shall be taken as equal to the length of the bottom tube holder. The measurement accuracy of the gross area shall be ± 0.1 %. The volume of the storage tank shall be measured to an accuracy of ± 1%.

Solar radiation shall be measured using a class-I Pyranometer on the plane of solar collector. For this, a mounting stand shall be used.

For measuring ambient air temperature, the measuring sensor (a calibrated RTD) shall be located shaded by a Stevenson screen in the vicinity of the test set-up (not more than 10 m from it. It shall be ensured that there is no obstruction by any structure or building to alter (block or enhance) the free flow of the natural wind to the sensor. The outside surface of the Stevenson screen shall be of light colour, preferably white, and its bottom shall be kept at least 1 m above the ground level.

The surrounding air speed shall be measured on the collector surface at about its middle every half an hour with an accuracy of ± 0.1 m/s and the average value of the day will be reported along with the test results.

IV. PROBLEM SOLUTION

A: SOLAR CONSTANT

The eccentricity of earth orbit is such that the distance between the sun and earth varies by 1.7%. The radiation emitted by the sun and its spatial relationship to the earth result in a nearly fixed intensity of solar radiation outside the earth atmospheres which is called as a solar constant (Gsc). Its value is 1367 w/m2 according to the World Radiation Center (WRC).

B: SOLAR RADIATION MEASUREMENT

Solar radiation flux is measured with the help of pyranometer, pyrheliometer and sunshine recorder. A pyranometer is used to measure solar irradiance on a planar surface. A pyranometer‟s main components are, A thermopile sensor with a black coating. This sensor absorbs all solar radiation, has a flat spectrum covering the 300 to 50,000 nanometer range, and has a near-perfect cosine response. A

glass dome. This dome limits the spectral response from 300 to 2,800 nanometers (cutting off the part above 2,800 nm), while preserving the 180 degrees field of view. Another function of the dome is that it shields the thermopile sensor from convection. The black coating on the thermopile sensor absorbs the solar radiation. This radiation is converted to heat. The heat flows through the sensor to the pyranometer housing. The thermopile sensor generates a voltage output signal that is proportional to the solar radiation.

Figure. 3. Pyranometer

C: RADIATION ON A SLOPE SURFACE

The diffuse radiation model is composed of three parts. The first is an isotropic part, received uniformly from the entire sky dome. The second is circumsolar diffuse, resulting from forward scattering of solar radiation and concentrated in the part of the sky around the sun. The third, referred to as horizon brightening, is concentrated neat the horizon and is most pronounced in clear skies. It is necessary to know or estimate the solar radiation incident on tilted surfaces such as solar collectors, windows, or other passive system receivers, The incident solar radiation is the sum of a set of radiation streams including beam radiation, the three components of diffuse radiation from the sky, and radiation reflected from the various surfaces seen by the tilted surface. The total incident radiation on this surface can be written as

$$IT = ITb + ITdiso + ITdcs + ITdhz + ITrefl \quad (1)$$

where the subscripts iso, cs, hz, and refl refer to the isoiropic, circumsolar, horizon, and reflected radiation streams. For a surface (a collector) of area Ac, the total incident radiation can be expressed in terms of the beam and diffuse radiation on the horizontal surface and the total radiation on the surfaces that reflect to the tilted surface. The new equation would be

$$ACIT = IbRbAC + Id,isoASFs\text{-}c + Id,csRbAC + Id,hzAhzFhz\text{-}c + \Sigma IiρiAiFi\text{-}c \quad (2)$$

The first term is the beam contribution. The second is the isotropic diffuse term, which includes the product of sky area *As* (an undefined area) and the radiation view factor from the sky to the collector Fs-c The third is the circumsolar diffuse, which is treated as coming from the same direction as the beam. The fourth term is the contribution of the diffuse from the horizon from a band with another undefined area *A*hz. The fifth term is the set of reflected radiation streams from the buildings, fields, and so on, to which the tilted surface is exposed. The symbol i refer to each of the reflected stream: Ii is the solar radiation incident on the ith surface. ρi is the diffuse reflectance of that surface and Fi-c is the view factor from the ith surface to the tilted surface. The equation can be rewritten in a useful form by interchanging areas and view factors (since the view factor reciprocity relation requires that ASFS-C = ACFC-S. This eliminates the undefined areas *As* and Ahz. The area *A*c appears in each term in the equation and cancels. So

$$I_T = I_bR_b + I_{d,iso}F_{c\text{-}s} + I_{d,cs}R_b + I_{d,hz}F_{c\text{-}hz} + I\rho_gF_{c\text{-}g} \quad (3)$$

This equation, with variations, is the basis for methods of calculating IT. When IT has been determined the ratio of total radiation on the tilted surface to that on the horizontal surface can be determined by

$$R = \frac{\text{total radiation on the titled surface}}{\text{total radiation on horizontal surface}} \quad (4)$$

D: THERMOSYPHON

Thermosyphon refers to a method of passive heat exchange based on natural convection, which circulates liquid without the necessity of a mechanical pump. This circulation can either be open-loop, as when liquid in a holding tank is passed in one direction via a heated transfer tube mounted at the bottom of the tank to a distribution point even one mounted above the originating tank or it can be a vertical closed-loop circuit with return to the original vessel. Its intended purpose is to simplify moving liquid and or heat transfer, by avoiding the cost and complexity of a conventional liquid pump.

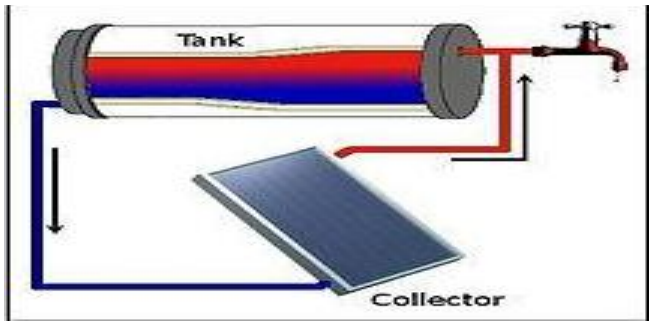

Figure 4. Thermosyphon

V. TEST SEQUENCE

Sequence	Test
1	Pre-conditioning Test
2	Static pressure Leakage Test
3	Thermal Performance Test (Daytime and nighttime tests shall be performed one after another to complete one data set)

The following energy balance equation would determine the thermal performance of the solar hot water system during the day-time:

$$\left[\begin{array}{l}\text{Rate of change in}\\ \text{energy contents of}\\ \text{the water in the}\\ \text{storage tank}\end{array}\right] = \left[\begin{array}{l}\text{Rate at which useful}\\ \text{energy is supplied to}\\ \text{water in the storage tank}\\ \text{by solar collector}\end{array}\right] - \left[\begin{array}{l}\text{Rate at which energy}\\ \text{is lost from water}\\ \text{in the storage tank}\\ \text{to the ambient air}\end{array}\right]$$

$$(MC)_s \frac{dT_s}{dt} = A_a F' [G_T (\tau\alpha)_{eff} - U_L (T_s - T_a)] - (A_s U_s + A_p U_p) (T_s - T_a)$$

Rearranging and integrating equation with respect to time, between the time period t1 to t2 during which the energy is collected, one gets

$$(MC)_s (T_{sfd} - T_{sid}) = A_a F' \int_{t_{1d}}^{t_{2d}} G_T (\alpha\tau)_{eff} . dt - (A_a F' U_L + A_s U_s + A_p U_p) \int_{t_{1d}}^{t_{2d}} (T_s - T_a) dt$$

The total energy incident on the collector during the time period from t1d to t2d is given by the following expression:

$$Q_c = A_c \int_{t_{1d}}^{t_{2d}} G_T dt$$

$$\eta_{sys} = \eta_{sys,o} - U_{sys,d} . X$$

Where

$$\eta_{sys} = \frac{(MC)_s (T_{sfd} - T_{sid})}{A_c \int_{t_{1d}}^{t_{2d}} G_T dt}$$

$$\eta_{sys,o} = \frac{A_a F' \int_{t_{1d}}^{t_{2d}} G_T (\alpha\tau)_{eff} . dt}{A_c \int_{t_{1d}}^{t_{2d}} G_T . dt}$$

$$U_{sys,d} = \frac{A_a F' U_L + A_s U_s + A_p U_p}{A_c}$$

$$X = \frac{\int_{t_{1d}}^{t_{2d}} (T_s - T_a) dt}{\int_{t_{1d}}^{t_{2d}} G_T dt}$$

The parameters sys,o and Usys,d are defined as the characteristic parameters of the thermosyphonic solar water heating systems.

Night time performance:

During night time, no solar radiation is received and also there is no flow of water through the solar collector. The heat is therefore lost primarily from the storage tank and part of the piping. In view of this, the equation (3) may be re-written as follows:

$$(MC)_s \int_{t_{1n}}^{t_{2n}} \frac{dT_s}{T_s - T_a} = - (A_s U_s + A_p' U_p) \int_{t_{1n}}^{t_{2n}} dt$$

or

$$(MC)_s \ln \left[\frac{T_{s,fn} - \overline{T}_{an}}{T_{s,in} - \overline{T}_{an}}\right] = U_{sys,n} A_c (t_{2n} - t_{1n})$$

Where $U_{sys,n} A_c = (A_s U_s + A_p' U_p)$

Cooling time constant to rate the performance of the solar water heating system during no-radiation period may be expressed by the following expression:

$$T_{cooling,n} = \frac{(MC)_s}{(U_{sys,n} A_c)}$$

Day time performance:

Solar collector is shaded completely with an opaque cover, white on the top exterior, at about 4 h before the solar noon. The storage tank of the solar water heating system is filled fully with water. The quantity of water filled in the storage tank only shall be taken as notional capacity of the solar water heating system.

The water in the storage tank is fully mixed by switching on pump for 5 minutes before beginning of the test at the designated time instant.

Initial value of the storage water temperature, Tsid is measured and recorded, and the shade-cover is removed at 3 h 30 min before the solar noon.

Measurements for ambient air temperature, water temperature of the storage tank, and solar irradiance on the plane of solar collector get commenced at the start of the test. The measurements are continued subsequently for the entire period of the test at an interval of one minute or less, however, recording of data is adequate at an interval of 10 minutes.

To end the day-test cycle, the solar collector is again shaded on expiry of 3 h 30 min from solar noontime. The water in the storage tank is again mixed by operating the pump for five minutes, and final storage water temperature (Tsfd) is measured and recorded.

The test is repeated for at least ten days with different values of initial storage water temperature. The first test shall be carried out with cold (supply) water in the storage tank. For subsequent days, initial water temperature shall be raised in uniform steps to cover up to 70ºC temperature (fully mixed storage).

Different initial temperature in the storage tank may be achieved by adding appropriate quantity of cold water to the previous day's heated water in the storage tank. Alternatively, hot water from any other source may also be used to achieve the required temperature of the water in the storage tank.

The minimum solar irradiance on the plane of solar collector, GT, during the period of day-test shall be 550 W/m2 and the ratio of minimum solar irradiance to maximum solar irradiance recorded during the day-test should not be less than 0.5. The data for the days for which these conditions are not specified, will not be used in the estimation of sys, o, and Usys, d.

Based on the measured data obtained during day-test and night-test, the characteristic parameters of the solar hot water system shall be evaluated as given subsequently**.**

Calculate system from the following expression using data recorded during the daytime test

$$\eta_{sys} = \frac{(MC)_s (T_{sfd} - T_{sid})}{A_c \int_{t_1}^{t_2} G_T \, dt}$$

$$X = \frac{\int_{t_{1d}}^{t_{2d}} (T_{sd} - T_{ad}) dt}{\int_{t_1}^{t_2} G_T dt} = \frac{\sum_{m=1}^{42} \left(\frac{(T_{sfm} + T_{sim})}{2} - \bar{T}_{adm} \right) \times (t_{2m} - t_{1m})_d}{\int_{t_1}^{t_2} G_T \, dt}$$

Where *T adm* represents average ambient temperature during the mth time interval; *Tsfm* and *Tsim* represents the average water temperature of the two RTD"s in the storage tank at the end and start of the mth time interval, respectively. Obviously, the value of (t2m -t1m)d in the above expression is equivalent to 10 minutes.

Plot a curve with values of sys on y-axis and those of X on x-axis. Draw a trend line using regression method of least squares of curve fitting, and obtain values of sys,o and Usys,d from the intercept of the trend line with y-axis and slope of the trend line respectively.

System efficiency corresponding to the following standard test conditions may be calculated

Average storage temperature = 50ºC Average ambient air temperature during test period = 25ºC Average of total solar radiation incident on the plane of = 700 W/m2 solar collectors

Amount of thermal energy stored in the storage tank during a period of seven hours corresponding to the standard test conditions in kWh may be calculated as follows.

Q = sys (corresponding to standard conditions) x Ac x 0.7 x 7

In order to calculate cooling time constant, a plot of **I**n (Tsm-Tam) versus time shall be plotted using measured data from the nighttime test. A trend line using regression method of least squares of curve fitting shall be plotted. The slope of the trend line shall give value for 1/cooling,n Using this value in equation (9), the value of Usys,n may be obtained.

LabVIEW Implementation:

To achieve the objectives mentioned in the above section LabVIEW software is programmed. The LabVIEW program contains two parts: front panel and block diagram [20-24]. The front panel vi (vi - program written in LabVIEW) is where the user can control and/or monitor the designed system. Block diagram vi is used to write the program for the desired application.

The front panel of the proposed system consists of a numerical indicator to display the efficiency of the specimen under test. A stop button is used to halt the process. Three numerical indicators to feed the tank size, aperture area, and tilt angle. Fig. 5 shows the front panel of the proposed technique.

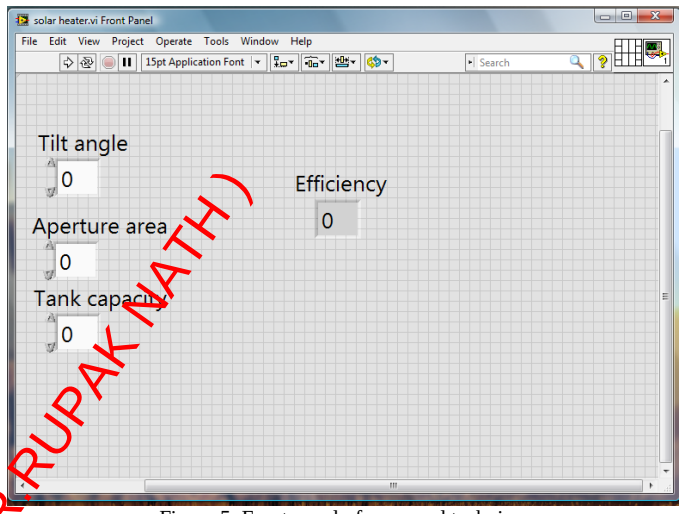

Figure 5. Front panel of proposed technique

The block diagram for the proposed system consists of a DAQ Assist to acquire the signals from sensors like RTD, Thermosyphon, and Pyranometer. Once the data is acquired the program is written to calculate the parameters like solar noon, and various other parameters required to calculate the calculate the efficiency of the solar heaters. Once the parameters of the desired equation is calculated the variables corresponding is calculated using the formula node. The data once used to calculate the efficiency of the solar water heaters, the results will be displayed using the numerical controls.

VI. RESULTS AND CONCLUSIONS

	Annu solar ltd	**Kirti solar ltd**	**Natural system**
Efficiency	53%	56 %	59%
Tank capacity	100LPD	100LPD	100 LPD
Aperture area	1.18 m2	1.18m2	1.56m2
Tilt angle	22˚	35˚	37.5˚

The data shows that the proposed technique has successfully achieved its proposed objective, and the following conclusions are made. Water temperature can be increased 30 to 35 degree with 600 w/m^2 radiation during a day. The water temperature decrease 4 to 8 degree during night with average ambient temperature of 20 degree at night. To get at least 10 days correct data more than 15 days experiment needed. Cold water should be pumped to tank during no solar condition. Solar noon varies from 11.23 am to 11.50 am maximum during the test period. Ideal time for test is from October to March generally.

REFERENCES

[1] Smith, Crosbie (1998), *The Science of Energy – a Cultural History of Energy Physics in Victorian Britain*, The University of Chicago Press. ISBN 0-226-76420-6.

[2] www.**bp**.com/.../**bp**...**Energy**.../**2030_energy_outlook**_booklet.pdf., BP energy outlook 2030.

[3] *Ministry of power India official website.*

[4] *2011 online available* http://www.gwec.net/index.php?id=180 .

[5] Chinese Government, "National Electric Power Industry", 2010.

[6] Min, B., Cheng, S. and Logan B. E. "Electricity generation using membrane and salt bridge microbial fuel cells", *Water Research*, 39 (9). (2005), pp1675–86.

[7] Holm, Alison (May 2010), *Geothermal Energy: International Market Update*, Geothermal Energy Association, pp. 7, 2010.

[8] *Ministry of new and renewable energy official website*

[9] Phillips, Kenneth J. H. (1995). *Guide to the Sun*. Cambridge University Press. pp. 58–67. ISBN 978-0-521-39788-9.

[10] John A. Duffie, William A. Beckman, *Solar Engineering of Thermal Processes*, ISBN 978-0-471-69867-8.

[10] Nand Kishor , Mihir Kr. Das , Anirudha Narain , Vibhaw Prakash Ranjan: *"*Fuzzy model representation of thermosyphon solar water heating system", *Solar Energy* 84 (2010) 948–955.

[12] Cynthia A. Cruickshank, Stephen J. Harrison, "Heat loss characteristics for a typical solar domestic hot water storage*"*, *Energy and Buildings* 42 (2010) 1703–1710.

[13] H.F. Naspolini, H.S.G. Militão, R. Rüther, "The role and benefits of solar water heating in the energy demands of low-income dwellings in Brazil ", *Energy Conversion and Management* 51 (2010) 2835–2845.

[14] Luis Juanico , *"A new design of roof-integrated water solar collector for domestic heating and cooling ", Solar Energy* 82 (2008) 481–492

15] Pei Gang, Li Jing, Ji Jie , "Optimization of low temperature solar thermal electric generation with Organic Rankine Cycle in different areas"**,** *Applied Energy* 87 (2010) 3355–3365.

[16] Lana Kenjo, Christian Inard, Dominique Caccavelli, "Experimental and numerical study of thermal stratification in a mantle tank of a solar domestic hot water system", *Applied Thermal Engineering* 27 (2007) 1986–1995.

[17 http://www.worldenergy.org/documents/ser_2010_report_1.pdf, World Energy council

[18] http://www.wordpress.com/2006/10/03/indian-energy-scenario/, Indian Energy Scenario indiastatistical.

[19] Technical specification supplied by Natural System pvt.ltd.

[20] www.ni.com/labview/

[21] Kevin James (2000), *PC Interfacing and Data Acquisition: Techniques for Measurement, Instrumentation and Control*, Newnes Publishers.

[22] Jovitha Jeroma (2000), *Virtual Instrumentation by LabVIEW*, Prentice Hill Publisher.

[23] Lisa K. wells, Jeffrey Travis (2000), *LabVIEW for everyone*, Prentice Hall, New Jersey, 1997.

[24] Sanjay Gupta, Joseph John (2005), *Virtual Instrumentation using LabVIEW*, Tata Mcgraw Hill Publishing Co Ltd.

An Agent Based Approach for Service provisioning in Cloud

Bidisha Goswami
PESIT-BSC
Assistant Professor
Bangalore, India

Angana Chakraborty
ISI Kolkata
Junior Research Fellow
Kolkata, India

Sankhyayan Choudhury
Calcutta University
Associate Professor
Kolkata, India

Abstract- *Appropriate delivery of the services to the customer as per their requirement becomes a challenge to the cloud service provider due to the complex distributed environment. Service Level Agreement (SLA) is the only term between customer and service provider that governs the conditions to be fulfilled at the time of service delivery. A cloud service provider offers the services from different server (location) and the same service may be offered by the different location with different cost based on the offered quality. The intention of the provider will be to select an effective schedule of services taken from various locations with minimum cost. In this work, we have made an attempt to propose an agent based solution that eases the decision making of a cloud service provider in this situation. The proposed agents are able to gather these information form different locations and render an effective delivery schedule (which service from which server).*

Key Words Cloud computing, Service provisioning, Multi-agent based techniques, AUML

I. INTRODUCTION:

Cloud computing provides a cost-effective, scalable and adaptive platform for service provisioning. These factors are driving migration of legacy applications into cloud computing platform. Cloud offers different level of services as Infrastructure-as-a-service, Platform-as-a-service & Software-as-a-service. In Cloud every resource usage is on-demand, integrated and ready to use combination of services. The services come of compute, storage, network, platform and application software available as a standardized set offerings as a pay-as-you-use pricing model.

The concept of cloud computing has come to make the computing resource virtualized and for optimized usage. Cloud computing is the pool of service center. Some of the traditional and emerging Cloud-based applications include social networking, web hosting, content delivery etc. Each of these application types has different distributed and dynamic system. The cloud has given the exposure to its users for enjoying the open and shared environment. Demand prediction and capacity management are crucial issues in cloud and hence dynamic resource allocation with the timely match of supply and demand [1] is required.

Cloud resource optimization is one of the biggest challenges for the cloud provider. The paper [2] has discussed the idea of cloud resource optimization. The author shows that optimizing of resource is able to reduce cost substantially. Using an objective function the author explained the mechanism needed to take place to resource optimization. The demand of resource can be two type either it is reserved otherwise on demand. If the service provider has the idea of resource provisioning in future then the provider can plan accordingly. However the challenge lies in on-demand instant resource allocation in cloud. Some work is taken place for cost minimization on demand service provisioning. The paper [3] describes the uncertain nature and problem of resource provisioning in cloud. Consumer's future demand is unpredictable. Hence it is difficult to predict the future demand of a resource at any time instant. The author addresses this problem and proposed an algorithm by formulating a stochastic programming model. However the approach has some implementation issue and complicated in nature. Again the stochastic model has its own limitation. In our proposed model we had a plan to use of agent based model to reduce the pricing. The nature of agent is dynamic and it behaves different according to circumstances. This is the reason agent has proven as an important entity for controlling the cloud environment. The paper [4] has exposed the aspect of agent usage in service configuration. The author presented architecture of Cloud which offers functionalities integrated with a mobile agent platform able to dynamically add and configure services on the virtual clusters. Paper [5] explains the value models using the agent which is used for qualitative and quantitative purpose. The author proposes a methodology to model the agents for interaction of service and business process.

II. PROBLEM DEFINITION

A service provider in a distributed environment like cloud generally has more than one server for offering the services to their customer. Initially there must be a service level agreement (SLA) between the customer and the service provider and SLA denotes the typical qualification of the services as requested by the customer e.g. maximum cost,

average response time etc. Service provider can offer same service from different server having different cost. Here the cost signifies the cost needed for providing the services by the provider. The cost of the same service offered from different server may vary based on the quality of the offered service. In this scenario, the challenge of the service provider is to choose the atomic services through which a composed service can be rendered to the user satisfying SLA with a minimum cost. Here an attempt has been made to propose a solution on behalf of a cloud for facing the above mentioned challenge. An agent based approach is used for proposing a methodology that can be used by a cloud.

For the sake of simplicity, here we assume an arbitrary weight for these two factors to calculate the cost function. But in future work the AI technique can be used to make the agent as an intelligent one about the behavior of the cloud such that the agent can predict the weight of the variables involved in the cost function. This intelligent technique will be beneficiary for a realistic implementation.

III. PROPOSED SOLUTION

In this section, we have proposed a solution for the above stated problem using the agent- based technology. Two types of agent are used here: a Stationary Agent and a Mobile Agent. Agents endowed with the property of mobility are called mobile agents. The Stationary agent is immobile and only takes the decision based on the information provided by the mobile agent. But the Mobile Agent travels the whole system to collect information of system statistics needed to do the task for the user. Finally the stationary agent takes the decision through the interaction with the mobile agent.

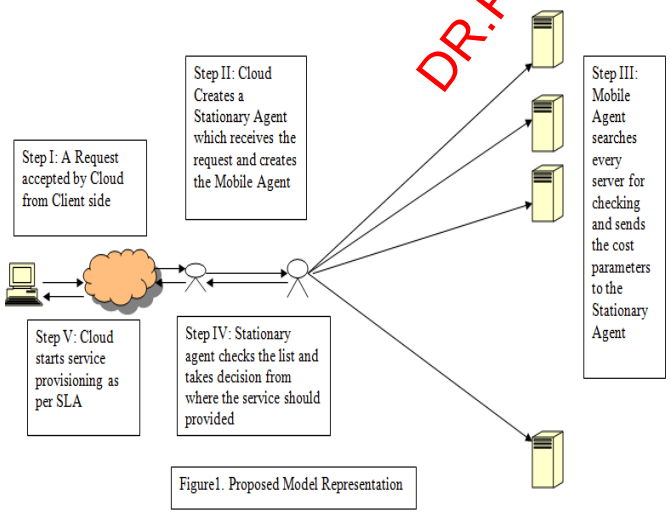

Figure1. Proposed Model Representation

The Proposed Methodology:

The mechanism is described based on the proposed framework as depicted in Figure1. The steps of the methodology are as follows:

Step I: The Cloud provider accepts a request from the clients with some typical requirements in form of Service Level Agreements (SLA). Here we assume that the SLA is identified by the metrics as: Cost range, Response time, CPU load, Security etc.

Step II: After receiving the request the Cloud generates a Stationary Agent. The Stationary Agent receives the request of the Cloud Consumer. This Stationary Agent is responsible to create a Mobile Agent for every request with specified SLA. Once the Mobile Agent is created then it specifies the service to the Mobile Agent.

Step III: The Mobile Agent moves on each of the server available to provide services and checks whether the service quality for the requested service matches with the requested parameters or not. If it matches, then the Mobile Agent identifies the details of the identified service, the corresponding server, the static cost for the requested service, the load of the server at that time instant and the traffic density of the lines lead to the server. This details is returned to the Stationary Agent .The later mentioned parameters are important to take the decision that sometimes it may not be beneficiary i.e. cost effective for offering a service from the server with high load and the higher chance of network congestion in spite of getting a cheap solution in terms of static cost of that service.

Step IV: The Stationary agent now checks the list of the Server which can offer the requested services. After getting the list it checks the corresponding servers from where the service can be fired and the parameters required for cost calculation. Here we are assuming the variables used in cost function have the same weight.

Step V: The cloud now starts providing the service as per the newly generated schedule.

The interactions in a distributed system are often achieved using communication protocols. These protocols involve transfer of large volumes of data stored at remote hosts over the network to a central processing site resulting in high network traffic. An alternative to using communication protocols is the use of mobile agents. Mobile agents are dispatched to the remote hosts containing the needed data.

The agents perform the computations at the remote hosts and return back with the results only. Thus the communication cost is reduced drastically as the computations are executed at

the data storage location instead of moving data to the computing location.

The task requested by a customer may be considered as a composition of some atomic services and the cloud is responsible for offering those services. Sometimes it may happen that the closest server (with respect to the customer) is able to provide the requested services but there may be a mismatching between the qualities. As a result there is no other alternative except taking the service from another server. There must be some static cost for each service offered from different server with different quality. Moreover the load on that server at that time instant and the network traffic leads to that server should be considered for cost calculation. The cost function should be an expression involving the static cost as well as the cost of communication, (as it increases based on the traffic density) cost generated due to the overloading on that server. Thus the Cost incurred for offering the requested service =Static cost needed for offering the chosen services + x (Load factor of that server) + y (Chance of congestion). Here we are assuming that chosen services from different server after composition will be able to delivery the requested service.

The agent based technique is used here to trap the cost value from each server and take the decision accordingly for choosing the minimum. Here the adaptive nature of the agents are exploited fully as you may get the different solution in various time generated by an agent based on same SLA.

Activity Diagram of Agents:

The activities of the proposed agents are described below through AUML design as defined in UML2.0 [7].

Stationary Agent:

This agent is created at the beginning and creates mobile agent. Once the mobile agents collect the information, this agent is responsible for decision making. The AUML diagram of Stationary agent is as given in Figure 2.

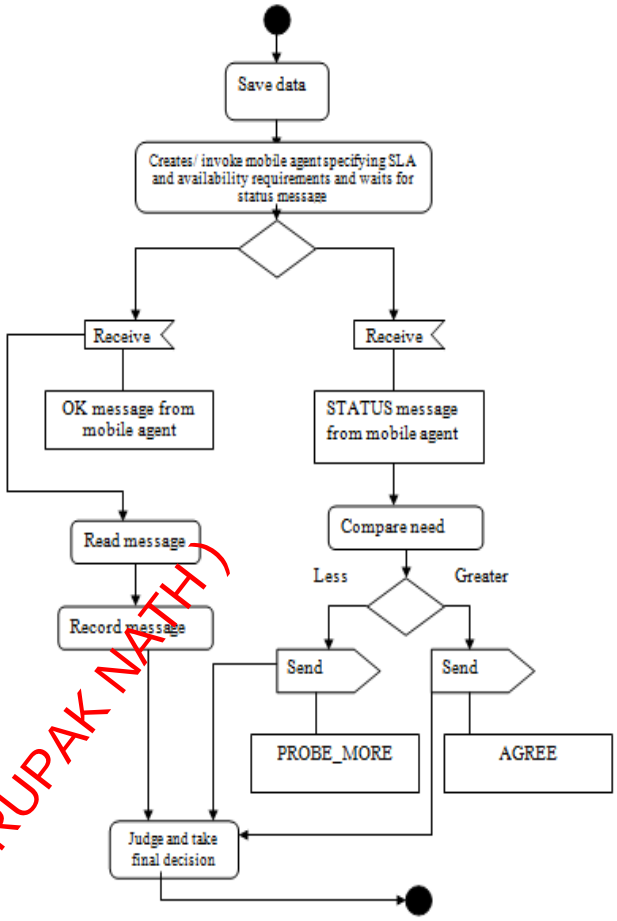

Figure 2: Stationary Agent

Mobile Agent:

Mobile agent is created by stationary agent. The mobile agent moves in every server and collects the status information of each server at every time instant. The collected information then sends to the Stationary agent. The AUML diagram of Mobile agent will be as in Figure 3.

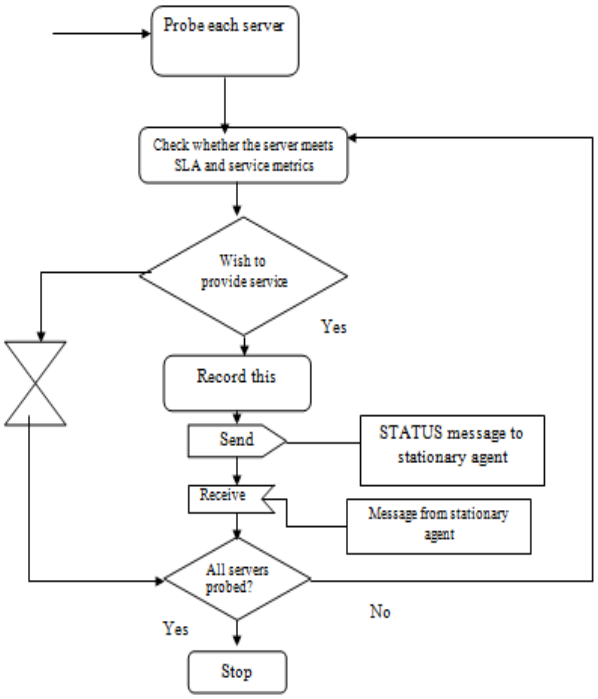

Figure 3: Mobile Agent Activity Diagram

IV. CONCLUSION

In this work, we have tried to propose a solution for the efficient service provisioning from the service provider point of view. We have tried to propose a solution through a multi-agent technique and the entire concept is implemented through agent-based programming. Here the adaptive nature of the agents can be exploited. It is because the different solution is generated based on the other cost factors like CPU overload and network congestion which changes time to time. Thus the cost value also changes accordingly due to the different values of the participating variables but with same SLA. For the sake of simplicity, in experimental purpose, here we assume an arbitrary weight for these two factors to calculate the cost function. But in future work the AI based technique can be used to make the agent as an intelligent one to apprehend the behavior of the cloud such that the agent can predict the weight of the variables involved in the cost function. This intelligent technique will be beneficiary for a realistic implementation.

V. BIBLIOGRAPHY

1. R. Buyya, J. Broberg, and W Voorsluys, Cloud Computing: Principles & Paradigms © 2011, John Willey & Sons, Inc.

2. Marin Litoiu & Milena Litoiu, Optimizing Resources in Cloud, a SOA Governance view, ISGIG, page Proceedings of the 2010 Workshop on Governance of Technology, Information and Policies , Pages 71-75ACM New York, NY, USA ©2010

3. Chaisiri, S. Bu-Sung Lee Niyato, D. ; Optimization of Resource Provisioning Cost in Cloud Computing Sch. of Comput. Eng., Nanyang Technol. Univ. (NTU), Singapore, Singapore **Volume:** 5, Issue: 2 **Page(s):** 164 – 177 IEEE Transaction @2012.

4. Aversa, R.; Di Martino, B. ;Rak, M. ;Venticinque, S, Cloud Agency: A Mobile Agent Based Cloud System Dept. of Inf. Eng., Second Univ. of Naples, Aversa, Italy **Page(s):** 132 - 137, IEEE Conference paper on International Conference on Complex, Intelligent and Software Intensive Systems @2010

5. Hoa Khanh Dam and Aditya Ghose.: An agent-oriented approach to service analysis and design. International Workshop on Services and Agents (ServAgents 2010) held at PRIMA 2010, Kolkata, India,November 2010.

6. M. Luck. , McBurney P. and Preist. C and the AgentLink Community, Agent Technology: Enabling Next Generation Computing, Agent Technology, a roadmap. page 94- 1: 94, Agentlink @2003

7. M. Kang*, L. Wang and K. Taguchi: Modeling Mobile Agent Applications in UML2.0 Activity Diagrams, School of Computing, Leeds Metropolitan University*, Department of Computing, School of Informatics, University of Bradford. Edinburgh, Scotland, 2004, p.104–111 "Third International Workshop on Software Engineering for Large-Scale Multi-Agent Systems (SELMAS'04)"@2004